# Water and $CO_2$ Adsorption on Magnetite Surfaces: a Combined Molecular Beam and IRAS Study

Dissertation zur Erlangung des akademisches Grades

**doctor rerum naturalium**

(Dr. rer. nat.)

im Fach Chemie

eingereicht an der

Mathematisch-Naturwissenschaftlichen Fakultät

Humboldt-Universität zu Berlin

von

**MSc. Chem. Francesca Mirabella**

Präsidentin der Humboldt-Universität zu Berlin:

Prof. Dr.-Ing. Dr. Sabine Kunst

Dekan der Mathematisch-Naturwissenschaftlichen

Fakultät: Prof. Dr. Elmar Kulke

Gutachter: 1. Prof. Dr. Hans-Joachim Freund

2. Prof. Dr. Klaus Rademann

3. Prof. Dr. Hans-Peter Steinrück

Datum der Promotion: 17.07.2018

*“Da chimico un giorno avevo il potere*
*di sposare gli elementi e di farli reagire,*
*ma gli uomini mai mi riuscì di capire*
*perché si combinassero attraverso l'amore,*
*affidando ad un gioco la gioia e il dolore”.*
*F. De Andrè*

# Abstract

The interaction of water and $CO_2$ with oxide surfaces is nowadays a hot topic especially for environmental scientists. The use of water as hydrogen for $CO_2$ reduction/hydrogenation would be the most ideal process, which would contribute to reduce $CO_2$ emission into the atmosphere and minimize the dependence of society on fossil fuels. Despite certain advances in this field, further fundamental studies need to be addressed to understand the interaction of water and $CO_2$ with metal-oxide surfaces for a rational design of heterogeneous catalytic processes.

This work presents a fundamental study of the adsorption of water and $CO_2$ on well-defined $Fe_3O_4(111)$ films grown on Pt(111) single crystal. To understand the adsorption properties of the iron oxide film, the surface has been characterized using CO as probe molecule. The characterization showed that the magnetite surface is terminated by a 1/4 monolayer of tetrahedrally coordinated $Fe^{3+}$ ions on top of a close-packed oxygen layer. On this well characterized surface, the interaction with water and $CO_2$ has been investigated in detail. Combined IRAS and TPD data revealed that water readily dissociates on the surface, forming two hydroxyl species, $O_wH$ and $O_sH$, involving oxygen atoms from the water (w) itself and from the oxide surface (s), respectively. At increasing coverage, these species act as anchors for molecular water adsorption ultimately giving rise to a long-range ordered architecture. DFT calculations rationalized these data in the framework of cooperative formation of the hydrogen bonding network. Moreover, $Fe_3O_4(111)$ seems to be rather inert towards $CO_2$ chemisorption at low temperatures, and the formation of weak chemisorbed species may be interpreted as driven by surface imperfections. At higher temperatures, the presence of water on the regular surface (induced and/or just as residual gas adsorption) plays a critical role in the $CO_2$ activation, promoting the formation of bicarbonate-like species.

# Zusammenfassung

Die Wechselwirkung von Wasser und $CO_2$ mit Oxidoberflächen ist vor allem ein bedeutsames Thema für Umweltnaturwissenschaftler. Der Gebrauch von Wasser als Wasserstoff-Ressource für die Reduktion/Hydrierung von $CO_2$ würde zu einer Reduktion der $CO_2$-Emmissionen in der Atmosphäre führen. Trotz einiger Fortschritte in diesem Bereich sind weitere grundlegende Studien notwendig, um die Wechselwirkung von Wasser und $CO_2$ mit Metalloxidoberflächen zu verstehen und darauf aufbauend eine rationale Gestaltung Katalyse-Prozesse zu ermöglichen.

Die vorliegende Arbeit präsentiert grundlegende Studien der Adsorption von Wasser und $CO_2$ auf wohldefinierten $Fe_3O_4$(111) Filmen, welche auf einem Pt(111) Einkristall aufgewachsen wurden. Die Oberfläche wurde zuerst durch Adsorption von CO als Sondenmolekül gestützt. Es zeigt sich, dass die Magnetitoberfläche aus einer 1/4-Monoschicht tetraedrisch angeordneter $Fe^{3+}$-Ionen auf einer dicht gepackten Sauerstoffschicht besteht. Auf dieser gut charakterisierten Oberfläche wurde die Wechselwirkung mit Wasser und $CO_2$ sodann detailliert untersucht. Kombinierte IRAS- und TPD-Daten deckten auf, dass Wasser leicht an der Oberfläche dissoziiert und unter Einbeziehung von Sauerstoffatomen aus dem Wasser selbst bzw. von der Oxidoberfläche zwei Hydroxylspezies bildet. Diese Spezies fungieren als Anker für die molekulare Wasseradsorption, die schließlich zu einer geordneten Struktur führt. DFT-Rechnungen rationalisieren diese Ergebnisse im Rahmen einer kooperativen Bildung des Wasserstoffbrückenbindungsnetzwerkes.

Die Magnetitoberfläche scheint hingegen eher träge gegenüber der $CO_2$-Chemisorption zu sein. Bei niedrigen Temperaturen kann die Bildung schwacher chemisorbierter Spezies als durch Oberflächendefekte bedingt interpretiert werden. In Jedem Fall spielt bei höheren Temperaturen das Vorhandensein von Wasser auf der regulären Oberfläche eine entscheidende Rolle in der $CO_2$-Aktivierung und fördert die Bildung von Bikarbonat-Spezies.

# Table of Contents

# 1. Introduction

Heterogeneous catalysis has become a key point in many processes including environmental technology, energy storage and conversion as well as chemical synthesis[1,2]. Research in heterogeneous catalysis is branched into multiple sub-fields and, due to its complexity, there is the urge for an interdisciplinary approach that integrates methods, concepts and expertise from different chemical disciplines. The questions that can be answered and the problems that can be solved by heterogeneous catalysis constitute key questions for a highly industrialized society like ours. However, in the future, an ever-growing need for productivity must be matched by solutions able to take responsibly into consideration the increasingly complex environmental and energy demands.

By definition, a catalyst changes the kinetics of a chemical reaction, controls its rate and influences its selectivity, but does not alter the thermodynamics of the reaction. Although the catalyst is not being consumed during the reaction, it participates in the chemical process: the catalyst's role is basically a medium which holds the reactants on its surface and changes their molecular geometry, electronic structure, or even turns them into new intermediate species. Typically, heterogeneous catalysts consist of two main components: a thermally stable support - usually a metal oxide -, and an active phase, which can be either a metal or a metal oxide, often dispersed as small particles. These nanostructured objects display several different sites (they are generally characterized not only by distinct facets, corners, edges, but also by defects sites), which play a crucial role in the kinetics of the catalyzed reaction. Besides, the support is also characterized by regular as well as defective oxide areas. It has also been found that several factors can affect the catalyst performance. Thus, sites modification by promoters or poisons, particle size, size distribution, morphology and oxidation state as well as the interaction between support itself and active phase, or the possibility of catalyst restructuring under reaction conditions, must be taken into account. Because of the high complexity of these systems a rational way of designing new catalysts has not been established yet. Thus, in order to develop a good catalyst, it is important to better understand the reaction mechanism happening on the surface and also how it depends on the electronic and geometric surface structure as well as the interaction with adsorbed reactants[1,3,4].

There are basically two different approaches in catalysis research: either the reactivity of the catalyst is studied under conditions as realistic as possible, or the catalyst will be simplified to model systems (e.g., for metal catalysts the simplest case, would be a metal single crystal) investigated under well-defined conditions such as ultra-high-vacuum. The latter allows a chemically clean environment and thus high control of the molecules adsorbed on the surface. The advantage of the first approach is that, by varying the structural parameters of the catalyst, it is possible to have access to macroscopic information directly relevant for applications. On the other hand, atomic details, and, therefore, a truly microscopic understanding of the reaction mechanism, are not accessible. In the second case, the structural and chemical complexity of the catalyst is reduced, ensuring the availability of the atomic details using spectroscopic methods. The ideal achievement, in this sense, would be to be able to describe the elementary steps of a process – such as adsorption/desorption, diffusion or reaction – in details. However, there is a lack of availability of such models. The use of the proper model catalyst, though, in combination with the surface science tools, provides detailed insights into chemical reactions on surfaces. Indeed, in the last two decades, the focus of surface chemistry on single crystal surfaces[4] has moved towards development of a model catalyst approach[5–10]. With model catalysts is possible to mimic some important structural properties of applied catalysts. These systems are also accessible by surface science methods, allowing a detailed characterization at the atomistic level of their geometries as well as electronic structures.

Despite the big contribution given by UHV studies to the understanding of catalytic processes[4], there is a substantial difference between these model systems and the industrially applied ones, regarding mainly the pressure range ("pressure gap") and also the complexity of the catalyst ("material gap"). These gaps are the reasons why these simple model systems may only poorly resemble the properties of the real catalyst surfaces[5,10]. A very promising approach to overcome both the material and the pressure gap and to mimic the structures and pressure conditions of a real catalyst while keeping the working conditions under a clean and controlled environment as well as knowing the structural details at atomic level, is to combine molecular beam experiments[10,11] with well-defined metal oxide catalysts[12]. Hence, the large degree of chemical complexity, deriving from the interaction between multiple adsorbed

gases under high pressure conditions, can be overcome by crossing multiple molecular beams on the catalyst surface. As it will be explained in a more extended way in Section 3.3.1 of Chapter 3, molecular beams provide a well-defined directed flux of molecules having pressures in the range between $10^{-10}$ and $10^{-5}$ mbar at the sample surface, while the background pressures stays several orders of magnitude lower. This allows to create a certain degree of chemical complexity on the catalyst surface in an otherwise UHV environment.

In this scenario, metal oxides play a significant role, being employed in the catalytic processes not only as support for active materials, but also as active components themselves. In this sense, much progress was made in the last decades in the preparation of well-defined metal oxide surfaces, epitaxially grown on metal single crystals and then used as model systems[6,7,13]. Although the advantages and properties of thin metal oxides will be discussed in more detail in Chapter 2, some general aspects are also considered in this introduction. From the experimental point of view, the main advantages of preparing thin metal oxide films result from their enhanced electrical and thermal conductivity. This makes them suitable to be investigated using electron spectroscopies, scanning tunneling microscopy and other experimental methods on the surface science toolbox based on charged carriers, because those systems do not show charging effects[8]. Besides, as a consequence of the film growth onto a metal support - which acts as a mirror -, the surface displays high reflectivity and, therefore, can be investigated using reflection infrared spectroscopy (IRAS)[7,10]. In this work, for example, infrared-reflection-absorption spectroscopy is employed as main spectroscopic technique for the surface investigation.

One less obvious advantage is the possibility to prepare surfaces using different isotopes. The opportunity to perform experiments employing isotopic labelling not only for the adsorbates but also for the surface, is a key approach in the presented work (see Chapter 5 and 6), which, combined with infrared reflection absorption spectroscopy, appears to be perfectly suited to characterize and identify functional groups or bonding environments on a surface.

Nonetheless, it must always be considered that metal oxides are extremely complex objects. Consequently, the preparation of defined oxide surfaces is difficult and is

heavily affected by preparations parameters (i.e, oxidation temperature, oxygen partial pressure, vacuum conditions)[14]. Undesired formation and possible coexistence of different surface structures may happen as well as the presence of surface defects which can dominate the catalytic properties rather than the well-ordered surface areas. To elucidate and control catalytic processes on such surfaces is a formidable task, which requires the joint effort of several experimental techniques as well as theoretical support.

In this thesis, a thin iron oxide (magnetite) film was used as model catalyst. Among the transition metal oxide catalysts employed in heterogeneous catalysis, iron oxides have proven to be invaluable materials, used not only to catalyze certain reactions, but also as inexpensive support for metal nanoparticles[15]. Enormous success has been received from iron oxide-based catalysts employed in the Fenton reaction[16], ethylbenzene dehydrogenation to styrene[17], and Fischer-Tropsch synthesis[18] as well as in the water-gas shift reaction (WGSR)[19,20].

In particular, magnetite seems to be one of the most explored iron oxide in surface science[15], principally because its stability range fits very well to the ultra-high vacuum environment. Besides, it is an electron conductor, which is necessary for studying it with surface science. $Fe_3O_4$ shows two different surface-orientations, (111) and (100), when properly grown epitaxially onto Pt(111) and Pt(100) single crystals, respectively. Among the two, $Fe_3O_4$(100) is the best understood iron oxide: its structure is known with a high accuracy level and also most of the defects and properties have been already characterized[13,15,21]. On the other hand, although $Fe_3O_4$(111) has been studied for more than twenty years, a controversy regarding the question which one is the most stable surface termination is still ongoing. To understand the catalytic and adsorption properties of the $Fe_3O_4$(111) films used in this work, a detailed characterization of the surface was performed using CO as probe molecule. Adsorption studies are extremely helpful for the investigation of the surface structure of oxides. Indeed, the adsorption properties of oxides are the key for the understanding of the mechanism of catalytic reactions which use metal oxides as catalysts. In the case of catalysts based on magnetite, and/or any other reducible oxide, the adsorption of molecules such as water or hydrocarbons may include decomposition processes of the adsorbates. In order to be able to directly correlate

the probe molecule's absorption properties with the oxide surface structure it is necessary to overcome these difficulties. Carbon monoxide fulfils these requirements[22] and, therefore, was chosen to study and characterize the magnetite surface in this work.

The aim of this thesis is to characterize the processes of adsorption and activation of water and carbon dioxide on a well-defined magnetite surface. The motivation arises from the potential use of $CO_2$ and water as raw materials which can be converted in valuable feedstock. $CO_2$ is one of the most abundant components in the atmosphere and since its emissions on Earth are rising, the interest in attempting to soften the global warming by improving storage and/or $CO_2$ sequestration technologies, has increased rapidly in the past ten years. In this picture, it is essential to understand the interaction between $CO_2$ and environment components, such as water[23]. Adsorption/activation of $CO_2$ and water are also of great interest in catalysis, being involved in technological important chemical reactions, such as the ones mentioned earlier, where iron oxide materials have been employed as catalysts[15,16,18,17,19,20]. However, $CO_2$ displays the most oxidized state of carbon which renders it rather inert to chemical transformations. Therefore, despite the advances in this field, further fundamental studies are needed in order to understand the activation and interaction of water and $CO_2$ with catalyst substrates, especially metal-oxide surfaces, for rational design of heterogeneous catalytic processes.

In this work, the initial stage of water and $CO_2$ adsorption on well-defined $Fe_3O_4$(111) films grown on Pt(111) single crystal was studied in detail from a spectroscopic point of view. Particularly, this thesis is structured as follows. Chapter 2 reports a literature survey on metal oxide surfaces. Moreover, a description of the planar model catalysts of interest is provided, followed by an overview of the surface structures and reactivity of the (111)- and (100)- oriented $Fe_3O_4$. The up-to-date knowledge on the water and $CO_2$ adsorption on metal oxide is also discussed. Chapter 3 presents some general insights on the gas-surface interface interaction and introduces the main techniques used in this thesis. Chapter 4 deals with the characterization of the $Fe_3O_4$(111) film, using CO adsorption as probe molecule. The outcome of this adsorption study is crucial to understand the surface adsorption properties of magnetite towards water and $CO_2$. The core of this thesis is represented

by Chapter 5 and 6, which discuss the adsorption of water and $CO_2$, respectively. Thereafter, Chapter 7 presents preliminary results on the adsorption of water and $CO_2$ on $Fe_3O_4$(100). These results are then compared to the results obtained on the (111)-orientated surface and possible differences in their reactivity are discussed. Finally, the work is summarized in Chapter 8.

It must be mentioned that the adsorption of water and $CO_2$ on magnetite surfaces is a very challenging task which has required enormous effort from different teams. In particular, the presented work will face up to the problem from a mainly spectroscopic point of view, whereas the Temperature-Programmed-Desorption and LEED, and the Density-Functional-Theory aspects will be examined by the forthcoming PhD-theses of Eman Zaki and Xiaoke Li.

# 2. Metal Oxide Surfaces

This chapter is divided into five sections. In the first Section (2.1) some general aspects of metal oxides used as catalysts will be discussed. The second and third Sections (2.2 and 2.3) review findings of previous relevant studies on $Fe_3O_4(111)$ and $Fe_3O_4(100)$ surfaces. Finally, a literature survey to sum up the key knowledge on water and $CO_2$ adsorption on magnetite and other metal oxide surfaces is reported in Sections 2.4 and 2.5.

## 2.1 General Aspects

The progress of surface science in the understanding of the surface chemistry of metal oxides have been moderate compared to bare metals, despite of the fact that their preparation under well-defined ultra-high vacuum conditions can be accomplished by simple mechanical cleavage of a bulk single crystal. One reason for this is the metal oxides low thermal and electric conductivity which leads to unwanted electrostatic charging in scanning tunneling microscopy and variants as well as spectroscopic techniques based on charged information carriers[24]. A second reason is the higher complexity of oxide surface structures compared to a metal surface. Therefore, the preparation of model substrates with a certain set of properties (e.g. exacts surface plane, certain stoichiometry, defects concentration) is challenging. In the literature it is possible to find some examples of metal oxide surfaces that have been studied in detail with bulk samples: an outstanding case is titanium oxide[25]. For instance, it is possible to obtain for the rutile form many stable low Miller index surfaces just with the proper selection of polishing conditions. Also, simple UHV treatments allow, for example, to enhance the electroconductivity of the substrates[26].

Another preparation method, different from the ordinary mechanical bulk cleavage, is to grow them in the form of thin single-crystalline films supported on metallic substrates[12]. The structure of the oxide film is mainly determined by the geometry of the metallic substrate acting as a support. Thus, the structural properties of the film are ruled by the epitaxial relation between the lattice constants of the metallic substrate

and the oxide film itself. This leads to the possibility of having – within a certain range – control on the defects architecture and density of the grown layers, knowing the lattice mismatch. A more detailed description of the various aspects of metal-supported-thin films used as model systems can be found elsewhere[6,13,7]. There are three main methods for the preparation of thin epitaxial oxide films: i) oxidation of a pure metal, ii) evaporation of a metal under oxygen atmosphere onto an inert substrate, iii) oxidation of an alloy. Oxidation of a pure metal is the simplest way of producing well-ordered oxide layers. Examples of samples prepared in this way are NiO(100) on Ni(100) and $Al_2O_3$ on NiAl(110)[27,28]. Certainly, in this case a large lattice mismatch between metal and oxide lattice constants may result in a defect rich film. The second method, based on physical vapor deposition, provides films grown choosing inert metal substrates onto which the metal to be oxidized is evaporated (the oxidation step may be done during or after the deposition). Besides, with the proper lattice constant of the inert substrate, the grown film may exhibit long-range order of high quality. A different variety of thin films can be prepared by changing the supporting material and its surface planes or by introducing a buffer layer. Great examples of oxides grown with molecular beam epitaxy methods are MgO grown onto Ag(100), Fe(100), Mo(100)[29], ZnO onto Pd(111), Pt(111), Cu(111)[30], Cu(100), Cu(110)[31], ceria on Ru(1000), Ni(111)[32], iron oxides on Pt(111), Pt(100), MgO(100)[33], and other binary as well as more complex oxides. Generally, the surface properties of the thin films reproduce very well those of the bulk materials and are therefore widely used in catalysis as model systems[34].

Magnetite is a metal oxide of importance and its chemical properties have been midpoint of study from surface scientists for many years. As 150 other metal oxides, $Fe_3O_4$ crystallizes in the spinel structure. As shown in Fig. 2.1, the general formula of spinel is $AB_2O_4$, where A and B can either be different cation species (e.g. $MgAl_2O_4$ and $CuFe_2O_4$) or different oxidation states of the same cation, as in magnetite ($Fe^{2+}Fe^{3+}{}_2O_4$). Their structure consists of a close packed array of oxygen anions into a face-centered cubit sublattice having 1/8 of the tetrahedral and ½ of the octahedral interstices occupied (see Fig. 2.1)[35].

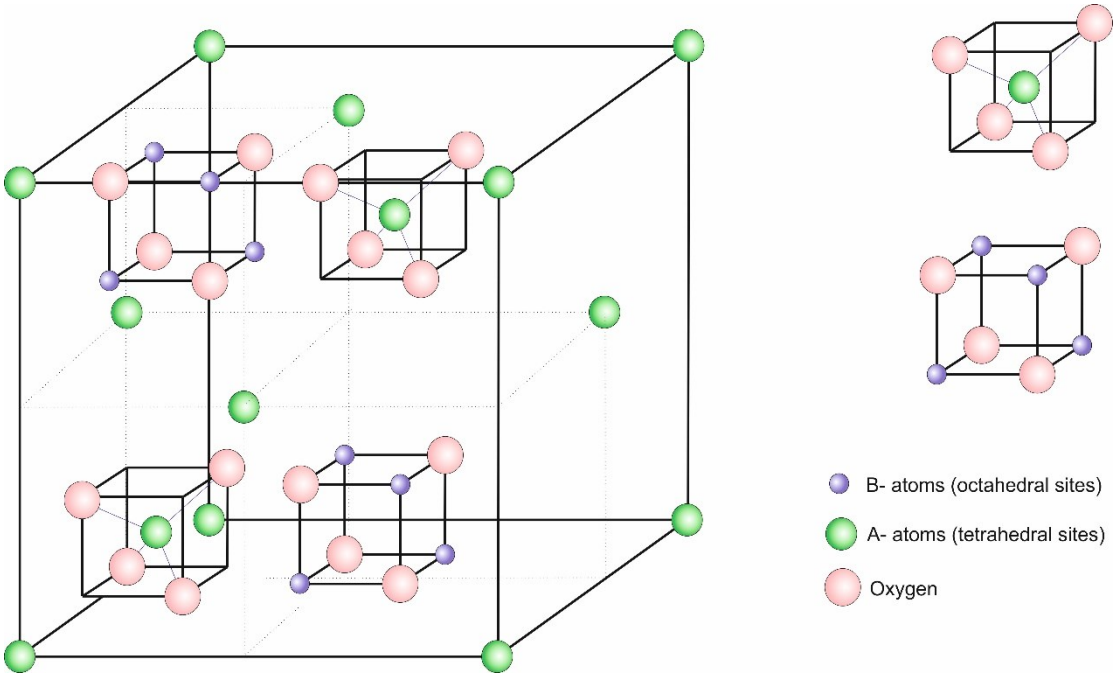


*Fig. 2.1 Spinel Structure.*

In common spinel, such as $MgAl_2O_4$ and $CuFe_2O_4$, the tetrahedral holes are occupied by the $A^{2+}$ cations, while the octahedral sites are filled with the $B^{3+}$ cations. If the $A^{2+}$ cations have a large crystal field stabilization energy (LFSE)[35], they will occupy half of the octahedral interstices while the displaced $B^{3+}$ cations will then adopt the tetrahedral coordination. The latter structure is known as "inverse spinel" and it is the case for $Fe_3O_4$. In magnetite, the coexistence of $Fe^{2+}$ and $Fe^{3+}$ in the octahedral sublattice leads directly to many of its interesting material properties. There is, for example, a rapid electron hopping between $Fe^{2+}$ and $Fe^{3+}$ above 125 K, resulting in high electric conductivity[36]. Also for titanium oxide, magnetite surface properties have been intensively studied using single crystal samples[37, 38]. On the other hand, model systems based on well-ordered thin oxides films grown onto metal supports may offer some advantages compared to bulk materials. As multiple phases exist in the iron-oxygen binary system ($Fe_2O_3$, $Fe_3O_4$, FeO), the use of the supported substrates was proved to be more convenient in studying equilibrium bulk and surface structures[39].

We have chosen magnetite as catalytic substrate for the present work because of the current status of knowledge regarding iron oxides surfaces, being $Fe_3O_4$ the most studied iron oxide in surface science[40].

## 2.2 $Fe_3O_4$(111) Films and Surface Structures

The $Fe_3O_4$(111) surface has been extensively studied in surface science. In particular magnetite films have been grown on different single crystal substrates such as Pt(111)[33, 22, 41, 42, 43, 44], Pt(100)[21], Au(100) and (111)[45], Cu(100)[46], sapphire (0001)[47]. In general, when Fe is deposited in oxygen atmosphere, a FeO(111) wetting layer forms at the interface and a close packet oxygen layer templates further growths: this makes the (111) the most common growth direction[21]. In this work $Fe_3O_4$(111) has been grown onto Pt(111) single crystal substrates. Details of the growth mode of $Fe_3O_4$(111)/Pt(111) can be found in the review from Weiss and Ranke[33], whereas our film preparation will be discussed in Chapter 4.

The magnetite crystal lattice along the (111) direction has close-packed hexagonal oxygen arrays stacked into an ABC lateral sequence[41]. Two different iron layer types, known as Kagomé- and mix trigonal layer, separate the oxygen layers. The Kagomé layer contains octahedrally coordinated iron cations (a 50:50 mixture of $Fe^{3+}$ and $Fe^{2+}$) which fill ¾ of the available sites and arrange themselves in a hexagonal lattice showing a 6Å periodicity. Furthermore, the mix trigonal layer shows both octahedral and tetrahedral sites, and the iron cations are indeed arranged in three parallel planes. In particular, tetrahedrally coordinated $Fe^{3+}$ cations sit next to the two opposite oxygen planes, while octahedral coordinated iron ions constitute the middle cation array. Also, in each of these layers, a periodic structure with a 6Å hexagonal unit cell is formed. Fig. 2.2 shows a side view of magnetite structure and a top view of the cation layers.

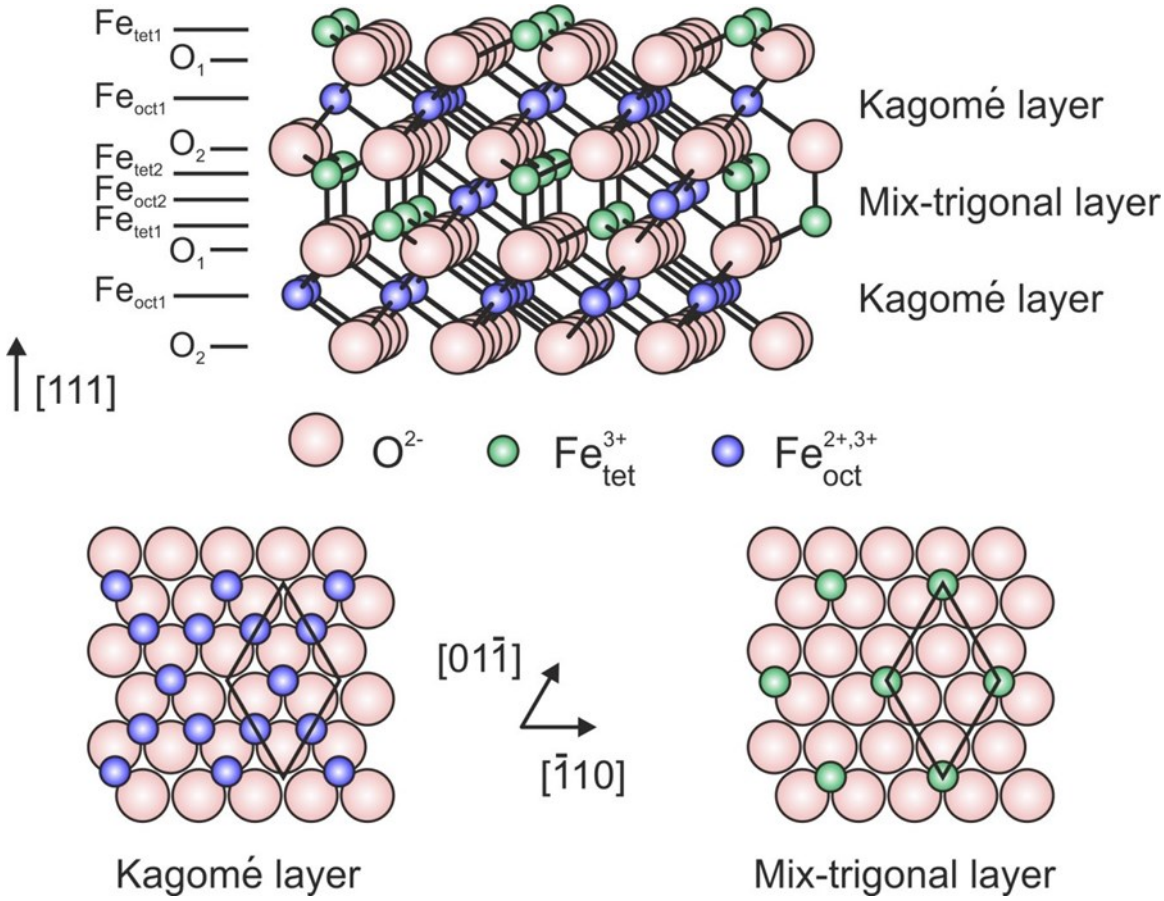


*Fig. 2.2. Side and top views of $Fe_3O_4$ lattice along the (111) direction. The top view shows the two different Kagomé and Mix-trigonal layers.*

As illustrated in the above Fig. 2.2, the (111) direction of the magnetite structure consist of six planes of atoms, which means that six formal bulk truncated terminations are possible. The six planes are generally expressed in literature as $Fe_{tet1}$, $O_1$, $Fe_{oct1}$, $O_2$, $Fe_{tet2}$, and $Fe_{oct2}$. Both the tetrahedrally ($Fe_{tet1}$, $Fe_{tet2}$) and octahedrally ($Fe_{oct1}$, $Fe_{oct2}$) iron terminated layers as well as the two oxygen layers ($O_1$, $O_2$) differ because of their neighboring atom planes above and underneath. The $O_1$ and $O_2$ planes are fcc close packed $O^{2-}$ layers and, consequently, negatively charged, whereas the Fe containing planes are positively charged. This makes the $Fe_3O_4$(111) a Tasker type-3 polar surface[48]. Thus, a simple bulk truncation is expected to be energetically unstable and a criterion for surface reconstruction or for its electronic rearrangement is, therefore, needed to explain its existence[41, 49, 50]. However, a crystal cleaved along the Kagomé layer exposes a $Fe_{oct1}$ surface termination characterized by ¾ ML of iron atoms over an oxygen layer. The $Fe_{tet1}$ and $Fe_{tet2}$ display subsequently ¼ ML of cations

in tetrahedral positions, whereas the $Fe_{oct2}$ termination exposes ¼ ML of six-fold coordinated Fe.

Although there have been more than twenty years of study on the (111) surface of $Fe_3O_4$, significant controversy remains in the literature concerning the thermodynamically most favored surface termination. Different models have been proposed and some of them are described below.

LEED experiments conducted on thin $Fe_3O_4$(111) films grown onto Pt(111) substrates, combined with STM studies, suggested a bulk termination at the $Fe_{tet1}$ plane with a 1/4 monolayer of tetrahedrally coordinated $Fe^{3+}$ ions over a close-packed oxygen layer[41, 43]. Following LEED I/V studies[41, 43, 50] agreed with the latter statement presenting a quite acceptable Pendry R-factor (0.19). Another evidence for the $Fe_{tet1}$ terminated surface was found by Weiss et al. who observed it as dominant structure after a final oxidation step at 1000 K[41]. Lower oxidation temperatures (~870 K), showed formation of the biphase covering 5-15% of the film surface[43]. Sala et al.[14] performed the most recent LEED study on $Fe_3O_4$(111) surfaces and concluded that the $Fe_{tet1}$ termination forms after a final annealing in UHV at 900 K. However, previous adsorption studies of CO and water on the magnetite surface invoked the octahedrally terminated surface $Fe_{oct2}$ to rationalize the experimental data[22, 51]. The considerable complication of working with $Fe_3O_4$(111) surface is due to the fact that multiple terminations can actually coexist and the surface prepared seems to be strongly sensitive to the growth conditions and also sample history[40].

To shed light on the question how $Fe_3O_4$(111) surfaces terminate and in order to obtain a unified picture is one of the main research goals of this work. In particular, a CO adsorption study using IRAS and TPD measurements, corroborated by DFT calculations, ruled out the presence of octahedrally coordinated iron ions ($Fe_{oct2}$) on the regular surface, but on defect sites such as, for example, step edges. The details of this study, together with the surface preparation procedure used in this thesis will be discussed in Chapter 4.

## 2.3 $Fe_3O_4$(100) Films and Surface Structures

In the (100) direction, two different atomic arrays alternate, and they are typically known as A-layer and B-layer. As Fig.2.3 shows, the A-slab consists of tetrahedral iron atoms, whereas the B- one is a mixed octahedrally terminated iron and oxygen layer. It is well known that LEED patterns of $Fe_3O_4$(100) surfaces typically exhibit a $\left(\sqrt{2}\,x\sqrt{2}\right)R45°$ reconstruction in both epitaxial and natural samples[52, 53, 54] Earlier studies proposed the surface charge neutrality as being the driving force for this reconstruction. Further models discussed it as an auto-compensated B-terminated surface characterized by an octahedrally coordinated iron cations array and a tetrahedrally coordinated oxygen, along with one oxygen vacancy per unit cell[53, 54, 55]. As reported by the surface phase diagram built in the framework of ab initio thermodynamics, a modified B-terminated surface seems to be the most stable over a wide range of oxygen potentials. This stabilization occurs upon a Jahn-Teller distortion that causes a wavelike displacement of Fe and O atoms in the top B layer, through which the $\left(\sqrt{2}\,x\sqrt{2}\right)R45°$ superstructure is formed (Fig. 2.3)[56, 57]. Density functional theory showed that both A- and B-terminated surfaces have similar surface energies[58], meaning that these two surfaces are strongly sensitive to the preparation conditions. Accordingly, Parkinson et al. observed the same behavior experimentally. In their work, they were able to prepare in a reproducible way both the B-termination and a metastable A-termination on a single crystal samples by varying the annealing temperature[59]. A recent study from Bliem et al., used a combination of LEED I/V, STM and DFT to rationalize the B-layer stabilization as due to an ordered array of subsurface cation vacancies (SCV)[60]. In this model, the B-layer remains stoichiometric, but it is distorted by rearrangement of the cations in the subsurface layers. Precisely, two octahedrally coordinated iron from the third layer are replaced by an additional interstitial tetrahedrally coordinated iron in the second layer. This structure was predicted to be thermodynamically stable over a broad range of oxygen pressures up to $10^{-5}$ mbar.

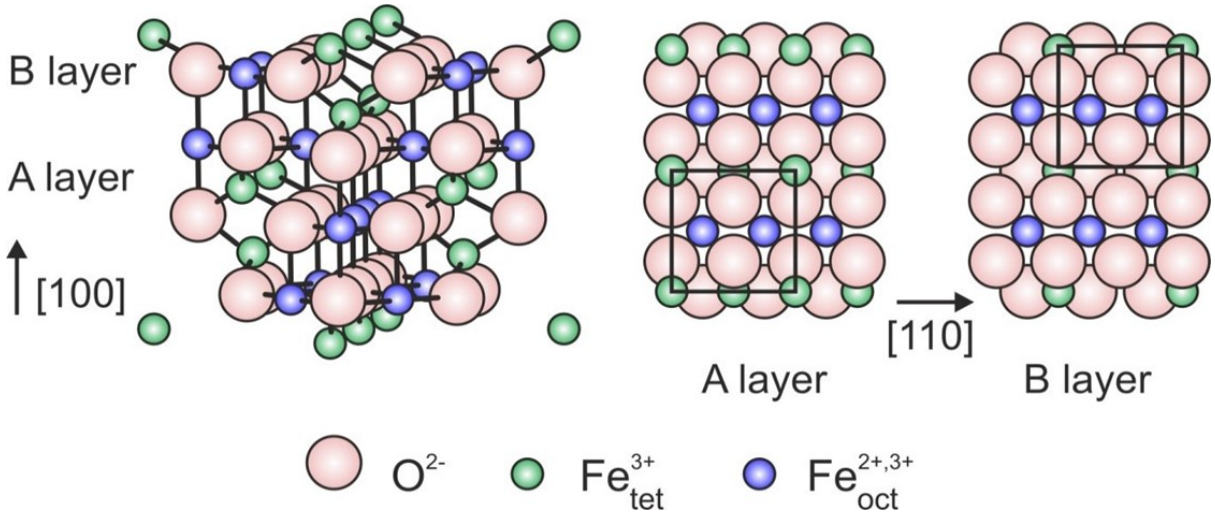


*Fig. 2.3. Side and top views of the $Fe_3O_4$(100) lattice. The side view shows the stacking sequence of atomic array, while the top views illustrate the two types of ideal bulk truncated surface.*

As for $Fe_3O_4$(111), well-ordered epitaxial $Fe_3O_4$(100) film are widely used as model substrates for catalytic studies. A typical support for the growth of such films is MgO(100). Chambers et al. were the first who used oxygen plasma to prepare the oxide film onto a UHV cleaned MgO(100) crystal[61]. Later on, Korecki et al. improved the $Fe_3O_4$(100) preparation making use of an Fe buffer layer to prevent migration of Mg atoms and allow higher annealing temperatures. They found out that this procedure led to a Fe-rich termination known as "dimer" termination[21, 62]. Recently, a new procedure for $Fe_3O_4$(100) preparation onto Pt(100) single crystal supports was developed by Davis et al.[21] Their growth also involves the use of a Fe buffer layer. It was observed that the thickness of the buffer layer is indeed a critical parameter in the growth process and the two most stable terminations (A and B) can be prepared by varying the growth conditions.

## 2.4 Water on Iron Oxide

The adsorption of water on magnetite surfaces has been widely investigated on both bulk single crystals and well-ordered epitaxial films[63,64]. The following literature survey sums up the crucial aspects of water interaction with iron oxide observed in the last years. Room- (and low-) temperature ultraviolet and photoelectron spectroscopy measurements showed new electrostatic states upon water adsorption on magnetite. These features were assigned to OH species[65, 66, 67, 68], meaning that water dissociation occurs. TPD experiments of water adsorbed on $Fe_3O_4$(111) in the low coverage regime revealed desorption peaks of chemisorbed water in a broad range of temperatures between 200 K and 400 K[68, 69, 70]. Here, signals above 300 K were attributed to the recombinative desorption of dissociated water. Also, the heat of adsorption measured in the low water coverage regime by use of single crystal microcalorimetry provided a value of 100 kJ/mol, which rapidly decreases to 55 kJ/mol with increasing coverage[51]. The first infrared study on the water interaction with $Fe_3O_4$(111) was performed by Leist et al.[70] In their paper they report that water adsorbates on magnetite exhibit two adsorption bands at 2712 $cm^{-1}$ and 2691 $cm^{-1}$. These IRAS features were in the first place assigned to $O_wD$-$Fe_{tet1}$ and $O_sD$ species consequent to water dissociation, where $O_wD$ and $O_sD$ are hydroxyl groups involving oxygen atoms from the water itself and from the oxide surface, respectively. However, this assignment was doubted in a recent IRAS study[51], which invoked an octahedral terminated magnetite surface ($Fe_{oct2}$-) to rationalize the spontaneous formation of a water complex consisting of a dissociated and a non-dissociated water molecule (known as a "half-dissociated dimer"). On the contrary, room temperature STM on a $Fe_3O_4$(111) single crystal showed water–related species formed upon water dissociation only on $Fe_{tet1}$-terminated surfaces[66, 71]. In general it is important to point out that the initial stage of the water adsorption process on magnetite was found to be quite challenging to image, especially because of the high reactivity of Fe-terminated $Fe_3O_4$ towards traces of water in the UHV background[72]. Indeed, STM images of "fresh prepared" $Fe_3O_4$(111) films showed adsorbate-like species even without water exposure.

Water adsorption on magnetite was also investigated from the theoretical point of view, and the first studies were performed on a $Fe_{tet1}$-terminated surface, as the most stable one. Several groups have calculated the adsorption energy for the dissociative

water adsorption structure and a value of 95.4 kJ/mol was reported by Grillo et al.[73], while Rim et al. obtained 126 kJ/mol, which seems to be more stable than molecular adsorption by 47 kJ/mol[71]. Furthermore, calculations performed by Li et al. revealed reported adsorption energy for dissociated water on $Fe_{tet1}$-terminated magnetite of 66 kJ/mol, which is considerably lower than what was previously observed and only 14 kJ/mol more stable than molecular adsorption[74]. The agreement between all theoretical studies is reached at higher water coverage regime (when the coverage increases up to two water molecules per unit cell), where a unified picture of a dimer composed of a dissociated and a non-dissociated water molecule is proposed. Still, substantial controversy remains in the literature regarding the role of the surface termination. On the one hand, theoretical calculations from Yang et al. predicted that the $Fe_{tet1}$-terminated surface favors the interaction with water[75], whereas the $Fe_{oct2}$-termination was found to be more active towards water adsorption by Zhou et al.[76] The latter study came to the conclusion that direct water dissociation is unfavorable, but it can indeed be promoted by the presence of neighboring water molecules.

It is quite clear that the initial stages of water adsorption on $Fe_3O_4(111)$ surfaces is a challenge that has not been fully overcome yet. The main reason for the controversy found in the literature is probably related to the experimental difficulty to prepare a well-defined uniform $Fe_3O_4(111)$ surface. As mentioned in the Section 3.2, one of the achievements of this work is to eliminate the apparent discrepancy between tetrahedral- and octahedral-terminated surfaces, preparing a well-ordered and uniform $Fe_3O_4(111)$ film. Hence, the next research goal for this thesis is to revisit a previous study on the water adsorption on magnetite[51], rationalizing it in the new framework of a uniform tetrahedrally terminated surface.

## 2.5 $CO_2$ on Metal Oxide

Until the early 80s, the surface chemistry of carbon dioxide has received relatively little attention in comparison with other small inorganic molecules. The interest on $CO_2$, earlier less pronounced probably due to its thermodynamic stability[77], changed rapidly in direction when it was found that carbon dioxide was a key reactant in the methanol synthesis[77]. With the passing years, $CO_2$ has become also one of the most important greenhouse gases[62]. Indeed, its efficient conversion into fuels or other value-added chemicals would result in both the reduction of the $CO_2$ emission in the atmosphere and in minimizing the society dependence on fossil fuels[78, 79]. Besides, the use of water as hydrogen resource (instead of molecular hydrogen) for $CO_2$ reduction/hydrogenation would be the most ideal process. However, $CO_2$ represents the most oxidized state of carbon which makes its chemical transformations thermodynamically highly unfavorable[77]. The two main ways to overcome this problem are, on the one hand, high temperature and pressure conditions and active reducing agents such as hydrogen, or, on the other hand, activation on a solid-state catalyst with the ability to adsorb the $CO_2$ and facilitate electron transfer to it. It is possible to find in the literature an appreciable amount of material for carbon dioxide adsorption on metal surfaces (summarized in two comprehensive reviews from Solymosi[80] and Freund and Roberts[77]), whereas a similar database for metal oxide surfaces does not exist.

It is instructive here to summarize the key experimental findings of previous studies on $CO_2$ adsorption on metal/metal oxide surfaces. The most stable intermediates observed during reactions involving CO and/or $CO_2$ seem to be carbonates[81]. Haruta et al.[82] showed that bidentate carbonates are formed at 300 K upon CO adsorption at the perimeter of Au nanoparticles supported on $TiO_2$. In this case carbonates act as intermediates towards $CO_2$ formation. Later it was found that a considerable number of different carbonate species may (co-)exist on metal oxides such as alumina[81], magnetite[83], MgO[84] or ZnO[85, 86, 87] and they can be distinguished using, e.g., infrared spectroscopy. Particularly, the non-coordinated carbonate ion is identified by an asymmetric vibration in the range 1420-1450 $cm^{-1}$ and a symmetric one between 1020 $cm^{-1}$ and 1090 $cm^{-1}$. Monodentate carbonates (covalently bound) exhibit IRA bands at 1470-1530 $cm^{-1}$ ($\nu_{as}$ $COO^-$), 1300-1370 $cm^{-1}$ ($\nu_s$ $COO^-$) and 1040–1080 $cm^{-1}$ ($\nu$ C-

O). Furthermore, bidentate carbonates may form into different binding geometries known as bidentate-chelating and bidentate-bridging (more details can be found in Ref. [81]). Wang et al.[88] observed an unusual tridentate carbonate species on the surface of ZnO(10–10) single crystals. Additionally to carbonates, bicarbonates or formates species can be formed[81]. Bicarbonates usually show a supplementary band around 1180-1250 $cm^{-1}$, whereas formates can be differentiated because of the characteristic band in the C-H stretching region[84, 89] (≈ 2750–2950 $cm^{-1}$). Although it seems quite well accepted that carbonates are the most stable intermediates[90, 91, 92, 93, 94] in the $CO_2$ activation process, they are not the only ones. In fact, other less stable intermediates exist, such as oxalate ($C_2O_4^{-2}$), carboxylate (bent $CO_2^-$) and $CO_2^{2-}$ species[95]. The vibrational assignment of these species has been difficult and often highly controversial. The difficulty in their characterization, in particular in the case where several intermediates are simultaneously present at the surface, originates from the overlap of the vibrational bands for carbonate, bicarbonate, oxalate, carboxylate and $CO_2^{2-}$ species, which fall all in the 1000-1900 $cm^{-1}$ range[95].

The identification of the $CO_2$ intermediates formed on $Fe_3O_4$(111) (and 100), employing isotopic substitution and their interaction/dependence towards water on the surface is one of the accomplishments of this work.

# 3. Theoretical Background and Experimental Methods

This chapter is divided into two sections. In the first sections some general aspects of kinetics at the gas-surface interface (3.1), and surface energy (3.2), will be presented. In the second Section (3.3), the physical working principle of the most important experimental methods applied in this work will be described. Finally, Section 3.4 shows the experimental setup as well as the details concerning the reactants employed during the experiments presented in this work.

## 3.1 Gas-Surface Interaction

Heterogeneous catalysis is defined as a kinetic phenomenon based on the interaction between the surface and the gas (or liquid) phase. In every catalytic reaction, even the simplest cases, a number of elementary reaction steps have to be considered.

In this section the basic processes that can occur on a surface will be briefly presented. More specific summaries can be found in the literature[11,96–98].

**Scattering:** the molecules (or atoms) from the gas phase can either be elastically or inelastically scattered. In the case of elastic scattering, the scattering angle is identical with angle of incidence and no energy transfer occurs. Inelastic scattering processes are instead characterized by energy transfer, thus the surface can be heated or cooled by these events[11,96,97].

**Trapping:** when the incident molecule looses sufficient momentum along the surface normal, for example through coupling to its momentum parallel to the surface or suface phonons, it becomes thermally equilibrated with the surface and trapped on it. This procces is mostly associated with a non-activated, non-dissociative physisorption. The trapped molecule can either adsorb directly in a more strongly binding state or diffuse over the surface before desorbing or adsorbing in a stronger binding state[11,97,98].

**Adsorption-Desorption processes.** The adsorption process involves the interaction of species in the gas phase with solid surface. The rate of adsorption depends on two parameters: flux of impinging species at the surface and the sticking coefficient (see below). The first parameter is given by the Hertz-Knudsen equation:

$$F = \frac{P}{\sqrt{2\pi mkT}} \tag{3.1}$$

where $P$ is the gas pressure expressed in $N \cdot m^{-2}$, $k$ is the Boltzmann constant, $m$ is the molecular mass of the impinging molecules expressed in $kg$, and $T$ is the absolute temperature, expressed in $K$. Therefore, the adsorption rate is given by:

$$R_{ads} = FS \tag{3.2}$$

with $S$ as sticking coefficient. The sticking coefficient gives the ratio of the number of adsorbate species that adsorb ("sticks") to the surface to a total number of molecules impinging upon the same surface during the same time period. Its value oscillates typically between 0 (no species sticks to the surface) and 1 (all species stick to the surface) and depends on several factors such as the substrate temperature, the temperature of the incoming molecules, the number of adsorption sites on the surface (it decreases with decreasing of number of available sites). Under high availability of adsorption sites on the surface and low temperature conditions where the adsorbate can form condensed multilayers, it is possible to assume a constant sticking coefficient.

In general, adsorption of molecules from the gas phase onto the solid surface takes place when attractive forces exist at short distance between them. It is possible to distinguish two principle modes of adsorption at the surface: physisorption and chemisorption. The distinction between the two modes depends on the nature of the bond between molecules and surface. The weakest interaction with an attractive nature between adsorbate and surface is the *van der Waals interaction*, which originates from the synergy of a fluctuating dipole in the adsorbates with a polarizable surface. A van der Waals bonding can be described as the interaction between two point-dipoles and, in the case of bonding to a surface, the attractive potential has a distance dependence proportional to $r^{-3}$. However, as the atom is brought closer to the surface, the overlapping of the electron cloud of the adsorbate leads to a steep increase of kinetic

energy of the electrons and hence a high repulsive potential[99]. A physisorption potential is the sum of the repulsive and attractive Van der Waals contributions (see the energy potential diagram in Fig. 3.1).

When there is an overlap between electronic orbitals of the adsorbate and the surface, leading to a chemical bond having energies higher than $50kJ/mol$, a chemisorption occurs. Chemical bonds are typically ionic or covalent and it is possible to distinguish between three types of chemisorption: a) molecular chemisorption, b) non-activated dissociative chemisorption, c) activated dissociative chemisorption[100]. As it is shown in Fig. 3.1, the potential energy curve is described as a combination of physisorption and chemisorption.

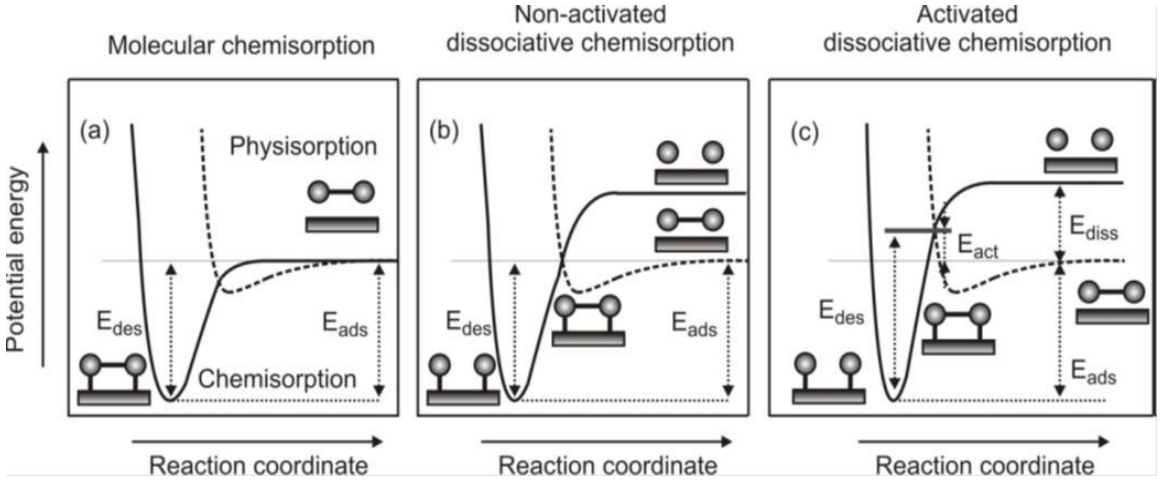


*Fig. 3.1. Schematic potential diagram for (a) molecular chemisorption, (b) non-activate dissociative chemisorption, (c) activated dissociative chemisorption of a diatomic molecule. Solid line curve: the total potential energy curve.*
*The figure is adapted from Ref.*[100]

In the energy diagram, the region on the left of the crossing point between the two curves is characterized by chemisorption. The depth of the adsorption well gives the adsorption energy $E_{ads}$, a measure of the strength of the bond to the surface. The desorption of an adsorbed species from a surface is considered to be the reverse process of adsorption. In the cases (a) and (b) in Fig. 3.1, the desorption energy ($E_{des}$) is equal to $E_{ads}$ The dissociative chemisorption is often an activated process, and therefore an activation barrier ($E_{act}$) has to be overcome. In this case the desorption energy can be written as follows:

$$E_{des} = |E_{ads}| + |E_{act}| \tag{3.3}$$

The potential energy diagram for an activated dissociative chemisorption process is shown in the Fig. 3.1 (c). When a diatomic molecule approaches the surface from a large distance, it interacts in the first place physisorbing on the surface. If the molecule possesses kinetic energy high enough to overcome the activation barrier, it may dissociate. The dissociated species can then interact with the surface in a chemisorbed state. The corresponding potential energy curve for two atoms differs from the one of a molecule for the term dissociation energy $E_{diss}$.

**Diffusion:** after adsorption, the molecules can diffuse across the surfaces or desorb into the gas phase. It is an activated process, which means that the molecule, in order to diffuse, has to overcome an energetic barrier. The activation barrier for diffusion is generally lower than the one for desorption. Considering that both processes are driven by thermal fluctuations, the surface temperature critically governs their rate.

The diffusion constant is described by an Arrhenius-like equation with the pre-exponential factor $D_0$ and the activation energy for the diffusion[96]:

$$D = D_0 \exp\left(\frac{-E_{diff}}{k_B T}\right) \tag{3.4}$$

When $E_{diff} \gg RT$, the species are strongly bound and have to overcome a significant activation barrier between different adsorption sites and therefore the diffusion over the surface resembles a hoping motion along the path of minimum activation energy. In the case of $E_{diff} \ll RT$, the molecules are free of diffusing in a Brownian motion-like.

The desorption rate can be written as follows:

$$\frac{-d\Theta}{dt} = \Theta^n k_0^{des} exp\left(\frac{-E_{des}}{k_B T}\right) \tag{3.5}$$

Where $n$ is the desorption order, $k_0$ is the pre-exponential factor for desorption, and $E_{des}$ the activation barrier for desorption[96].

**Reaction on surfaces:** generally, reaction on surfaces can occur through two different mechanisms, Langmuir-Hinselwood (LH) and Eley-Rideal (ER) [101], as it is shown in Fig.3.2.

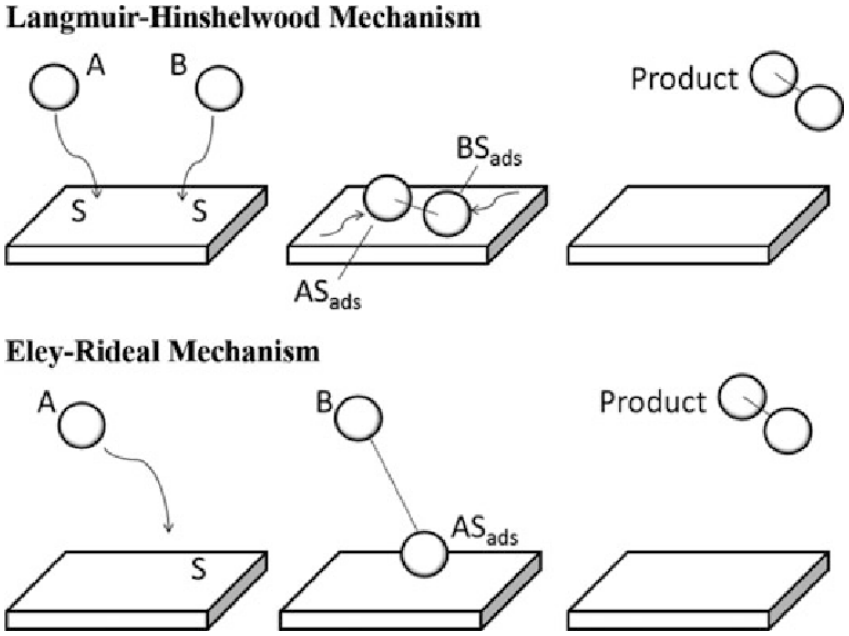


*Fig 3.2. Langmuir-Hinselwood (LH) and Eley-Rideal (ER) mechanisms. In the LH mechanism both reactants are fully accommodated on the surface. In the Eley-Rideal the reaction occurs directly at the point of impact between an incident and an adsorbed species*[101]*). The Figure is adapted from Ref*[102].

Most of the reactions take place via LH mechanism, where both reactants are already present on the surface before the reaction starts. The following steps are likely to happen in this mechanism: physisorption in a precursor state, diffusion across the surface to different sites, and chemisorption (dissociation is not necessary). Finally, the molecules can react and then desorb into the gas phase.

In terms of reaction rate, if A and B are the reactants and AB is their product after reaction, the formation rate of the AB product can be written as follows:

$$\frac{d\Theta_{AB}}{dt} = k_0^{LH} exp = \left(\frac{-E_{act}^{LH}}{k_B T}\right) \Theta_A \Theta_B \tag{3.6}$$

where $\Theta_A$ and $\Theta_B$ are the surface coverages of the species A and B, $E_{act}^{LH}$ is the activation energy for the reaction, and $k_0^{LH}$ is the pre-exponential factor.

The ER mechanism is less common compared to the LH and characterizes rare reactions occurring between a species on the surface and an incident one which has

not yet equilibrated to the surface. Details and evidences for both mechanisms can be found in the literature[96,97].

### 3.2 Surface Energy

The surface energy is defined as the quantification of the intermolecular bonds that occur when a surface is created. Normally, the molecules on a surface have higher energy compared to the one in the bulk of the same solid. Thus, surfaces are intrinsically less energetically favorable than bulks, otherwise there would be a driving force creating surfaces and removing the bulk of the material. Therefore, the surface energy can be identified with the excess energy at the surface of a certain solid in comparison with the bulk energy. Another way to define it is to relate it to the work to create a certain area of a particular surface, or to the work to cut a bulk sample and obtain two surfaces. When a solid is cut into pieces, its bonds are being disrupted and its surface energy increases. When the cut is reversible, the energy that has been consumed during the cutting process has to equal the surface energy for the new surfaces created. In this way, the unit surface energy of a material would be the half of its cohesion energy. Actually, this happens only for surfaces which are prepared in ultra-high vacuum. Indeed, surfaces change often their form by means of simple cleavage and are dynamic systems ready to react or rearrange for reducing their energy.

For example, in the case of magnetite, both natural and synthetic crystals have often octahedral shape embedded in (111) planes[40], although different kind of shapes and size can be grown modifying for instance the pH of the respective solution during the growth[103]. A very widely used method for the comparison of the surface energies of the low index facets of $Fe_3O_4$ is density functional theory[104,105,58]. Using this approach, surface energies of 0.96 $J \cdot m^{-2}$ and 1.10 $J \cdot m^{-2}$ have been calculated for the (100) and the (111) facets respectively. Despite the fact that the surface energy depends strongly on the surface termination has to be taken into account, it is legitimate to consider the energy trend (100) < (111) < (110) for the different facets plausible.

## 3.3 Basic Techniques

This section describes the technical and experimental fundamentals of the methods applied in this thesis. In the first part (3.3.1), the theory of the molecular beams will be discussed, focusing on the effusive beams, used in this work, and a small mention on the supersonic beam, part of the experimental setup but not employed for this study. The next part will focus on the surface science detection methods and their physical background employed in this thesis: infrared-reflection-absorption spectroscopy (3.3.2), quadrupole mass spectrometry and temperature programmed desorption (3.3.3), low energy electron diffraction (3.3.4).

### 3.3.1 Molecular Beam

Molecular beam techniques are well-established tools to study dynamics and kinetics of surface reactions and it is possible to find in the literature several reviews with a large number of case studies[106,107,11,98]. A detailed description of the molecular beam setup used in this work can be found elsewhere[10,108].

A molecular beam is a spatially well-defined, directed and collision-free flux of molecules, or atoms, which is typically produced in a beam source such as showed in Fig. 3.3. A gas expands from a gas reservoir (so-called stagnation state, $p_0$, $T_0$) into a vacuum chamber. The properties of the molecules in the expansion depend on the specific conditions (see below). A skimmer (aperture) cuts a small solid angle to produce a direct beam that can be further modified in many ways. For example, the flux can be modulated using a mechanical chopper or shutter. In order to separate the molecular beam from the effusive background of molecules, several differential pumping stages are implemented. The pumping speed in the first expansion typically limits the achievable flux.

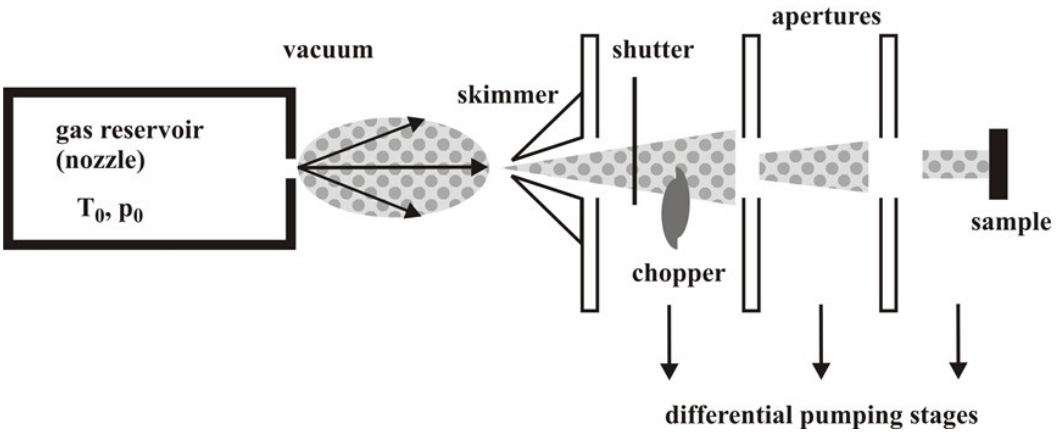


*Fig.3.3. Schematic illustration of a molecular beam source. The figure used is adapted from Ref.*[10,108]

Finally, after the last pumping stage, the beam will enter the scattering chamber and hit the sample at the desired angle of incidence.

The main advantage of using a molecular beam over a simple reactor is given by the possibility to perform experiments under *single scattering conditions.* This means that every molecule will interact only once with the sample surface in an otherwise collision-free environment. The collision-free environment allows several new experimental options which will be discussed briefly as follows.

1. *Possibility to determine the absolute reaction probability*. Since the incidence flux is known, it is possible to have access to the absolute probability of different reactive processes (i.e. sticking coefficient in the case of adsorption). Experiments to determine the sticking coefficient have not been performed in this work, but it is still worth to mention how the experimental setup can be used to execute them. The procedure is based on the experiment developed originally by King and Wells[109]: a molecular beam is directed to the sample and the partial pressure of the species of interest is detected. At the beginning of the experiment the shutter between the beam and the sample is kept closed, so that the beam is blocked. As soon as the shutter is opened, the partial pressure decreases due to partial absorption. The change in the pressure is related to the absolute sticking probability. This method allows determining sticking probabilities in the range between $10^{-2}$ and 1. It must be taken into account that i) for

lower values, detection of surface species is superior to the gas phase analysis, ii) for reactive gases the interaction with the chamber walls may slow down the response of the vacuum system.

The determination of absolute adsorption/reaction probability gives the possibility to compare reaction rates as function of surface parameters.

2. *Fast and flexible reactant flux modulation*. The flux modulation plays a key role in kinetic and dynamic experiments because it allows to precisely study transient processes. Different kind of modulated beam experiments give fundamental information on the kinetics and the mechanism of surface reactions.
3. *Isothermal reaction conditions*. Most of the molecular beam experiments operate under isothermal conditions, meaning simplifying the analysis of the kinetics.
4. *Collision-free detection of scattered and desorbing molecule.* Local pressures at the sample position are up to $10^{-4}$ mbar and are several orders of magnitude higher than the background pressure. Therefore, atoms or molecules that are being scattered or desorbed from the surface can be detected as they are in a collision-free environment. Several information are available due to this direct detection, such as the angular distribution of reactant molecules, their kinetic energy, their rotational or vibrational energy distribution[107,98,110,111]. With this kind of studies is possible to have access to details on the potential energy surfaces, which determine desorption and reaction events or scattering processes.

It is possible to distinguish two limiting cases regarding molecular beam sources: *effusive* and *supersonic* beam sources. The differences between the two categories are related to the expansion conditions, generating different types of energy distribution of the molecules in the beam[112].

**Supersonic Beam**

The expansion conditions (temperature and pressure in the gas reservoir and in the expansion stage) have a huge effect on the properties of the molecules or atoms in the beam. The expansion conditions can be described by the Knudsen number, $K_n = \frac{\lambda}{d}$, with λ = main free path of molecules and d = diameter of the nozzle. A supersonic beam is formed at low Knudsen number conditions ($K_n \ll 1$) and it is characterized

by narrow velocity distribution of molecules. This resembles to a supersonic expansion from a gas reservoir with a high pressure, where collisions between molecules are frequent, through a small nozzle into a vacuum chamber. A scheme of a supersonic beam source is shown in Fig. 3.4.

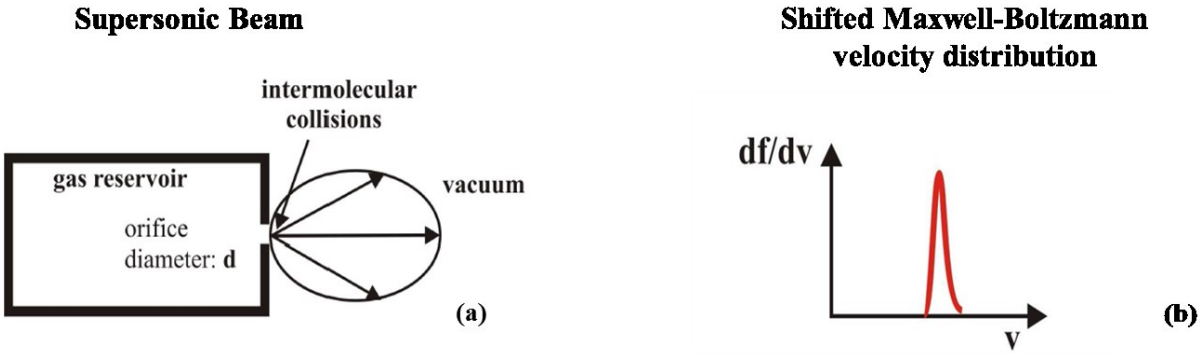


*Fig. 3.4. Schematic representation of a supersonic beam. The figure used is adapted from Ref.*[10,108]

Typically, the gas starts in the stagnation stage ($p_0$, $T_0$) with a negligibly small velocity, and then accelerates towards the source exit. Under sufficiently extreme conditions the flow reaches sonic speed as it exits the nozzle, and supersonic speed upon further expansion. Due to the small mean free path of the molecules, numerous collisions occur in the nozzle during the expansion and this results in an efficient cooling of the gas. From this part of the expansion a solid angle of the beam is extracted by means of a skimmer and it is then collimated by further apertures and modified by choppers or shutters. Following the trend of the velocity of the molecules ($v$) as a function of the distance from the source[112], it is seen that $v$ approaches an asymptotic value, whereas the translational temperature, density and collision frequency decrease drastically. The translational temperature $T_{||}$ characterizes the width of the parallel velocity distribution for the flux $I_{||}$, which is typically described as a shifted Boltzmann distribution:

$$I_{||} = N\, v^3 exp\left(-\frac{M(v-v_{II})^2}{2kT_{||}}\right) \tag{3.7}$$

with $v_{II}$ = parallel flow velocity and $M$ = molecular mass of the molecules in the beam and N is a normalization factor[10].

In summary, the main advantages of a supersonic beam source are: i) the narrow velocity distribution, ii) the variable kinetic energy and iii) the large degree of control over the internal energy. Thus, the main application fields of supersonic beam studies are the dynamics of gas-surface interactions, scattering and diffractions studies, which require well-defined monochromatic beams.

**Effusive Beam**

An effusive beam is formed at large Knudsen number conditions ($K_n \gg 1$). A relatively low pressure is applied in the gas reservoir ($p < 1\,mbar$) which is sufficiently low to maintain the molecular flow. These conditions result in a low collision frequency and, therefore, the energy distribution remains constant during the expansion. The velocity distribution follows the Maxwell-Boltzmann distribution (Fig. 3.5b):

$$I = Nv^3 exp\left(-\frac{Mv^2}{2kT_0}\right) \tag{3.8}$$

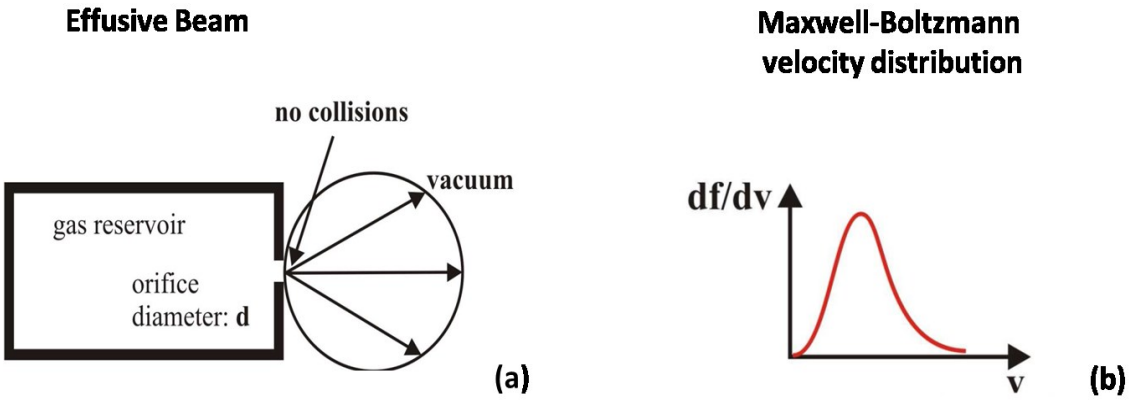


*Fig. 3.5. Schematic representation of an effusive beam. The figure used is adapted from Ref.*[10,108]

There are several types of effusive sources that can be used in the kinetic experiments: the thin wall orifice (Fig. 3.5a), the single channel and the multi-channel array (Fig. 3.6). The simplest case is the thin-wall orifice, where the orifice produces a cosine

angular flux distribution. Only a small solid angle is extracted in order to produce the beam, while the rest will be pumped out by differential pumping. A substantial portion of molecules is not able to contribute to the beam because of the low directionality of the expansion, causing low intensities of the beam and requiring high pumping speeds. Is this case, the available pumping speed is the limiting factor for the maximum beam intensity. It is possible to improve the directionality, and therefore the intensity, of the beam using channels with a strongly angle dependent transmission probability instead of thin-walled orifice. In the absence of intermolecular collisions, only the molecules moving in the direction close to the centerline can pass through the channel. This results in the formation of the well-collimated flux of molecules. Typically, the collimation effect of the channel depends on the length to radius ratio of the channel itself and it is described as function of the peaking factor (κ), which equals the ratio of the center-line intensity of the actual distribution $I(0)$ and the center-line intensity of the cosine distribution at identical total flux $\dot{N}$. For long enough tubes and at low pressure, κ can be approximated as follows[112-10]:

$$\kappa = \frac{\pi}{\dot{N} I(0)} = \frac{3L}{8r} \tag{3.9}$$

With typical length to radius ratio $\frac{L}{r} = 40$, peaking factors of 15 can be reached, while in the case of supersonic beam enhancement of less than 2 are displayed.

With increasing pressure in the gas reservoir, the mean free path decreases, thus intermolecular collisions inhibit the increasing flux, leading to broadening of the angular distribution and deviation of the Maxwell-Boltzmann velocity distribution. While, on one hand, for tubes with smaller overall dimensions the above discussed pressure limit is higher, on the other hand in small channels the total flux of molecules is low. As shown in Fig.3.6, the use of several parallel arrays of small channels (multi-channel arrays, MCA) allows overcoming this issue. In this way it is possible to have a collimation effect at high stagnation pressure and thus at high total flux.

In the case of effusive beams, the main advantages are the following: i) having a variable beam flux over several orders of magnitude without changes of the beam properties; ii) high maximum intensities despite the moderate pumping speed; iii) low backing pressures, conceding the use of chemicals with low vapor pressures and also

reducing the consumption of gas (this point be particularly important when using expensive reactants like isotopically labeled molecules).

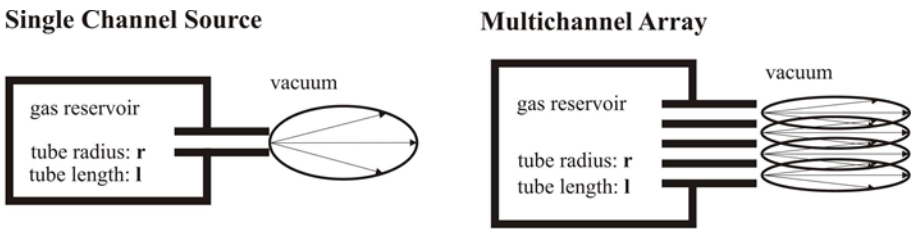


*Fig.3.6 Schematic illustration of the focusing effect of a capillary and capillary array of a gas flux. The figure used is adapted from Ref.*[10,108]

### 3.3.2 Infrared Spectroscopy

Infrared spectroscopy (IR) is a powerful technique to detect the interaction between adsorbates and surface. Molecular vibrations are excited by adsorption of IR light and their frequency provides detailed information about chemical bonds and thus about the interactions of the molecules with the metal surface[113–115]. The adsorption frequencies of covalent bonds in some molecules, *e.g.* CO, are related not only to the surface, but also to the specific adsorption site where they are sitting. Therefore, CO adsorption is often used to characterize the morphology of the surface (see Chapter 4).

**Molecular Vibrations**

The excitation of molecular vibrations by electromagnetic radiation can be described using the time-dependent perturbation theory. In the case of wavelength λ bigger than the dimensions of the excited vibration (always valid for IR radiation), the electric field $\vec{E}$ induced by the electromagnetic radiation is approximately constant over the size of the excited dipole[116]. Thus, the Hamiltonian operator $H^{(1)}$ of the perturbation can be written as follows:

$$H^{(1)} = -\vec{\mu} \cdot \vec{E} \tag{3.10}$$

where $\vec{\mu}$ is the electric dipole moment of the molecule and $\vec{E}$ the electric field vector of the electromagnetic radiation[117]. In line with Fermi's golden rule, the excitation probability is given by:

$$W \propto \left|\langle \psi_f | \vec{\mu} \cdot \vec{E} | \psi_i \rangle\right| \tag{3.11}$$

with $\psi_f$ and $\psi_i$being the vibration eigenfunctions in the excited and ground state. Within the Born-Oppenheimer approximation of the independent electron and nucleus motion, the wave function can be factorized to the vibrational and electric components, $\nu_k$ and ϵ respectively:

$$\psi = |\langle \epsilon, \nu_k' | \vec{\mu} | \epsilon, \nu_k \rangle| \tag{3.12}$$

Where $\nu_k$ and $\nu_k'$ are the vibration eigenfunctions before and after the excitation. In this approximation the two terms can be treated separately. Therefore, the probability for a vibrational transition along the normal coordinate $Q_k$ is:

$$\langle \nu_k' | \vec{\mu} | \nu_k \rangle = \left\langle \nu_k' \middle| \vec{\mu} + \sum_i \left(\frac{d\vec{\mu}}{dQ_i}\right)_0 Q_i + \cdots \middle| \nu_k \right\rangle = \left(\frac{d\vec{\mu}}{dQ_k}\right)_0 \langle \nu_k' | Q_k | \nu_k \rangle \quad (3.13)$$

Therefore, a vibration is IR-active if it is associated with an oscillating dipole moment:

$$\left(\frac{d\vec{\mu}}{dQ_k}\right) \neq 0 \quad (3.14)$$

The derivative $\frac{d\vec{\mu}}{dQ_k}$ is denoted as *dynamic dipole moment of the molecule* along the normal coordinate $Q_k$ .

**Fourier-Transform Infrared Spectroscopy**

Nowadays, the most commonly used IR spectrometers are Fourier-transform (FT) spectrometers [113,114]. They present several advantages over the dispersive spectrometers which/that were mostly employed in the past. Dispersive spectrometers work by dividing polychromatic IR light by gratings on prisms. As consequences of the monochromatization procedure, disadvantages such as low beam intensities, low detection limits, long times required for the spectra acquisition with a reasonable resolution and signal-to-noise ratio, emerge. Fourier-Transform spectrometry can help to overcome these drawbacks. In fact, in FT-IR the sample is exposed to light from a wide spectral range and all the frequency components are collected simultaneously. The measured quantity in FT-spectroscopy is the interference signal from a two-beam interferometer. Most of the interferometers used today are based on the setup of the original one designed by Michelson. In more details, a Michelson interferometer is a device that splits the beam of radiation into two paths and then recombines the partial beams. Fig. 3.7 shows a simple form of the interferometer. It consists of two mutually perpendicular plane mirrors, one of which can move along the axis shown. Between the fixed and the movable mirror, a *beam splitter* is located, at which the beam is partially reflected to the fixed mirror and partially transmitted to the movable mirror.

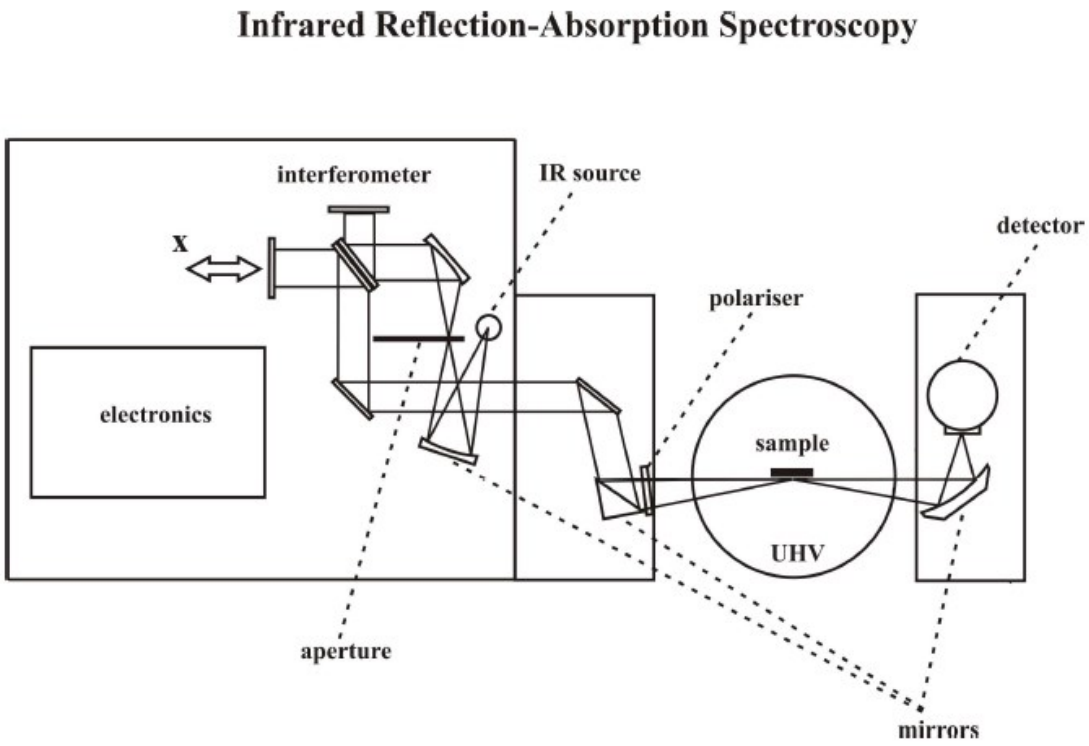


*Fig. 3.7. A schematic illustration of the in-situ IRAS setup (FT-IR spectrometer containing a Michelson interferometer). The figure used is adapted from Ref.*[30]

Each beam is reflected back to the beam splitter, where the superposition of both beams causes the interference. The resulting beam intensity *I(x)* is measured by the/a detector as a function of optical path difference *x*. The function *I(x)* is termed the interferogram and contains all the information accessible in an IR experiment[118]. Depending on the path difference *x*, constructive or destructive interference can occur. If the path difference *x* is zero, constructive interference of all waves occurs, leading to the maximum in the interferogram. Away from this position most waves undergo partially or totally destructive interference, resulting in rapidly decaying oscillations on both sides of the maximum. Ideally, the interferogram should be symmetrical. However, experimental interferograms are usually asymmetrical due to certain electronic and optical effects in the spectrometer. A numerical phase correction is applied in this case to improve the quality of the resulting spectrum. Even if a single scan of the mirror position can be sufficient to provide an interferogram, the mirror is usually scanned N times to improve the signal-to-noise ratio. The interferogram *I(x)* is

then converted into a spectrum that describes the measured intensity as a function of the wavenumber $\tilde{\nu}$:

$$S(\tilde{\nu}) = \frac{1}{2\pi}\int_{-\infty}^{\infty} I(x)e^{-2\pi\tilde{\nu}x}dx \tag{3.15}$$

where $\tilde{\nu} = \lambda^{-1}$. The obtained spectrum is termed *single channel spectrum*. The single channel spectrum contains additional absorption signals due to the optical setup, detector function and due to the adsorbed molecules on the sample. The strategy to eliminate the contributions from these factors is to divide the sample spectrum by another single channel spectrum, called *reference*, obtained before using the very same optical setups, but with no adsorbates.

**Infrared Spectroscopy on Surfaces**

The vibrations of molecules adsorbed on planar model surfaces, which are not transparent to the IR light, are often detected using a method called infrared-reflection-absorption spectroscopy (IRAS) [116–118]. This method is generally used on thin dielectric films deposited on top of metal surfaces, which acts as mirrors assuring high signal intensity in reflection geometry. It has to be taken into account that, due the dielectric behavior of the metal, there is a difference between the adsorption of the IR light by a molecule adsorbed on a metal surface and a molecule in the gas phase[119–121]. In the gas phase, the electric field of the incident infrared light interacts only with the dipole moment of the molecule, exciting in this way the molecular vibrations. However, on metal surfaces both the incident IR light and the dipole moment of the adsorbed molecule interact with the metal electrons. Therefore, a strict *metal surface selection rule* (MSSR) is imposed from the metal surface. First of all, IR-active vibrations are only the ones having a dynamic dipole moment or a non-zero component perpendicular to the metal surface, i.e. for which

$$\left(\frac{\delta\vec{\mu}}{\delta Q_k}\right)_{\perp} \neq 0 \tag{3.16}$$

Fig. 3.8. shows what happens to the parallel component of the dynamic dipole $\left(\frac{\delta\vec{\mu}}{\delta Q_k}\right)_{\parallel}$: this is being screened by the metal electrons, which are fast enough, on the time scale

of molecular vibrations, to generate an imaged dipole moment that cancels the parallel component of the dynamic dipole[122].

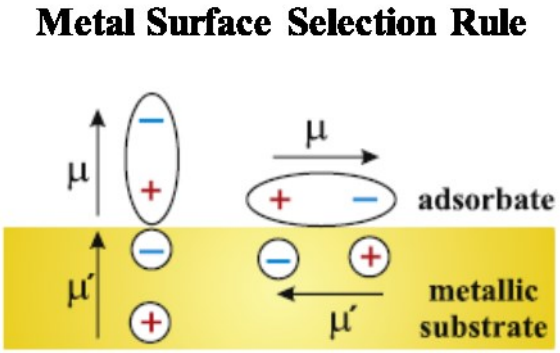


*Fig. 3.8. The metal surface selection rule and screening of the parallel component of the dynamic dipole. The figure used is adapted from Ref* .[122-123]

Besides, molecular vibrations on metal surfaces can be excited only by a radiation having a component parallel to the plane of incidence (p-polarized light)[123]. In fact, the s-component of the electric field at the surface goes through a uniform phase shift of 2π for all angles of incidence. This implies that the electric field parallel to the surface vanishes due to destructive interference. Accordingly, it is not possible to excite vibrations parallel to the surface because of two factors: the screening of the vibrating dipole due to its image and the loss of the field component parallel to the surface. For these reasons the p-polarized light is usually used in the IRAS experiment. The phase shift for the p-light is strongly dependent on the incidence angle, and the maximum surface electric field as well as the maximum absorption intensity, is established at grazing incidence.

**IRAS of adsorbed molecules**

The IR-spectrum of adsorbed molecules can provide information related to the chemical state, e.g. if the molecule is dissociated, or to the strength of the metal-adsorbate bond which is known to affect the vibrational frequency shift, unlike in the case of molecules in the gas phase. Several effects on the vibrational frequencies, such

as *frequency shift*, *intensity of vibration*, *line shape and width of the adsorption band*, can be observed and their interpretation is usually based on specific models, briefly considered in the following.

**Frequency shift.** The frequency shift of an isolated adsorbed molecule can be affected by four important effects.

1. *Mechanical renomarlization.* The adsorption of a diatomic molecule (e.g.) CO to a rigid surface will give rise of a purely mechanical shift of internal frequencies of the molecule (e.g. C-O stretch). The shift can be predicted using a simple model of masses and springs. In case of the metal–C–O system, the C–O stretching is affected by a blue shift (to higher wavenumbers) of 50 $cm^{-1}$ as compared to the gas phase. In case of a vibrating substrate, additional renormalization appears[115,117–120,123,124]. The renormalization model predicts a frequency shift to higher wavenumbers. However, experimental results mostly indicate lower frequencies for adsorbed molecules. This indicates that this model alone is not sufficient to describe the experimental results.
2. *Polarization effect.* The dynamic dipole moment of an adsorbed molecule induces an image dipole in the metal substrate. The interaction between the dynamic dipole moment and its own image tends to lower the vibration frequency (red shift).
3. *Chemical shift.* The chemical shift derives from the chemical interaction between the molecule and substrate. A theoretical description of this phenomenon in the case of CO is given by Blyholder[125,126]. This model defines the CO bond with the metal substrate as deriving from a charge transfer from the 5σ molecular orbital of CO into the metal, and a "back-donation" from the metal d-bands to the unoccupied 2π* molecular orbital of CO. Whereas the 5σ orbital is weakly bonding, the 2π* orbital has strong antibonding character. Thus, the population of the 2π* molecular orbitals results in weakening the CO internal bond, giving rise of a red shift in the stretching frequency.
4. *Charge transfer.* Charge transfer between the metal surface and adsorbed molecule results in an electrostatic interaction, which may cause a frequency shift. Theoretical calculations predicted a shift of 10-20 $cm^{-1}$ for a single adsorbed non-polar molecule, such as CO[127].

   The sum of these effects results on an occurrence, widely used for surface site identification: the vibrational frequency of an adsorbate strongly depends on the nature

of the adsorption site on the surface. For example, the internal stretching of the CO molecule adsorbed on transition metals generally decreases with increasing of coordination number: the typical frequencies are observed around 1800-1900 $cm^{-1}$ for CO on threefold hollow sites, 1900-2000 $cm^{-1}$ for CO on bridge sites, and 2000-2100 $cm^{-1}$ for CO at on-top sites[127].

**Frequency shift due to adsorbate-adsorbate interaction.** Typically, as described above, the vibrational frequency of an isolated adsorbate molecule shows a red shift deriving from the interaction with the metal substrate. However, when the coverage increases, a blue shift is observed. This phenomenon arises from lateral interaction between adsorbates. The three major effects are the following:

1. *Dynamic dipole-dipole interaction.* When the distance between the molecules in an adlayer decreases, a spatial dipole-dipole coupling between neighboring dipoles and image dipoles becomes increasingly important.
2. *Chemical Shift.* The chemical shift has been already discussed on the bases of the Blyholder back-donation model for the example of CO-metal interaction. In the case of increasing coverage, adsorbate molecules compete for d-electrons from the metal orbitals, decreasing the degree of back-donation. Since the back-donation into the antibonding orbital lowers the frequency, this effect leads to a blue-shift.
3. *Static dipole-dipole interaction.* The vibrational frequency of an adsorbate is also affected by the electric field generated from neighboring static dipoles. This kind of interaction is typical for co-adsorption experiments where a considerably difference in the vibrational frequencies precludes dynamic dipole-dipole interactions. The frequency shift of an adsorbed dipole depends on its orientation relative to the electric field: a parallel orientation leads to a redshift, an antiparallel to the blue shift.

**Intensity.** The intensity of the IR absorption of adsorbed molecules is not only influenced by the MSSR, but also by adsorbate–adsorbate interactions. In the low coverage limit the intensity is proportional the number vibrating dipoles. With increasing coverage, however, all the above discussed effects on the value of the dynamic dipole must be taken into account. This results in a non-linear behavior of the absorption intensity as a function of coverage.

One frequently observed effect is known as *intensity borrowing*. This effect can lead to difficulties in identification of species on a surface. If a surface is populated with

two species with slightly different vibration frequencies, dipole–dipole coupling can result in intensity transfer from the IR adsorption at lower frequency to the one at higher frequency. This effect can result in strong changes in the intensity distribution between different species.

### 3.3.3 Mass Spectrometry and Temperature Programmed Desorption

Mass spectrometry is a very useful tool to investigate the chemical composition of the gas phase. The method uses the separation of gaseous ions according by their mass-charge ($m/z$) ratio. This technique is generally employed to examine neutral molecules and, therefore, these are first converted into ions by means of an ionizer. The ions that are generated can be singly or multiply charged and have masses corresponding to the original molecules or to their fragments. In the next step the ions go from the source to the mass analyzer: here a magnetic or an electric field, or a combination of both, will divide the ions into appropriate mass-charge groups. Ideally the ions travel from the source to the detector in a free-collision path, and this is possible when the gas pressure is below $10^{-5}$ torr (the mean free path is long compared to the ion trajectory). The setup is schematically illustrated in Fig. 3.9.

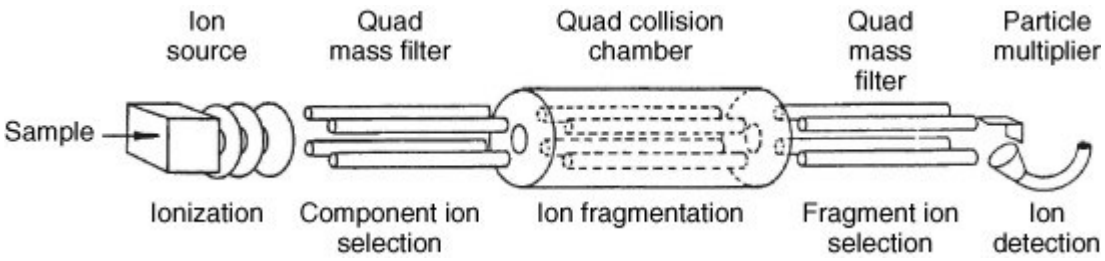


*Fig. 3.9. Illustration of the principle of the quadrupole mass spectrometer. The figure is taken form [http://what-when-how.com/proteomics/quadrupole-mass-analyzers-theoretical-and-practical-considerations-proteomics](http://what-when-how.com/proteomics/quadrupole-mass-analyzers-theoretical-and-practical-considerations-proteomics).*

**Ionization Process**

For the analysis of the gas compounds, electron and chemical ionization are the more often used ionization methods. The most common method (also used in this work) is the electron ionization (EI). For this, electrons $e-$ emitted from a cathode are accelerated onto the neutral molecules with energies ranging typically from 10-100 eV. Part of the kinetic energy can be transferred from the electron $e-$ to the molecule $M$ which is thereby ionized:

$$M + e^- \rightarrow M^{\cdot+} + 2e^- \tag{3.17}$$

Furthermore, if enough energy is transferred to the ion, fragmentation can occur:

$$M^{\cdot+} \rightarrow A^{\cdot+} + B \tag{3.18}$$

Typical values for the electron energies used in conventional mass spectrometers are around 70 eV.

**Mass analysis**

The mass spectrometers are usually divided into two categories, according to the type of field used for the mass separation: *static* instruments use static electric and/or magnetic fields, while *dynamic* ones use periodic fields. One of the most common dynamic analyzer, also used in this work, is the quadrupole mass analyzer, shown in Fig. 3.10. The analyzer behaves as “filter” where the ions are separated by the mass-to-charge ratio. Such filter consists of four electrical conducing rods, arranged in parallel.

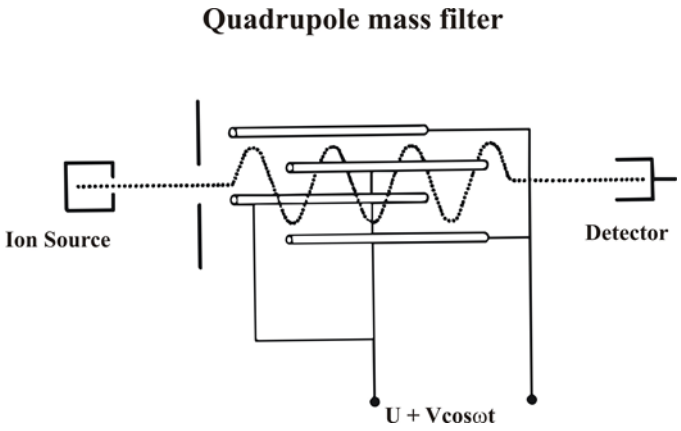


*Fig.3.10. Schematic representation of a quadrupole mass analyzer.*
*The figure is adapted from http://flashahead.info/category/q/quadrupole-mass-filter.*

Each opposing rod pair is connected together electrically, and a radio frequency (RF) voltage with a DC offset voltage is applied between one pair of rods and the other. Ions travel down the quadrupole between the rods. The resulting oscillating motion of the ions can be described by the *Mathieu equations*[128]:

$$\frac{d^2x}{dt^2} + \frac{e}{m_i r_0^2}(U + V cos\omega t)x = 0 \; ; \quad \frac{d^2y}{dt^2} + \frac{e}{m_i r_0^2}(U + V cos\omega t)y = 0 \qquad (3.19)$$

The ions move in an oscillating motion through the quadrupole mass filter. For a given parameters set $U$, $V$, $\omega$, only ions with a fitting $m/z$ ratio pass the filter on a stable trajectory in the $z$-direction parallel to the electrodes. All other ions on unstable trajectories leave the mass filter and are thus, not detected. During this mass selection, the ions are not accelerated or decelerated along the $z$-direction.

**Ion detection**

For the detection of ions different detectors may be used. In our setup, a channeltron electron multiplier (CEM) is applied as detector (see Fig. 3.11). CEM detectors are very commonly used today due to their high temporal resolution and high signal to noise ratio. However, CEM detectors require high vacuum conditions ($< 10^{-6}$ mbar) because of possible spark overs. CEM detectors consist of a small tube, typically made from glass, which is coated with a highly resistive material that emits electrons. Along the tube, a potential of $\sim 1 - 3$ kV is applied. The positively charged cations are

accelerated to the negatively charged entrance of the CEM where their impact onto the surface leads to the emission of electrons. These are attracted by the anode on the other side of the CEM. On their way, they create an avalanche of secondary electrons. In this way, amplification factors of up to $10^8$ can be achieved. When working at high fluxes, it is important to realize that the detected signal increases with flux only up to a certain threshold. When too many ions arrive simultaneously on the detector, the resulting electron flux will not increase linearly. This can be circumvented by *e.g.* reduction of the acceleration voltage. However, when signals of very high and very low intensities should be quantitatively detected simultaneously, this approach is not advantageous. In this case, one possibility is to follow the high intensity signal not on the maximum of the mass signal, but rather on a flank.

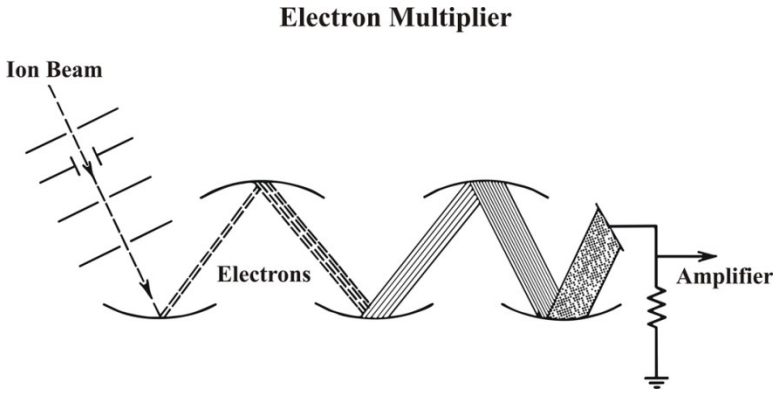


*Fig. 3.11. Scheme of an electron multiplier.The figure is adapted from* [http://www.specmetcrime.com/detectors.htm](http://www.specmetcrime.com/detectors.htm).

**TPD- Temperature Programmed Desorption**

A powerful way of applying mass spectrometry to study desorption processes from the surface, or decomposition reactions due to desorption of previously adsorbed species, is Temperature Programmed Desorption. This technique is also known as TDS (thermal desorption spectroscopy), when the experiments are performed in UHV chambers on well-defined single-crystalline surfaces, as in the case of this work. The working principle is quite simple: the sample, previously exposed to a gas reactant, is linearly heated with a rate $\beta = 3K \cdot s^{-1}$ resulting in a temperature ramp $T = T_0 + \beta t$ (where t= time). The desorbed species and their concentrations are monitored with a quadrupole mass spectrometer (described above).

The analysis of TPD data gives access to the understanding of the energetics and kinetics of adsorption. A typical TPD spectrum is a pressure-temperature curve like the one shown in Fig. 3.12.

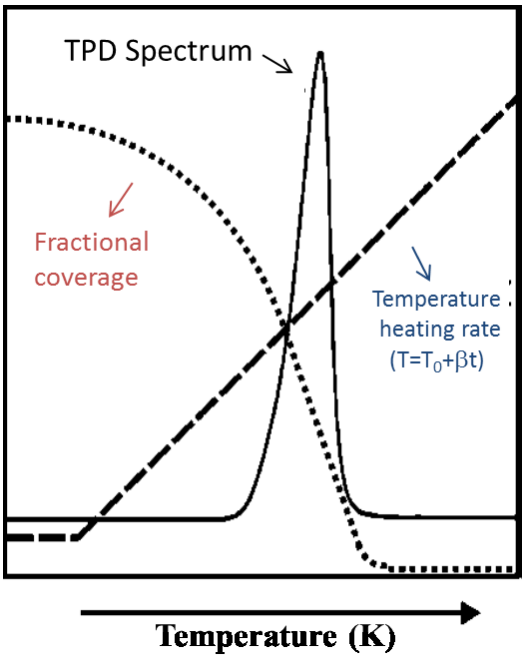


*Fig. 3.12. Schematic temperature programmed desorption spectrum. The figure is adapted from Ref.*[100]

A common desorption profile is characterized by a desorption peak, indicating the maximal concentration of the desorbing species at a certain temperature, according to the Maxwell-Boltzmann distribution. The amount of the desorbing species is proportional to the area of the peak, while their enthalpy of adsorption is related to the peak position (temperature). In general, a TPD spectrum provides information about the bond strength between adsorbate and substrate.

**Fundamentals of thermal desorption spectroscopy.** In a TPD-experiment, the sample is placed in a chamber having volume $V$, which is pumped out at a constant speed $S$, and where a gas is leaked inside at a constant rate $L$. At equilibrium, it is possible to write the steady-state pressure as function of $L$ as follows:

$$L = KSp_{eq} \tag{3.20}$$

with $K$ = proportionally constant ($K = 3.27 \cdot 10^{19}\, molecule^{-1}$, at $P = 1\, torr$ and $T = 295K$). If the sample is heated at constant rate, the gas pressure inside the chamber increases due to the desorbing species. If we assume that no particles re-adsorb on the surface and that adsorption on the chamber walls can be neglected, the mass balance of species leaving and coming into the chamber is given by the adsorption and desorption processes:

$$A\frac{dN}{dt} + L = KSp + KV\frac{dp}{dt} \tag{3.21}$$

where $A$ is the surface area of the adsorbent, $\frac{dN}{dt}$ is the desorption rate and $p$ is the instantaneous pressure inside the chamber. Considering that $\Delta p = p - p_{eq}$, it is possible to rewrite the eq. 3.21 as follows:

$$\frac{d\Delta p}{dt} + \frac{\Delta p}{\tau} = a\frac{dN}{dt} \tag{3.22}$$

with $a = \frac{A}{KV}$ and $\tau = \frac{V}{S}$ = characteristic pumping time. Two experimental scenarios are possible, depending on the pumping speed: i) at small pumping speed ($\tau \to \infty$), the desorption rate is proportional to the first derivative of pressure with time $\left(\frac{dN}{dt} \sim \frac{d\Delta p}{dt}\right)$; ii) at high pumping speed ($\tau \to 0$), as in the most cases of TPD experiments, the desorption rate is proportional to the pressure $\left(\frac{dN}{dt} \sim \Delta p\right)$.

Analysis of desorption signals is based on treating the desorption process as a kinetic phenomenon. In the Polanyi Wigner model, it is assumed that the rate of desorption from a species on a surface may be written in the form:

$$R_{des} = -\frac{d\theta}{dt} = n\theta^n e^{\left(\frac{-E_a^{des}}{RT}\right)} \tag{3.23}$$

where $R = 8.314\, J \cdot K^{-1} \cdot mol^{-1}$ is the universal gas constant, $T$ is the absolute temperature in $K$, θ is the coverage ($0 \leq \theta \leq 1$), ν is the pre-exponential factor (with good approximation $\nu = 10^{13} s^{-1}$), $n$ is the desorption order and $E_a^{des}$ is the desorption

activation energy expressed in $kJ \cdot mol^{-1}$. During TPD measurements, the temperature of the sample surface is linearly increased as $T = T_0 + \beta t$. Therefore, the Eq. 3.23 can be re-written as:

$$-\frac{d\theta}{dT} = \frac{\nu(\theta)}{\beta} e^{\left(\frac{-E_a^{des}(\theta)}{RT}\right)} \theta^{n(\theta)} \tag{3.24}$$

where β is the heating rate measured in $K \cdot s^{-1}$. Initially the temperature increase results in an exponential rise of the desorption rate. At the same time the coverage decreases. The activation energy $E_a^{des}$, the desorption number $n$, and the pre-exponential factor ν should be generally considered as functions of coverage and may, in cases of complex kinetics (e.g., a phase equilibrium on the surface), also depend on the desorption temperature (function of the heating rate). Therefore, the desorption parameters can depend on the TPD experiment conditions.

The coverage θ, it is a function of the gas pressure over the sample and can be considered using the Langmuir adsorption model[129], based on the following assumptions: i) the adsorption is localized, i.e., the adsorbed particles are immobile, ii) the surface substrate is saturated at $\theta = 1ML$, i.e., when all adsorption sites are occupied, iii) there are no interactions between the adsorbed particles. The desorption order, if interpreted as the molecularity of an elementary reaction, allows insight into the nature of the rate-limiting step of the desorption process. In particular, from the molecularity of the desorption process one can often draw conclusions about the state of the adsorbate itself. The TPD spectra of three different adsorbate systems, corresponding to zero-, first-, and second-order kinetics are shown in Fig. 3.13.

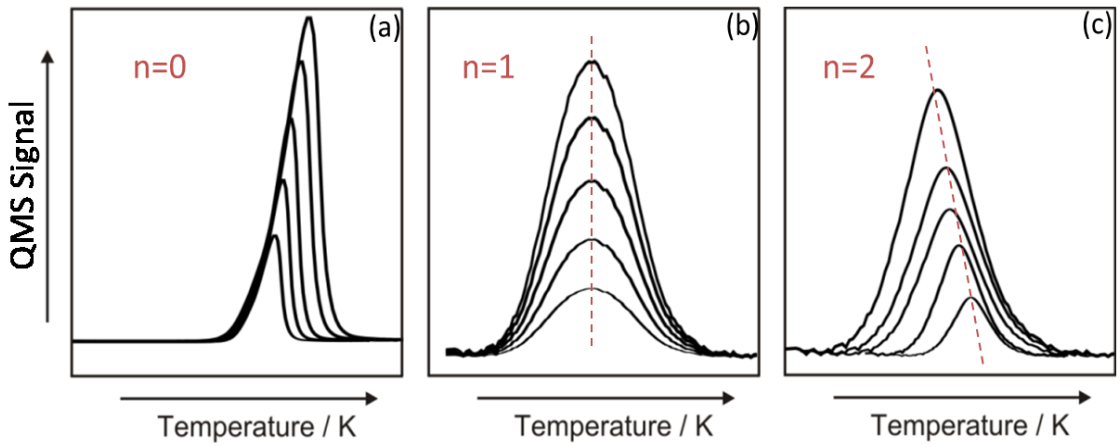

*Fig. 3.13 Series of TPD curves for a zero- (a), first- (b), second-order (c) desorption process. The figure is adapted from Ref.*[100]

In zero-order process (n=0, Fig 3.13a) the desorption rate is coverage independent, i.e., constant at a given temperature. This takes place in case of quasi-equilibrium coexistance of a 2D diluted gas of adatoms and a 2D solid phase. It also occurs at the desorption of a homogeneous multilayer film. In the TPD spectrum, the curves for all initial coverages have a common leading edge and a rapid drop beyond $T_{max}$; the peak temperature $T_{max}$ moves to higher temperature with increasing initial coverage. In first order kinetics (n=1, Fig. 3.13b) the desorption rate is proportional to the coverage. It corresponds to the simplest case when single species desorb directly and indipendently from their sites. The peak has a caracteristic shape with the temperature peak $T_{max}$ remaining constant with increasing coverage. In second order processes (n=2, Fig.3.13c), the desorption rate is proportional to $\theta^2$. It is the case of recombinative desorption, where the desorbing molecule originates from two species residing initially at separate sites. Here, the peak is nearly of symmetric shape and the peak temperature $T_{max}$ moves to lower temperature with increasing coverage.

There are three main methods that have been used to determine the desorption activation energy, the prefactor and the order of desorption in TPD-experiments: *Redhead's analysis*, *leading edge analysis* and *complete analysis*.

**Readhead's Analysis.** This analysis takes its name after P.A. Redhead, who in 1962 derived a simple relation between the desorption activation energy $E_a^{des}$, the peak maximum temperature $T_{max}$ and the desorption order $\nu$ [130]. He assumed that activation parameters are independent from the surface coverage and that the desorption process follows the first order

The maximum in the desorption rate occurs for $-\frac{d^2\theta}{dT^2} = 0$. In the case of $n = 1$, the desorption rate equation can be solved as follows:

$$\frac{E_a^{des}}{RT_{max}^2} = \frac{\nu}{\beta} exp\left(-\frac{E_a^{des}}{RT_{max}}\right) \tag{3.25}$$

Solving the eq. 2.25 for $E_a^{des}$, we obtain:

$$E_a^{des} = RT_{max}\left(ln\frac{\nu T_{max}}{\beta} - ln\frac{E_a^{des}}{RT_{max}}\right) \tag{3.26}$$

The second term in brackets is small relative to the first and is estimated as 3.64. The error introduced through this estimate is less than 1.5% for $10^8 < \frac{\nu}{\beta} < 10^{13}\ K^{-1}$. With this assessment, the relation between $E_a^{des}$ and $T_{max}$ can be written as follows:

$$E_a^{des} = RT_{max}\ (ln\nu T_{max} - ln\beta - 3.64) \tag{3.27}$$

The Redhead method is often employed to extract activation energies from a single peak desorption spectrum in processes characterized by first order desorption.

**Leading Edge Analysis.** This analysis was first introduced in 1984 by Habenschaden and Küppers[131]. According to them, this method is based on the assumption that in small temperature range the variation of *v* can be neglected and $\theta$ is close to the initial coverage. The leading edge of the TPD curve fits the Polanyi-Wigner equation (see 3.25). The desorption rate is proportional to the intensity of the TPD trace. Desorption is an activated process that obeys the Arrhenius equation and, therefore, we can write:

$$R_{des} = A\nu\theta^n e^{\left(-\frac{E_a^{des}}{RT}\right)} \tag{3.28}$$

where A is a proportionally constant. Taking logarithms of both sides of this equations leads to:

$$lnR_{des} = lnA + lnv + nln\theta - \frac{E_a^{des}}{RT} \qquad (3.29)$$

Plotting $lnR_{des}$ versus $\frac{1}{T}$, an Arrhenius plot with the slope $E_a^{des}$ is obteined. It is also possible to determine the desorption order. In TPD experiments it is not possible to measure the absolute coverage, however integrating the area under the TPD peaks gives a relative coverage $\theta_{rel}$. The eq. 3.29 can be rewritten considering $\theta = \theta_{rel}$:

$$lnR_{des} = lnA + lnv + nln\theta_{rel} - \frac{E_a^{des}}{RT} \qquad (3.30)$$

Plotting $lnR_{des}$ versus $ln\theta_{rel}$ at a fixed temperature, the order of desorption will be given by the gradient of this plot.

**Complete Analysis.** This approach was introduced by King in1975[132]. The Fig. 3.14 shows the procedure.

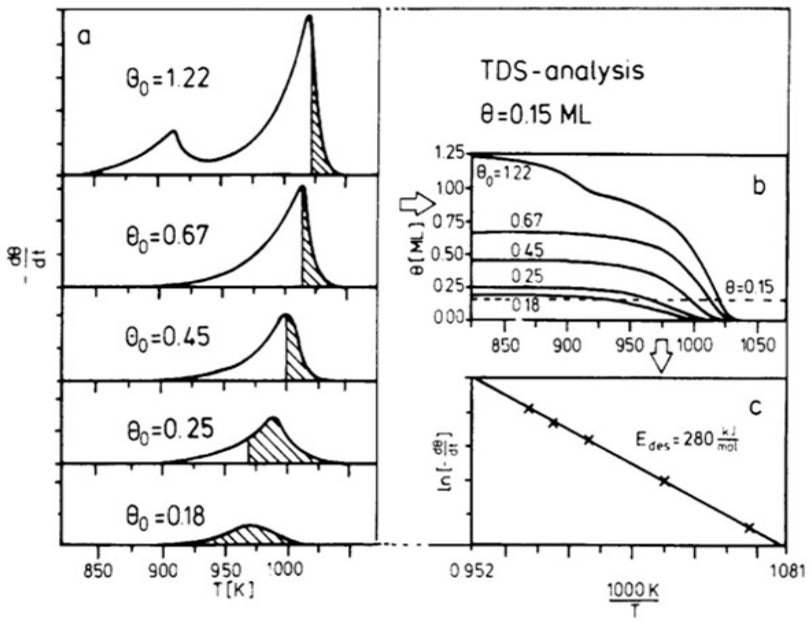


*Fig. 3.14 Complete analysis of TPD data. (a) The spectra are integrated to etermine points on the spectra corresponding to a fixed coverage. (b) A pair of ($R_{des}$, T) values for every desorption trace are given, from which an Arrhenius plot is made. (c) The slope yields the activation energy. The figure is taken from Ref.[40]*

A coverage is chosen (e.g. 0.15 ML); the points corresponding to $\theta = 0.15ML$ on all TPD curves are found. This gives a pair of ($R_{des}$ and $T$) values from every curve with initial coverage larger than 0.15 ML. An Arrhenius plot of all $lnR_{des}$ versus $\frac{1}{T}$ values for this particular coverage yields $E_a^{des}$. The prefactor follows from the intercept $nln\theta + nlnv(\theta)$, when the order of desorption is known. For coverage above 0.1 ML the term $nln\theta$ is much smaller than $nlnv(\theta)$, and can be ignored. The pre-exponential factor can be regarded as representing the frequency of attempts of the adsorbed particle to escape the chemisorptive potential. The values determined vary by at least four orders of magnitude, from $10^{12}$ to $10^{16}$ $s^{-1}$.

### 3.3.4 Low Energy Electron Diffraction (LEED)

LEED is a very useful technique to determine both the surface structure and symmetry of a given crystal and of adsorbate-superstructures. The base principle of this technique is the electron diffraction. Upon bombardment of crystalline solids with electrons accelerated by a low voltage (typically below 300 *V*) to a constant velocity, diffracted electrons spots on a fluorescent screen are observed. Due to the different interatomic and interplanar distances in crystalline materials, the electron diffraction patterns are characteristic for a specific crystallographic structure.

As predicted by De Broglie in 1921, every moving particle has a wave-like nature and, therefore, electrons can undergo diffractions or interference. Combining the De Broglie's equation for the electron wavelength, the momentum $p$ and the dependence of the wavelength from the kinetic energy, a relation between the beam voltage and λ is established:

$$\lambda = \frac{h}{p} = \frac{h}{\sqrt{2mE_k}} = \frac{h}{\sqrt{2meV}} \tag{3.31}$$

where λ is the wavelength, $m = 9.11 \cdot 10^{-31} kg$ is the electron mass, $h = 6.626 \cdot 10^{-34} J \cdot s$ is the Planck constant, $E_k$ is the kinetic energy of the electron, $e = 1.6022 \cdot 10^{-19} C$ is the electron charge and $V$ is the beam energy.

As shown in the universal curve[133] in Fig. 3.15, the inelastic mean free path (IMFP) of electrons in a solid strongly depends on the beam energy rather than on the chemical identity of the solid. A typical LEED voltage is in the range between $20V$ and $200V$ which, according to the Eq. (3.31), corresponds to $\lambda < 3$Å. This is in the order of interatomic distances in a crystal lattice and is small enough to probe only the first 3-4 atomic layers: electrons scattered from deeper layers play no role in the observation of interference patterns on a luminescent screen opposite to the sample.

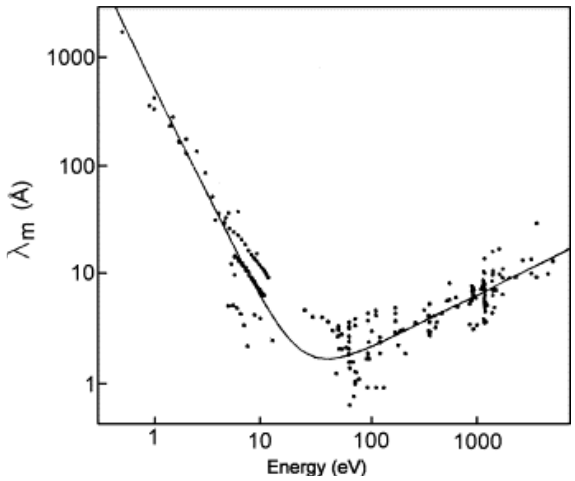


*Fig. 3.15 Universal curve of electron mean free path in solid matter. The figure is adapted from Ref. [41].*

The Fig. 3.16 shows how LEED patterns can be created using a geometric construction known as the Ewald sphere. The real space atomic positions in a crystal lattice are given by a vector $\vec{F}$. Another vector $\vec{G}$ is defined as the reciprocal lattice. $\vec{F}$ and $\vec{G}$ are related to each other as follows:

$$e^{i\vec{F}\vec{G}} = 1 \tag{3.32}$$

Note that the component of $\vec{F}$ perpendicular to the surface is inherently zero. Hence, the corresponding component of $\vec{G}$ has an infinite length, as indicated by the dashed parallel lines in Figure 3.16. Diffraction spots are observed, where this vector intersects with the Ewald sphere, which is explained in the following. The incident electron beam has a wavevector, $\overrightarrow{k_0}$,

$$\left|\overrightarrow{k_0}\right| = \frac{2\pi}{\lambda} \tag{3.33}$$

which is scattered from the sample. The scattered wavevectors $\overrightarrow{k_{ij}}$ $(i, j \in \mathbb{Z})$, have the same length as $\overrightarrow{k_0}$. Both $\overrightarrow{k_0}$ and $\overrightarrow{k_{ij}}$ are radii of the Ewald sphere. The difference vector between $\overrightarrow{k_0}$ and $\overrightarrow{k_{ij}}$, $\Delta\vec{k}$, is called scattering vector. Scattered electrons undergo constructive diffraction if the path difference between electrons coming from different atoms is equal to a multiple number of the wavelength (Bragg condition for constructive interference):

$$2dsin\theta = n\lambda \tag{3.34}$$

where $d$ is the distance between two adjacent lattice layers, θ is the angle between the incident beam and the surface, and $n$ is an integer number. Bragg's/ or the Bragg condition is satisfied where the Ewald sphere intersects with the reciprocal lattice:

$$\Delta\vec{k} = \vec{G} \tag{3.35}$$

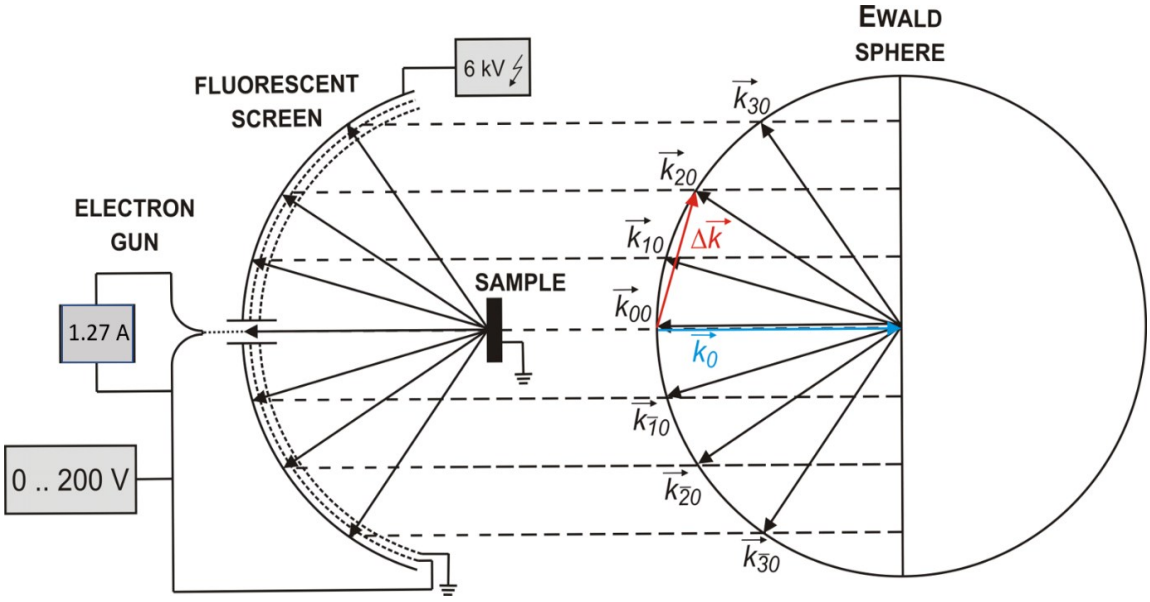


*Fig. 3.16 Basic principles of LEED and Ewald sphere.*
*The figure is adapted fromRef*[134].

**LEED Setup.** The experimental setup of LEED is depicted in the left part of Figure 3.16. The standard LEED apparatus comprises a hemispherical fluorescent screen and an electron gun aligned along the central axis of the screen. A current is applied to a filament made of low work function metals ($LaB_6$, W or Ir) to accelerate electrons towards the sample. To avoid deflection of the electron beam by the residual magnetic fields, the optics are covered by an anti-magnetic shield, which is made from μ-metal. The typical value for the beam voltage is 70 $V$ throughout this work, because then the screen shows the equivalent of the first Brillouin zone, which is the reciprocal of the real space lattice unit cell. The beam is focused by electrostatic lenses and reflected from the sample toward a luminescent screen. Before they are registered at the screen, they pass a repelling electrode, which is set to the beam acceleration potential ($V$ in equation 3.31), in order to deflect background electrons. Beyond this stage, the electrons are accelerated by a potential of typically 6 kV to produce a pattern of sufficient brightness.

## 3.4 Experimental Setup

All the experiments described in this work (Chapter 5, 6, and 7) were performed at the Fritz-Haber-Institut der Max-Planck-Gesellschaft in Berlin. Fig. 3.17 shows the ultra-high vacuum molecular beam/IRAS apparatus used (the details of the chamber can be found elsewhere[108]).

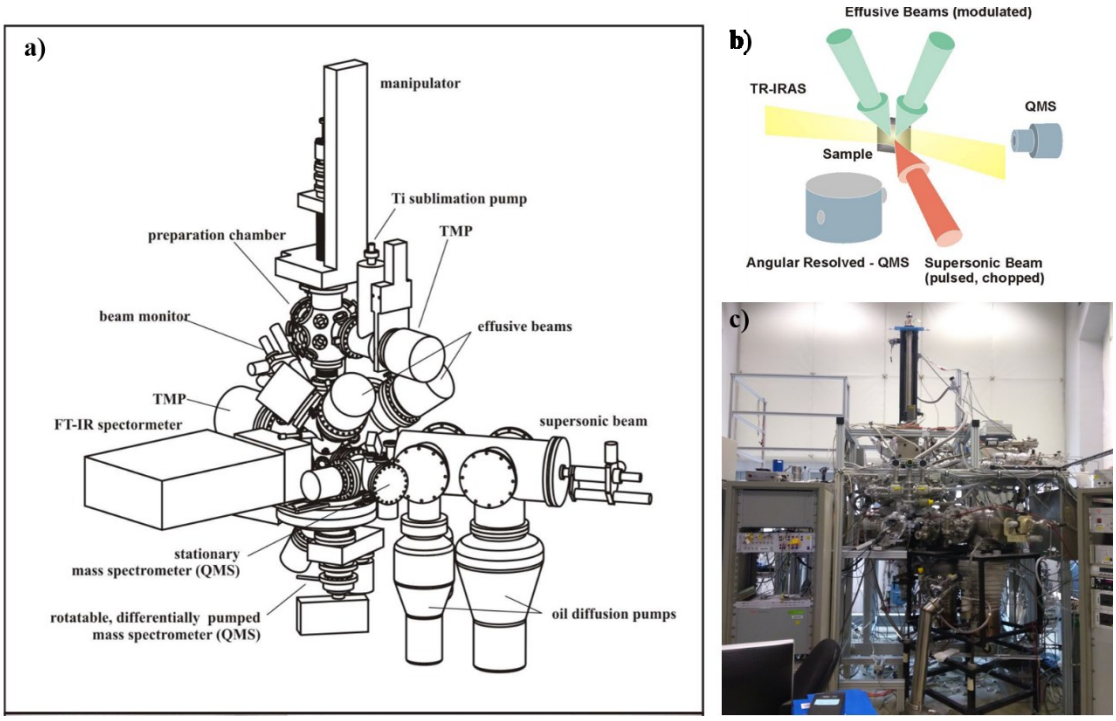


*Fig. 3.17. A schematic illustration (adapted from Ref.[30]) of the molecular beam/IRAS setup (a). The cartoon in (b) illustrates the chamber on the bottom of the setup, containing the two effusive beams, the supersonic beam, the infrared spectrometer and a mass spectrometer. A picture of the entire system is showed in (c).*

A vacuum Fourier-Transform Infrared (FT-IR) spectrometer (Bruker IFS 66v/S) with a spectral resolution of 2 $cm^{-1}$ was used with a mid-infrared (MIR) polarizer to select the p-component of the IR light.

The TPD experiments were performed with a commercial QMS (Hiden 301), using a heating rate in each run of 3 K/s.

The reactants used for the adsorption/desorption experiments were supplied via an effusive doubly differentially pumped molecular beam to exactly control the exposure. The acquisition of the IRA spectra was performed at the dosing temperature.

In particular, the following reactants were used:

- Water (Deuterium Oxide "100", min. 99.96% D, Sigma-Aldrich; Deuterium Oxide labelled with $^{18}O$, 95% $^{18}O$, 99% D, Sigma-Aldrich; ultrapure water, deionized and distilled $H_2O$);
- Carbon dioxide ($CO_2$, Linde; Carbon-$^{13}C$ Dioxide, min 99 atom % $^{13}C$, Campro Scientific; Carbon Dioxide-$^{18}O_2$, 97 atom % $^{18}O$, Campro Scientific);
- Carbon monoxide (CO, Linde);
- $O^{18}$-labelled magnetite ($Fe_3O^{18}{}_4(111)$) was prepared using $O^{18}$-gas, purity of 97 %, from Campro Scientific. The water was adsorbed on the surface in the temperature range between 120 and 350 K, and the acquisition of the IRA spectra was performed at the dosing temperature.

# 4. CO Adsorption on $Fe_3O_4$(111): Surface Termination

## 4.1 Introduction

Iron oxides have significant relevance in many technological applications, being for example an important active phase in iron-based catalysts for Fischer-Tropsch processes, water-gas shift reaction, etc.[135,136]. It is of high interest to understand the oxide surface structure and adsorption studies of probe molecules may be helpful in this sense. A variety of sites may exist on a metal oxide surface, i.e. coordinatively unsaturated cations, surface anions, and cation-anion pairs. Thus, several adsorption modes may exist. In the specific case of reducible oxides such as hematite and magnetite, choosing the right probe molecule for the adsorption study might is therefore critical. The chemistry of molecules like water and/or hydrocarbons is rather complex and processes such as temperature-dependent decomposition of the adsorbed molecule may occur[22]. With the use of carbon dioxide as probe molecule, it is possible to avoid these issues because it does not decompose on the surface and also its adsorption properties can be directly related with the surface structure of the oxide. CO adsorption on magnetite, has been extensively studied both theoretically and experimentally. The first TPD study was performed in the early 80s, when Udovic and Dumesic reported that CO does not chemisorb on magnetite at low temperature (150 K), but only weakly binds, giving rise to carbonyl species on the surface with a heat of adsorption of 46 kJ/mol[83]. These results are in disagreement with later studies performed by Watanabe and Kadowaki who showed that magnetite is indeed very reactive towards CO[137]. Experiments on the water-gas shift reaction performed by Rethwisch and Dumesic[138] suggested that CO can be oxidized by the adsorbed oxygen atom on the magnetite surface. Later on, Tinkle and Dumesic[139] proposed that the adsorption of CO occurs on coordinatively unsaturated cations sites, whereas the anion sites are reduced by the carbon monoxide. These results were questioned by Lemire et al. who studied the CO adsorption on thin $Fe_3O_4$(111) films by using temperature-programmed-desorption and found that the surface does not suffer from reduction by carbon monoxide[22]. Huang et al.[136], provided a density functional theoretical investigation on the CO adsorption on $Fe_3O_4$(111), focusing on the difference between $Fe_{oct2}$- and $Fe_{tet1}$- terminated surfaces. They predicted a more favored adsorption for the CO molecule on $Fe_{oct2}$- terminated magnetite. On both surfaces the on-top

configuration seems to be the preferred. The presented literature overview displays some discrepancies on the way how magnetite reacts towards CO, presumably related with the difference of the experimental conditions and possibly film preparation.

The latter studies[136,22] are an example of using CO adsorption as a way to characterize and clarify the surface termination of $Fe_3O_4$(111) surfaces. Indeed, although the (111) surface of $Fe_3O_4$ (magnetite) has been investigated for more than twenty years, substantial controversy remains in the literature regarding the surface termination[33,40]. It seems like the main controversy regarding the $Fe_3O_4$(111) surface termination originates from LEED and DFT studies, suggesting $Fe_{tet1}$-terminated surface as the most stable, and adsorption studies (in particular of CO and water) rationalized in terms of $Fe_{oct2}$ terminated surface in the outermost layer[140]. In order to give a unified picture on the CO adsorption on magnetite surfaces and also shed light on the question of surface termination of $Fe_3O_4$(111), CO adsorption studies on (111) and (001) oriented thin films, using *in-situ* infrared reflection absorption spectroscopy and temperature programmed desorption experiments, were performed in this work. The obtained experimental results were then rationalized on the basis of theoretical calculations. The outcome of this combined experimental and theoretical approach (the details will follow in this chapter) allowed to determine that the $Fe_3O_4$(111) surface is terminated by $^1/_4$ monolayer of tetrahedrally coordinated $Fe^{3+}$ ions on top of a close-packed oxygen layer, as previously determined by low energy electron diffraction[14].

## 4.2 Surface Preparation

The preparation of the $Fe_3O_4$(111) film is critical to understand the CO adsorption results and link them with the surface termination. Prior to use, the Pt(111) substrate was cleaned by repeated cycles of $Ar^+$ ion bombardment at room temperature, annealed at 1200 K and oxidized in $1 \cdot 10^{-6}$ mbar $O_2$ at 1000 K. In the first step of the film growth, an ultrathin FeO(111) film was prepared[33] on a Pt(111) substrate, by deposition of 1 ML Fe at room temperature and then annealing at high temperature (1000 K) in $5 \cdot 10^{-7}$ mbar $O_2$ atmosphere. The evaporation rate of Fe (~1 Å/min) was calibrated by a quartz-crystal microbalance (QCM, Sigma instruments). The quality of the FeO layer is easy to be checked by LEED, but also CO titration of Pt was used. After that, $Fe_3O_4$(111) is grown by 3-5 cycle of Fe deposition onto the Pt substrate

(kept at room temperature), followed by an oxidation step at 900 K for 5 minutes. In the final steps, the oxidation procedure is performed at slightly higher temperature (950-1020 K). The oxygen atmosphere is kept in the chamber also during the cooling process and pumped down at 500 K. The above described film preparation allowed us to grow ~50 Å thick $Fe_3O_4$(111) films.

## 4.3 Results and Discussion

The adsorption of CO at different exposures on well-ordered $Fe_3O_4$(111) films was performed dosing carbon monoxide at low temperature (100 K). Fig.4.1a shows the infrared spectra recorded as function of coverage upon CO adsorption on magnetite, until saturation is reached. At saturation, it is possible to see that the CO chemisorbs on $Fe_3O_4$(111) giving rise of three main vibrational features, indicated in the figure as $\alpha$, $\beta$, and $\gamma$. As the figure clearly shows, these peaks are coverage dependent and their trend will be discussed below.

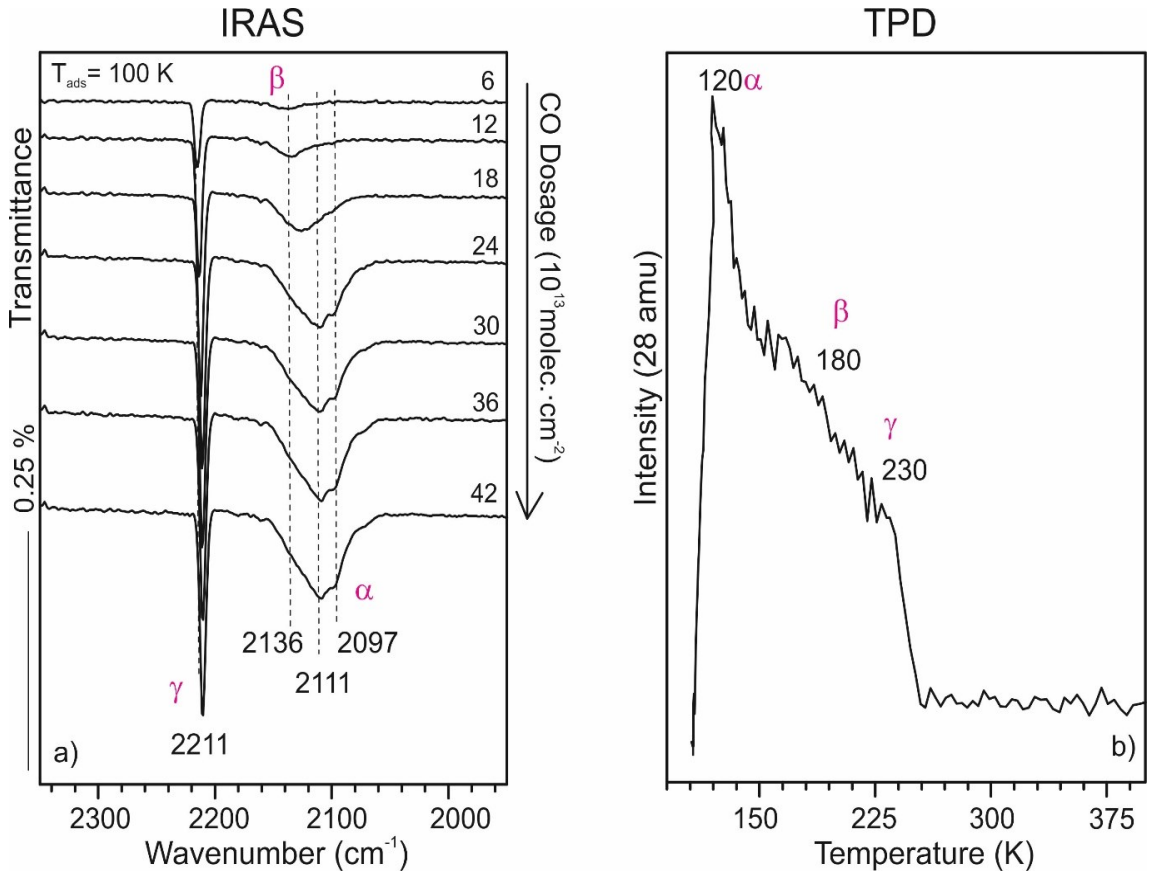


*Fig. 4.1. a) Infrared spectra of CO adsorbed at low temperature (100 K) on $Fe_3O_4$(111) surface as function of coverage. b) TPD recorded after CO adsorption on $Fe_3O_4$(111) surface at 100 K.*

When a small amount of CO is adsorbed on $Fe_3O_4$(111) at low temperature, the IRA-spectrum shows a very sharp peak centered at 2211 $cm^{-1}$ and a very broad and tiny feature at around 2136 $cm^{-1}$, referred in the figure as γ and β respectively. As the CO coverage increases, both peaks gain intensity and undergo red-shift. However, while in the case of the γ peak the shift is very small and most likely due to a coverage effect (see Chapter 3, Section 3.3.2 for more details), the β peak seems to correlate to a broader range of frequency which go from 2136 $cm^{-1}$ to 2111 $cm^{-1}$ (~25 $cm^{-1}$ separation between the two extremes). In the high coverage regime, a new feature centered at around 2097 $cm^{-1}$ appears, which is labelled as α in the figure. The IRA adsorption features correlates well with the desorption peaks obtained when a temperature programmed desorption experiment is run on the same sample, after CO saturation is reached on the surface (~$40 \cdot 10^{13}$ CO molec.·$cm^{-2}$). The latter experiment is shown in

Fig.4.2. According to the IRA-experiment, the TPD spectrum shows three main desorption features at around 120 K, 180 K, and 230 K. It must be mentioned that the experiment shown in Fig.4.1b may suffer from low resolution because the mass spectrometer used (described in Section 3.4, Chapter 3), is not equipped with differential pumping stage. However, the results are in very good agreement with what was observed in an earlier study done by Lemire et al.[22], and also in one of our recent works[140] where the same experiment was repeated using a setup especially designed for TPD experiments. According to them[22,140], the three desorption peaks in Fig. 4.1a can be assigned to the IRA features as follows. The sharp peak at 2211 $cm^{-1}$, indicated as γ, desorbs around 230 K; the β peak, which is consistent with a wider range of frequencies, shows a broad desorption feature centered at around 180 K; finally, the α correlates with the sharp desorption peak at 120 K.

As already mentioned, a very similar investigation was performed in 2004 by Lemire et al.[22] The study presented in this work shows some similarities with the previous one in the vibrational as well as in the desorption spectra, although the peak assignment and the general interpretation of the experimental data differs substantially. In particular, in the earlier study the infrared peak that here is assigned to α, was attributed to a very weak band showing frequency at 2141 $cm^{-1}$, which is a value very close to the CO vibration in the gas phase (2143 $cm^{-1}$). However, in the experiments done for this work, no tiny 2141 $cm^{-1}$ peak has been observed. The reason for that might be the surface preparation. For this purpose, several different samples were prepared during this work, following the procedure illustrated in the Section 4.2 of this Chapter and all of them showed reproducible IRA and TPD spectra. It was, though, noted that the intensity of the β and γ features is very sensitive to the surface preparation and varies randomly from sample to sample, even though no differences in the LEED pattern are observed.

Fig. 4.2 shows an interesting comparison of the TPD spectra obtained after CO adsorption on $Fe_3O_4$(111) and $F_3O_4$(100). Before drawing any conclusions on the spectra showed in the figure, it must be pointed out that these spectra were performed in a different chamber equipped with differential pumping stages and, therefore, the peak resolution is definitely higher. Despite that, it is clear that both sets of

experiments are in good agreement with each other, and therefore the results from the two chambers can be correlated.

As depicted in Fig. 4.2, while from the (111) surface CO desorbs giving rise to the three desorption features discussed above, on the (100) facet it is possible to observe only the α state, whereas the β and γ features are not present. Unlike the $Fe_3O_4$(111), the $F_3O_4$(100) surface structure is known with a high degree of precision and both thin films and single crystals, expose an almost defect-free uniform and homogeneous surface[40,33,21]. According to this, the fact that the CO TPD in the case of the (100) does not show the β and γ desorption states might mean that are indeed the surface imperfections the responsible for these two features in $Fe_3O_4$(111).

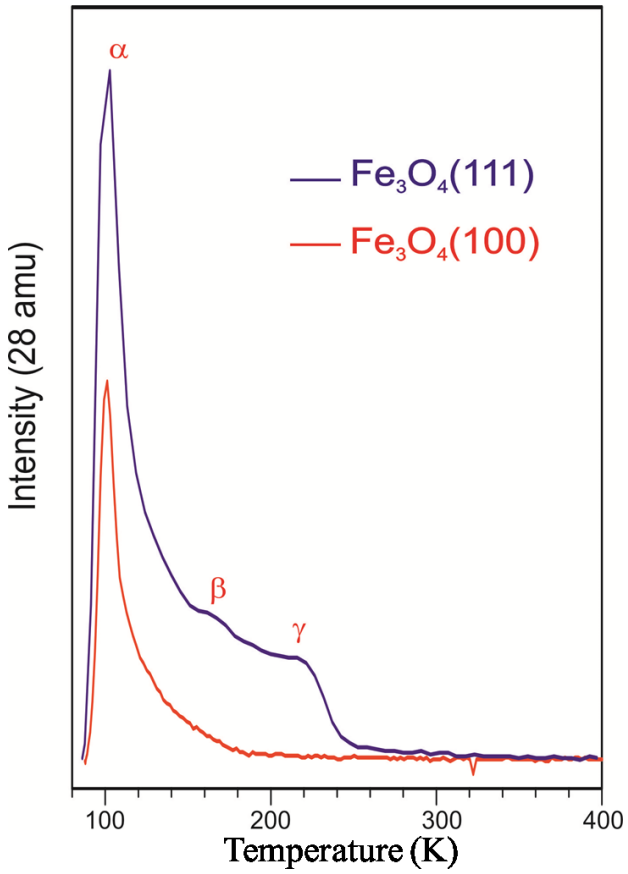


*Fig. 4.2. TPD of CO adsorbed at 90 K on $Fe_3O_4$(111) -blue spectrum- and on $Fe_3O_4$(100) -red spectrum- surfaces. This TPD experiment was performed by Eman Zaki at the Fritz-Haber-Institut der Max-Planck-Gesellschaft in Berlin.*

Another experimental evidence supporting this hypothesis is given by the CO coverage estimation on our $Fe_3O_4(111)$ film. A quantification can be done comparing the desorption spectra for the β and γ states with the CO TPD for the bare Pt(111) prior to film growth. This experiment is shown in Fig. 4.3.

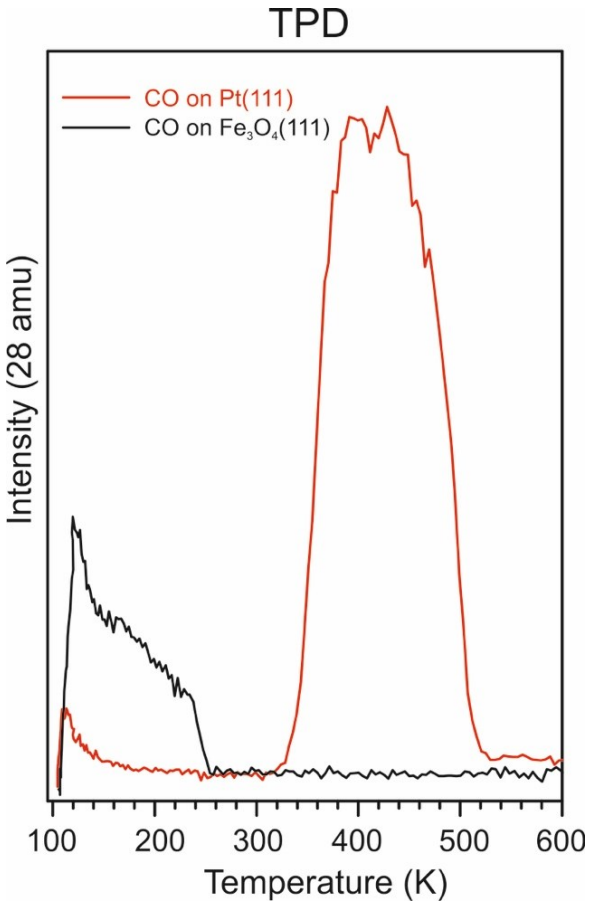


*Fig. 4.3. TPD spectra of CO adsorbed on $Fe_3O_4(111)$ – black line - and on bare Pt(111) – red line. It must be noted that the envelope of the TPD profile showed in this figure is quite consistent with the one showed in Fig. 4.2 which was performed in a different UHV setup. The reproducibility and consistency of these data in two different systems allows to safely cross-correlate them.*

The CO adsorption on Pt(111) has been widely investigated in the past[141,142], and it is well known that CO exhibits a c(4x2) structure at CO density of $7.5 \cdot 10^{14}$ molec.$\cdot cm^{-2}$. Using this value for the calibration, defining one monolayer (ML) as 1ML = $3.2 \cdot 10^{14}$ molecules $\cdot$ $cm^{-2}$ (corresponding to one molecule per $Fe_3O_4(111)$ surface unit cell), the CO coverage on magnetite corresponding to the integral area of the β and γ desorption

peaks is consistent with ~0.25 ML. The latter value is very small to be associated to adsorption on a regular surface and it seems more likely to account for CO adsorbed on defects sites.

In order to use the outcome from the CO adsorption/desorption experiments towards understanding the surface termination of our $Fe_3O_4$(111) film, a density functional theory study was required. The DFT calculations were performed by Xiaoke Li and Dr. Joachim Paier (Humboldt University, Berlin) and the details of this study can be found in[140] and references therein. Here, only the relevant points will be discussed in order to reach a unified picture between experiments and theory.

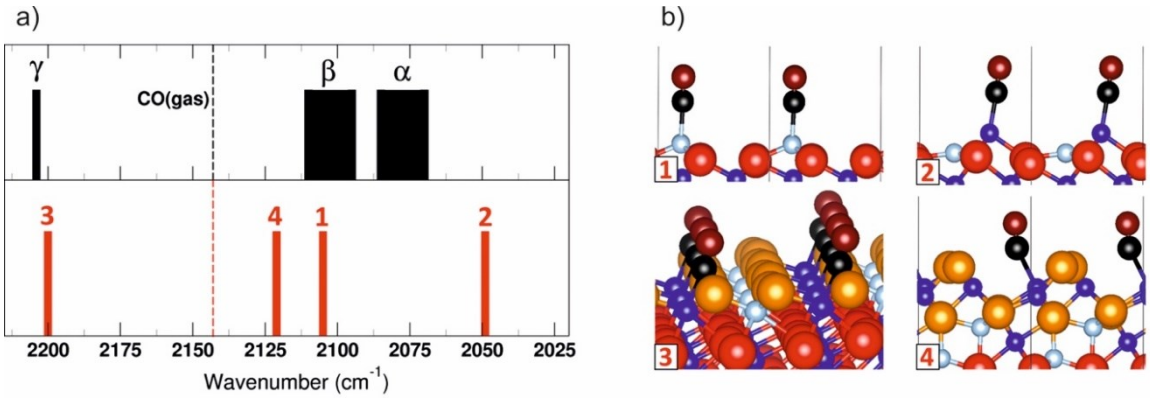


*Fig. 4.4. Comparison between observed (black) and calculated (red) vibrational frequencies of CO adsorbed on $Fe_3O_4$(111) (a). Calculated structures for CO adsorbed on a regular $Fe_{tet1}$, on regular $Fe_{oct2}$, and on step edges of type A and B displayed by structure 1, 2, 3 and 4 respectively (b). Color code: the $Fe_{oct2}$ and $Fe_{tet1}$ ions are dark and light blue, respectively; the lattice oxygen is red; the oxygen in O-ad-layers (structures 3 and 4) is orange; the carbon is black; the oxygen in CO is dark red.*

Four structures have been calculated as a result of the CO adsorption on regular tetrahedrally terminated surface ($Fe_{tet1}$), on regular octahedrally terminated surface ($Fe_{oct2}$) and on two different types of step edges (A and B types[22,143]). These structures and the corresponding calculated vibrational frequencies compared with the experimentally observed one are shown in Fig. 4.4. The calculation for CO adsorbed on an octahedrally terminated surface (structure 2) shows a CO-stretching at 2049 $cm^{-1}$. This value is red-shifted compared to the CO stretching in the gas phase and this is

essentially due to the back-donation from metal d-bands to the unoccupied $2\pi^*$ molecular orbital of CO. Since the $5\sigma$ orbital is only weakly bonding, but the $2\pi^*$ orbital has strong antibonding character, the population of the $2\pi^*$-MO weakens the CO internal bond, which lead to the red shift in the frequency[126,144]. Form the thermodynamic point of view, CO strongly adsorbs on $Fe_{oct2}$ with adsorption energy of ~ -103 kJ/mol. Using this energy value in the classical Redhead analysis[130] to calculate the corresponding desorption temperature, a value of $T_{des}$= 400 K is obtained. As Fig. 4.2 shows, this value is quite out of the range of the desorption temperatures that we have measured experimentally with TPD. According to this calculation and together with the experimental evidences an octahedrally terminated surface can be ruled out. The calculated structure indicated as structure 3 represents a CO on a type A-defective surface (with an oxygen layer on top of the $Fe_{oct2}$), having a stretching frequency of 2200 $cm^{-1}$. This feature, which is blue-shifted in comparison with the free CO stretching frequency, fits very well the observed $\gamma$ peak (observed experimentally at 2211 $cm^{-1}$). The blue-shift can be explained by the known "wall effect"[145]. When CO is adsorbed on an ionic surface and vibrates without moving its center of mass from the surface, the carbon lone pair gets closer to the surface thus increasing the Pauli repulsion and the potential well in this region. This results in a blue shift of the vibrational frequency. The last two structures, 1 and 4, represent CO adsorbed on a regular $Fe_{tet1}$ surface and on a Fe-rich step edge (B-type) respectively. The corresponding vibrational frequencies for these two models are 2105 $cm^{-1}$ and 2120 $cm^{-1}$ and both fall in the experimentally observed spectral region between 2136 and 2090 $cm^{-1}$ which exhibits more complicated features. The assignment is more complex but based on the relative peak positions and on what we have learned earlier from the TPD studies, it is reasonable to correlate the $\beta$ peak with the CO adsorbed on a B-type defective surface. Thus the $\alpha$ peak, present only at low temperatures, is assigned to CO adsorbed on regular tetrahedrally terminated surface ($Fe_{tet1}$).

## 4.4 Conclusions

Carbon monoxide can be used as probe molecule to study the surface structure of iron oxides because it does not undergo decomposition and also its adsorption properties can be directly correlated with the adsorption sites on the surface itself. A combination of experimental techniques such as IRAS and TPD as well as theoretical calculations, allows the characterization of the $Fe_3O_4(111)$ surface leading to an unified picture. By following the preparation procedure of the iron oxide described in Section 4.2, it is possible to obtain a well-ordered film terminated by a 1/4 monolayer of $Fe_{tet1}$ ions over close-packed oxygen layer. This study highlights the important role of surface preparation and exposure conditions as well as defects. Having a clearer idea about the surface termination of $Fe_3O_4(111)$ is the first step towards understanding the initial stage of water adsorption on magnetite. There is indeed certain controversy in the literature on the interaction between water and $Fe_3O_4(111)$ which can be substantially attributed to the difficulties to prepare well-defined uniform surfaces. A detailed study on the adsorption of water on magnetite, rationalized in terms of tetrahedrally terminated surface will be the subject of the next chapter.

# 5. Water Adsorption on CO Adsorption on $Fe_3O_4$(111)

## 5.1 Introduction

The all-presence of water and oxide surfaces in nature and their extensive application in heterogeneous catalysis, photo- and electro-chemistry, renewable energy production and storage, etc., make them a subject of study of enormous scientific and practical importance. Iron oxide is the most abundant class of oxides on earth and, therefore, the understanding of the interaction between water and iron oxide is interesting and essential. Iron is a multivalent element which can form oxides having different stoichiometry and surface terminations[33,22,40]. Hence, by choosing the appropriate preparation conditions, it is possible to finely tune the physical and chemical properties of the final material. It is possible to find in the literature a considerable number of studies on the interaction of water with different metal oxides. Indeed, adsorption studies have been performed at atomistic level on model surfaces such as $TiO_2$[4–150], MgO[151], ZnO[152,153], $Fe_3O_4$[65,67,68,70,71], $Fe_2O_3$[154], $RuO_2$[155], CaO[156], $SrTiO_3$[157], and others. The latter studies, mainly employing imaging techniques and theory, largely contributed towards the understanding of the water interactions with oxides and some systematics in the water adsorption process as a function of coverage are observed. However, a detailed atomistic mechanism of this interaction on transition metal oxides is still lacking and, where present, controversial. Indeed, as already mentioned in Chapter 2, the comprehension of the initial stage of water adsorption and dissociation remains an open question. In the case of water adsorption on $Fe_3O_4$(111), the main disagreement can be found between a general accepted model – also known as "classical model"- proposing water dissociation on a tetrahedrally terminated surface[67,68,70], and a more recent study invoking an octahedrally terminated surface to explain the formation of a water complex from the onset upon adsorption on the surfaces[51]. Hence, in the first study the water molecule dissociates on the surface giving rise of two hydroxo-species, $O_wH$-Fe and $O_sH$, where $O_w$ and $O_s$ indicate oxygen atoms in water and on the oxide surface, respectively. In the second study, the water spontaneously assembles in a complex formed by dissociated and non-dissociated molecules, known as "half-dissociated dimer". The main origin of this controversy is related to the difficulties of preparing well-defined, uniform and clean

surfaces. Also, surface imperfections are hard to quantify using LEED, conventionally employed to evaluate the quality of the prepared film. Our recent work, explained in detail in Chapter 4, allowed us to prepare a well-characterized $Fe_3O_4(111)$ with a tetrahedrally terminated surface, eliminating such discrepancy. In particular, it looks like the annealing step in ultra-high vacuum at high temperature (above 750 K) during the surface preparation plays a crucial role for the formation of a uniform $Fe_{tet1}$-terminated surface.

In this chapter we present the initial stage of water adsorption on a well-defined $Fe_3O_4(111)$ surface – prepared using the knowledge learned in Chapter 4. In particular, combined IRAS and TPD data revealed that water readily dissociates on the surface to form two hydroxyl species. The first, $O_wD$, contains an oxygen atom from the water itself and sits on top of a Fe cation; the second, $O_sD$, derives from a D atom from the water and an oxygen from the surface lattice. These species act as anchors for molecular water adsorption ultimately giving rise to a long-range ordered structure. The results were rationalized by DFT calculations in the framework of cooperative formation of the hydrogen bonding network.

## 5.2 Low Coverage Regime

The study of the water adsorption on magnetite has been performed adsorbing $D_2O$ on the surface at several temperatures and recording the IRA spectra as function of coverage. Fig. 5.1 shows the water behavior at 300 K, corresponding to a very low coverage.

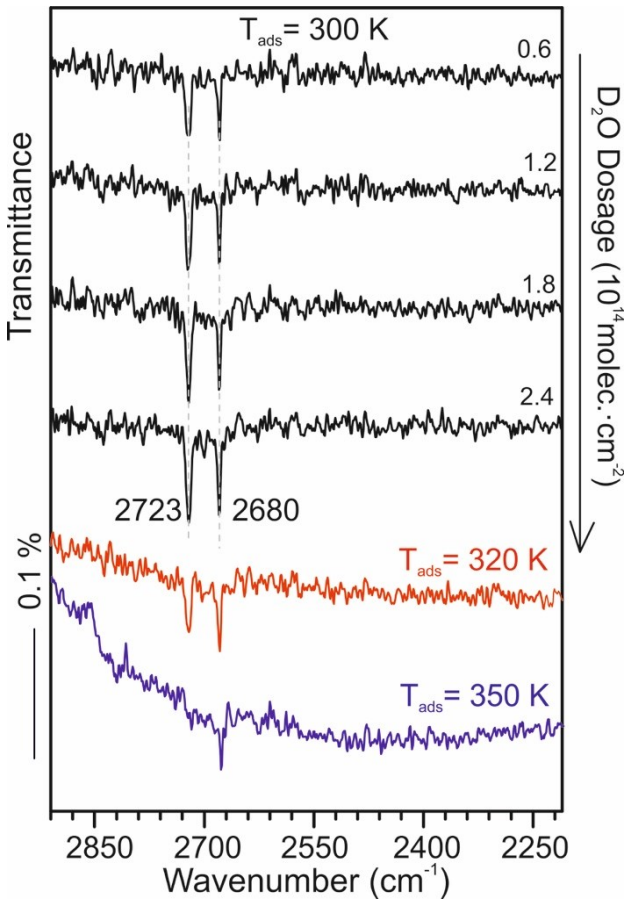


*Fig.5.1. IRA spectra of $D_2O$ adsorbed on $Fe_3O_4(111)$ as function of coverage (black). Each water pulse corresponds to a dose of $6 \cdot 10^{13}$ molec.·cm$^{-2}$. The red and the blue spectra correspond to $D_2O$ adsorbed on $Fe_3O_4(111)$ at 320 K and 350 K respectively (dosage = $2.4 \cdot 10^{14}$ molecules·cm$^{-2}$).*

At 300 K, $D_2O$ adsorbs on the surface giving rise of two sharp peaks, at 2723 cm$^{-1}$ and 2680 cm$^{-1}$ respectively. These features grow together and saturate almost immediately. Although the peaks appear together, adsorption experiments performed at higher temperature indicate that their behavior is independent. Hence, the lower frequency peak remains up to temperatures as high as 350 K, while the 2723 cm$^{-1}$ peak disappears above 320 K. Based on this observation, we can tentatively assign the 2680 cm$^{-1}$ peak

to water adsorbed on defects sites. Instead, the peak at 2723 $cm^{-1}$ falls in the range of the frequencies calculated for an OD group on top of a Fe cation[74]. More information can be obtained by looking at higher coverages. Fig.5.2a shows the case of $D_2O$ adsorption on magnetite at 250 K. It is clear that, even if the spectrum after the first $D_2O$ pulse looks similar as for the adsorption at 300 K, at higher water dosage the picture changes. It seems that the higher frequency peak exhibits a red shift whereas a blue-shift is observed for the lower frequency peak. Also, a new broad band appears at 2569 $cm^{-1}$, which falls in the frequency range for hydrogen bonded species.

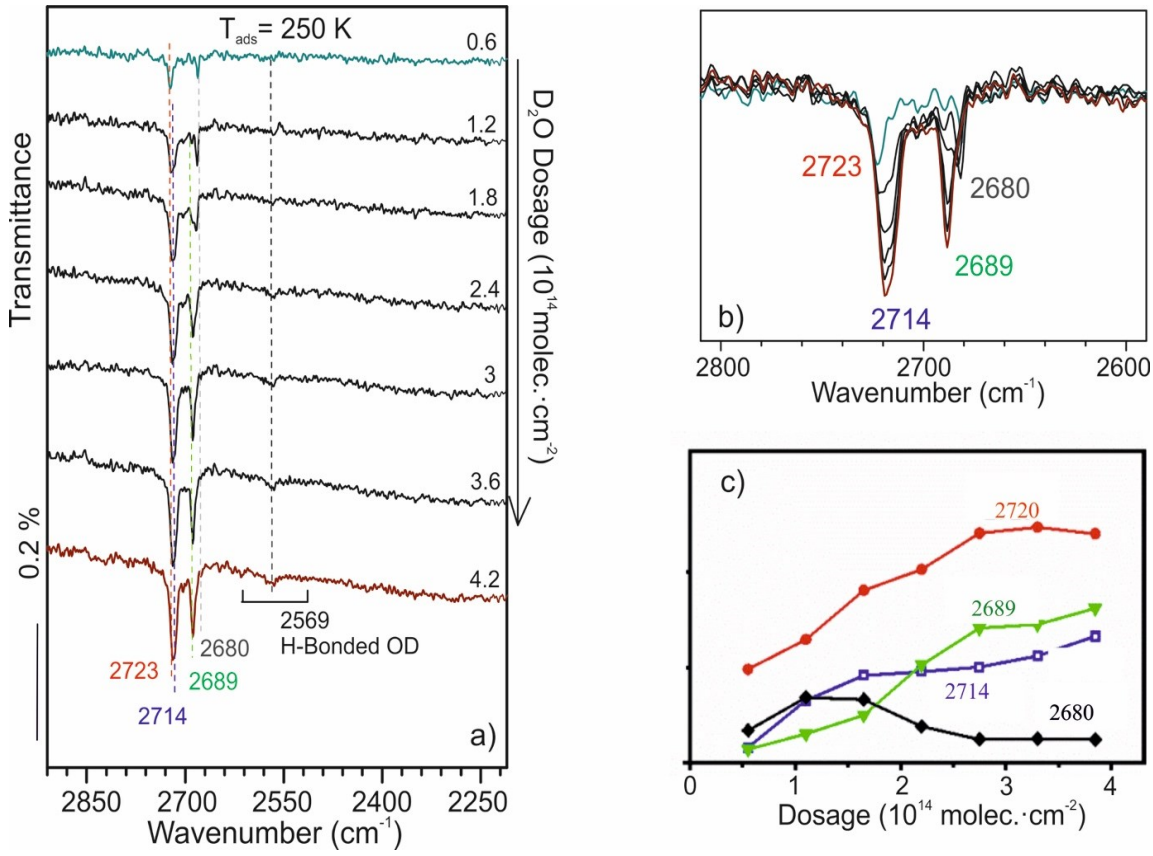


*Fig.5.2. a) IRA spectra of $D_2O$ adsorbed on $Fe_3O_4(111)$ as function of coverage at 250 K. Each water pulse corresponds to a dose of $6 \cdot 10^{13}$ molecules·$cm^{-2}$. b) Spectra in Fig. 5.2a superposed. c) Integral intensity of deconvoluted peaks as function of water dosage.*

The superposition of the spectra in Fig.5.2a is shown in Fig.5.2b and provides a closer look into the details of the spectra evolution. In the case of the higher frequency peak, not only a small red shift is observed, but also a new feature shows up as a shoulder at 2714 $cm^{-1}$, and grows as the coverage increases. On the other hand, the feature observed at 2680 $cm^{-1}$ is present for the first pulses but disappears as the water dosage increases. At the same time, a new peak at 2689 $cm^{-1}$ appears. The trend of the integral intensities of the above-mentioned peaks is shown in Fig. 5.2c. Although the deconvolution may suffer from a low signal-to-noise ratio, it is reasonable to say that the features at ~2723 $cm^{-1}$, 2714 $cm^{-1}$, and 2689 $cm^{-1}$ have all the same tendency and, therefore, they may have the same origin. Also, keeping in mind the information learned from the superimposition of the spectra and the deconvolution of the integral peak intensities, when looking more carefully at the Fig. 5.2a, an inverse correlation between the broad 2569 $cm^{-1}$ feature and the 2680 $cm^{-1}$ peak can be found. Earlier the latter peak was tentatively assigned to water adsorbed on defects sites. If this assignment is correct, the 2569 $cm^{-1}$ band might be related to further water interaction with the pre-existing OD on defects sites responsible for the 2680 $cm^{-1}$ feature.

It is shown that, as the coverage increases, the spectral evolution becomes harder to rationalize. A better understanding of the peak shifts can be achieved by performing isotopically labelled experiments. Different experiments using isotopes were used for this purpose. First, $H_2O$ was adsorbed on a single-pulse $D_2O$-precovered $Fe_3O_4(111)$ at 250 K. The comparison between the above-mentioned experiment and the behavior of pure $H_2O$ on the surface at the same temperature conditions is shown in Fig. 5.3a, in the blue and black spectra, respectively. The pure water on the magnetite surface (black spectra) nicely reproduces the coverage-dependence behavior also found for $D_2O$. In particular, $H_2O$ adsorbs on the surface showing initially two main features at 3690 $cm^{-1}$ and 3634 $cm^{-1}$. As already observed for heavy water (Fig. 5.2a), with increasing coverage the lower frequency band attenuates and then disappears at the same time as a band at 3641 $cm^{-1}$ shows up. Meanwhile, the higher frequency band slightly undergoes red shift and a new feature at 3682 $cm^{-1}$ starts appearing as a shoulder on the pre-existing 3690 $cm^{-1}$ peak, and gains intensity as the coverage increases. When the surface is pre-covered with a single pulse of $D_2O$ (corresponding of a dosage of 0.6 molec.$\cdot 10^{14} \cdot cm^{-2}$) the first signals are the already familiar peaks at 2722 $cm^{-1}$ and 2681 $cm^{-1}$. Upon $H_2O$ exposure on the $D_2O$ pre-covered surface, the

spectral evolution appears different as compared with the pure $H_2O$ behavior. Indeed, the two features at 3682cm$^{-1}$ and 3641 cm$^{-1}$, which in the case of pure $H_2O$ develop later at high coverage, show up immediately. Likely, the first $D_2O$ pulse generates on the surface OD species that are the equivalent of the OH-features having frequency at 3690 cm$^{-1}$ and 3634cm$^{-1}$. Therefore, it can be stated that the species coming from the $H_2O$ interact with the pre-existing OD-species formed upon $D_2O$ pre-coverage of the surface. Interestingly, also the peaks related to the first $D_2O$ pulse undergo shifts as in the case of pure $D_2O$ shown in Fig.5.2a, even if no heavy water is added to the surface. However, the formation of new OD species on top of the pre-existing ones is not possible because no $D_2O$ is added to the surface. Therefore, the observed shift can be interpreted as result of a coverage induced effect.

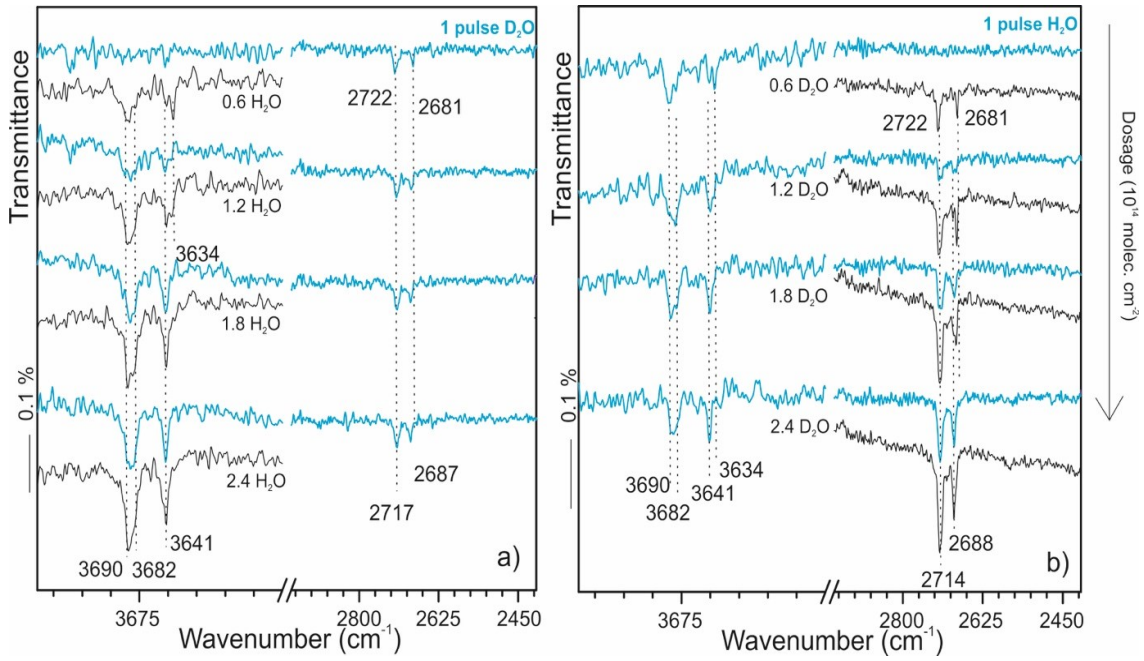


*Fig. 5.3. a) $H_2O$ adsorption on a single-$D_2O$ pulse pre-covered $Fe_3O_4$(111) surface at 250 K (light blue spectra), compared with the pure $H_2O$ adsorption on the clean magnetite surface (black spectra). b) $D_2O$ adsorption on a single-$H_2O$ pulse pre-covered $Fe_3O_4$(111) surface at 250 K (light blue spectra), compared with the pure $D_2O$ adsorption on the clean magnetite surface (black spectra). Each pulse of $D_2O$ or $H_2O$ corresponds to a dosage of 0.6 molec.$\cdot 10^{14} \cdot cm^{-2}$.*

Fig.5.3b shows a similar experiment, executed adsorbing $D_2O$ on a single-$H_2O$ pulse pre-covered magnetite surface at 250 K (blue spectra in the figure), and compared with the pure $D_2O$ adsorbed on the clean surface (black spectra). It is not surprising, that the outcome of this experiment is analogous to what has been observed already in Fig. 5.3a. Thus, the pre-adsorbed water induces the suppression of the first $D_2O$ features (2723 $cm^{-1}$ and 2681 $cm^{-1}$), and the OH signals shift accordingly because of the coverage effect. On the basis of the latter evidence, the following observation can be made: in the low coverage regime, the scenario is characterized by the progressive formation of hydroxo-species whose increasing coverage induces frequency shifts. As mentioned in the Section 3.3.2 of Chapter 3, frequency shifts in infrared spectroscopy can be caused by both dynamic dipole-dipole interactions of neighbor molecules and synergy with the metal oxide support.

Further IRAS experiments using isotopic labelling of oxygen in $D_2O$ as well as in the iron oxide film were carried out, in order to identify the nature of the sharp peaks. Fig. 5.4 shows the comparison between the $D_2O$ adsorption on a regular $Fe_3O_4(111)$ (black spectrum), with, on one hand, the double labelled water $D_2O^{18}$ adsorbed on regular magnetite (red spectrum) and, on the other hand, the "regular" $D_2O$ on $O^{18}$-labelled $Fe_3O^{18}{}_4(111)$ (blue spectrum). Clearly, upon $D_2O^{18}$ dosage on $Fe_3O_4(111)$, the 2720 $cm^{-1}$ peak undergoes shift of about 17 $cm^{-1}$. Additionally, when $D_2O$ is adsorbed on iron oxide prepared with $O^{18}$, the just above-mentioned peak does not shift, but the one usually centered at 2688 $cm^{-1}$ exhibits a blue shift. This is a strong indication that the higher frequency peak (2720 $cm^{-1}$) is related to a terminal Fe-$O_wD$ species coming from the $D_2O$, whereas the lower frequency peak relates to $OD_s$ species containing oxygen from the lattice surface. This experiment is consistent with the "classical model" of water dissociation on magnetite proposed - albeit not proven - in the first place by Leist et al in 2003[70].

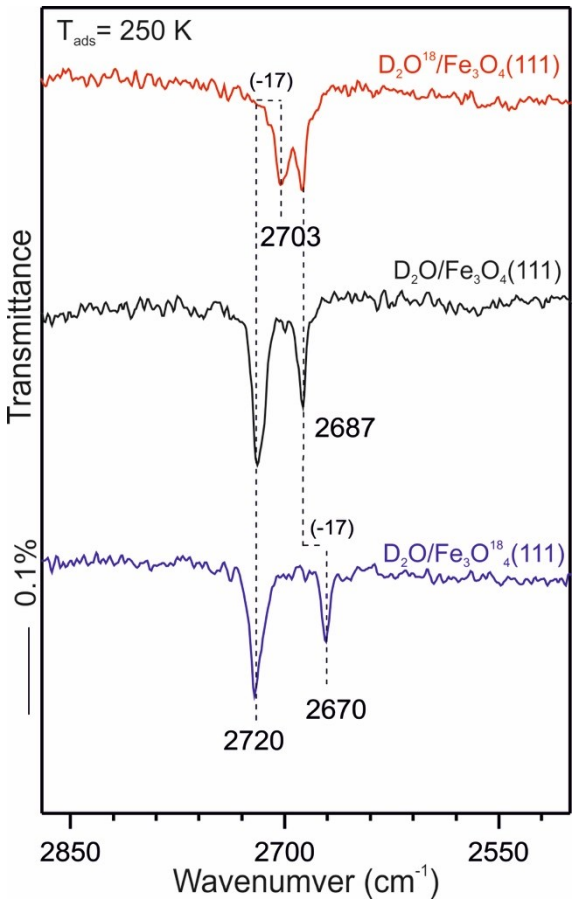


*Fig. 5.4. Infrared spectra for the adsorption of double labelled water $D_2O^{18}$ on $Fe_3O_4(111)$ (red spectra), $D_2O$ on $Fe_3O_4(111)$ (black spectrum), $D_2O$ on iron oxide prepared with $O^{18}$ (blue spectrum). The experiments shown in this figure are performed at 250 K and at saturation conditions ($4.2 \cdot 10^{14}$ molec.$\cdot cm^{-2}$).*

It was already mentioned in Chapter 2, that the latter conclusions were questioned by the data proposed in Ref.[51] The disagreement found in the two studies can be related to the already discussed difficulties associated with the $Fe_3O_4(111)$ surface preparation. Indeed, the study presented in Chapter 4, showed the crucial role of the preparation parameters as well as the vacuum conditions. These variables affect the formation of a uniform $Fe_{tet1}$ terminated surface and, therefore, also the water adsorption on it.

### 5.3 High Coverage Regime

In the following section, the adsorption of water on magnetite in the high coverage regime – i.e., lower adsorption temperatures – will be presented. The first set of experiments was performed at 200 K and it is shown in Fig. 5.5a. In this case, the very first pulse of $D_2O$ adsorbed on the surface produces in a similar, but not identical, scenario as observed for the low coverage regime. Indeed, as in the case of the first stage of water adsorption at 250-300 K, the peak at 2722 $cm^{-1}$ is observed. In the lower frequency region, the first peak appearing is not the "familiar" 2688 $cm^{-1}$, but a brand-new feature having a frequency at 2669 $cm^{-1}$. Only at slightly higher water dosage, the latter band starts attenuating and, at the same time, the feature at 2682 $cm^{-1}$ starts growing. Earlier (Fig.5.1), the lowest frequency band at low coverage was tentatively assigned to water adsorption on defects sites. Accordingly, the mentioned features might form because of surface diffusion. The superposition of the spectra from Fig. 5.5a, shown in Fig. 5.5b, makes easier the understanding of the water behavior at higher dosage. In particular, the whole experiment can be classified into two groups of spectra. The first group depicts the water behavior at low dosage (going from 0.6 to $4.8 \cdot 10^{14} \cdot D_2O$ molecules$\cdot cm^{-2}$): here the spectra look somehow similar to what was observed before in Fig.5.2a at 250 K. The second group, displaying a water dosage from 6 to $11.4 \cdot 10^{14} \cdot D_2O$ molecules$\cdot cm^{-2}$, highlights the more complex spectra evolution with increasing coverage. Hence, the higher frequency band centered at 2720 $cm^{-1}$ loses intensity whereas two features centered at 2712 $cm^{-1}$ and 2707 $cm^{-1}$ gain intensity. On the other hand, the peak at 2688 $cm^{-1}$ shifts to 2693 $cm^{-1}$ and decreases in intensity. Such complex spectra evolution suggests the formation of some complex H-bonded structure at the expenses of simpler species. This is leads to an isosbestic point in the spectra (marked as circle in the Fig.5.5b). The low frequency region is dominated at low dosage by a broad band centered at 2561 $cm^{-1}$, as in the case of the experiment done at 250 K. Later, two broad features centered at 2600 $cm^{-1}$ and 2475 $cm^{-1}$ show up, becoming more prominent at increasing coverage. The two bands are the fingerprints of H-bonded hydroxyl species.

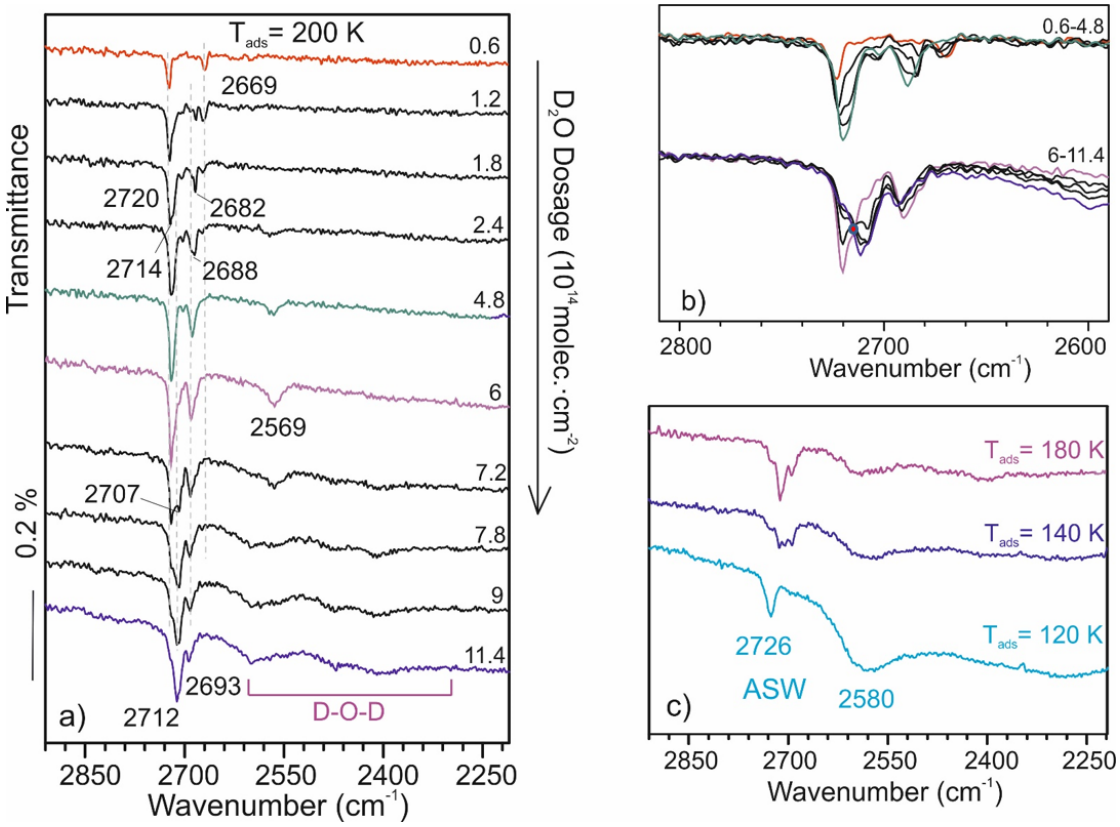


*Fig 5.5 a) IRA spectra of $D_2O$ adsorbed on $Fe_3O_4(111)$ as function of coverage at 200 K. Each water pulse corresponds to a dose of $6 \cdot 10^{13}$ molecules·cm$^{-2}$. b) Spectra in Fig. 5.5a superposed. The isosbestic point is marked as a circle. c) Selected spectra (saturation conditions) of $D_2O$ adsorbed on $Fe_3O_4(111)$ at 140 K, 180 K and 120 K respectively.*

In order to clarify the peak evolution observed so far, further experiments with isotopes were performed. Therefore, keeping in mind what was learned from the experiment shown in Fig. 5.4, further investigations adsorbing $D_2O$ at 200 K on a film grown with $O^{18}$ were carried out. The comparison between the spectra of water adsorbed on regular magnetite and on $O^{18}$-labelled magnetite is shown in Fig. 5.6. As already observed at 250 K, the lower frequency bands (in this case centered at 2681 cm$^{-1}$ and 2669 cm$^{-1}$) undergo a shift when water adsorbs on $O^{18}$-labelled magnetite. These peaks are only observed at the very first dosages, thus could be attributed to adsorption on surface imperfections. Also, the feature at 2681 cm$^{-1}$, observed also at very low coverage, may occur even before the appearance of the Fe-$O_w$D peak at 2723 cm$^{-1}$. If this is true, the above-mentioned adsorption on defects may involve $O_w$D species which have similar

in nature as $O_sD$. This might be the case of adsorption on surface defects such as oxygen-vacancies sites. The O-vacancy might be filled by $O_wD$-species which behave resembling $O_sD$-species.

At higher dosage, the 2688 $cm^{-1}$ peak shifts by ~ 17 $cm^{-1}$, according to the formation of $O_sD$ containing oxygen from the surface. The Figure 5.6 shows clearly that the band at 2672 $cm^{-1}$ on the $O^{18}$-labelled film is well-separated from the rest of the bands in the high frequency region (see Fig. 5.5a for comparison). This suggests that the hydroxyl species involving surface oxygens ($O_sD$), participate to further water coordination via H-bonding, which typically leads to band broadening and strong red-shift of about 250 $cm^{-1}$. Besides, the other hand, the broad band at 2565 $cm^{-1}$, characteristic for H-bonded species, does not shift when $D_2O$ is adsorbed on the $^{18}O$-labelled surface. This suggests that the molecular water contribution only involves $O_wD$-species.

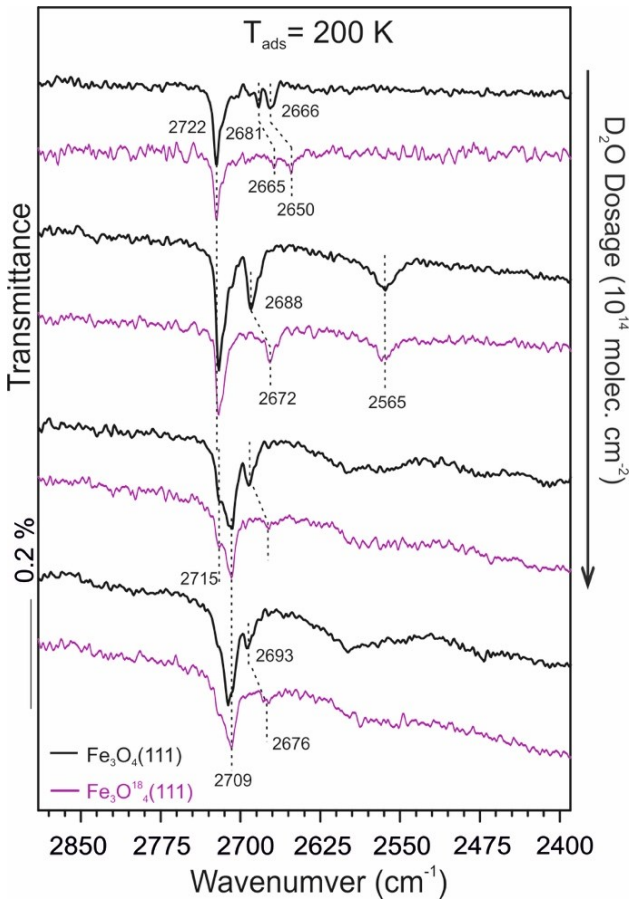


*Fig. 5.6. Infrared spectra of $D_2O$ adsorbed at 200 K on regular $Fe_3O_4(111)$ (black lines) and on $O^{18}$-labelled $Fe_3O_4(111)$ (pink lines).*

After the above description of the infrared data in both low and high coverage regimes, the proposed overall picture follows.

At higher temperatures (see Fig. 5.1) the scenario is dominated by adsorption of water on defect sites, while, at increasing coverage, the primary event is the dissociative adsorption on regular $Fe_{tet1}$ surface giving rise to a Fe-$O_w$D (~ 2720 $cm^{-1}$) and an $O_s$D (2688 $cm^{-1}$). Both bands undergo shift as the coverage increases, probably due to a substrate-mediated dipole-dipole interaction (see again Chapter 3, Section 3.3.2).

The high coverage scenario, with the evolution of several sharp peaks as well as the contribution of the molecular water, is harder to interpret only by means of infrared techniques. As already mentioned in the introduction, metal oxides surfaces, and - in particular - magnetite, are very complex systems and the understanding of the adsorption processes on these surfaces is a notoriously challenging task. A joint effort between several different experimental techniques (and setups) as well as theoretical support, must be employed in the attempt of a unified picture of the water interaction with this surface.

Particularly, further experiments, by means of temperature programmed desorption technique, were performed in two different UHV setups. Figure 5.7 shows water TPD spectra measured after $D_2O$ exposure on the $Fe_3O_4$(111) surface at 140 K and 250 K, in the same UHV chamber used for the IRAS experiments (see Section 3.3.5, Chapter 3). In the water desorption profile three major features (two of them sharper and one quite broad) can be distinguished at ~193 K, 230 K, and 270 K. Above 270 K, a shoulder at ~305 K and a very small desorption feature at 375 K appear (the latter assigned to water adsorbed on surface imperfections).

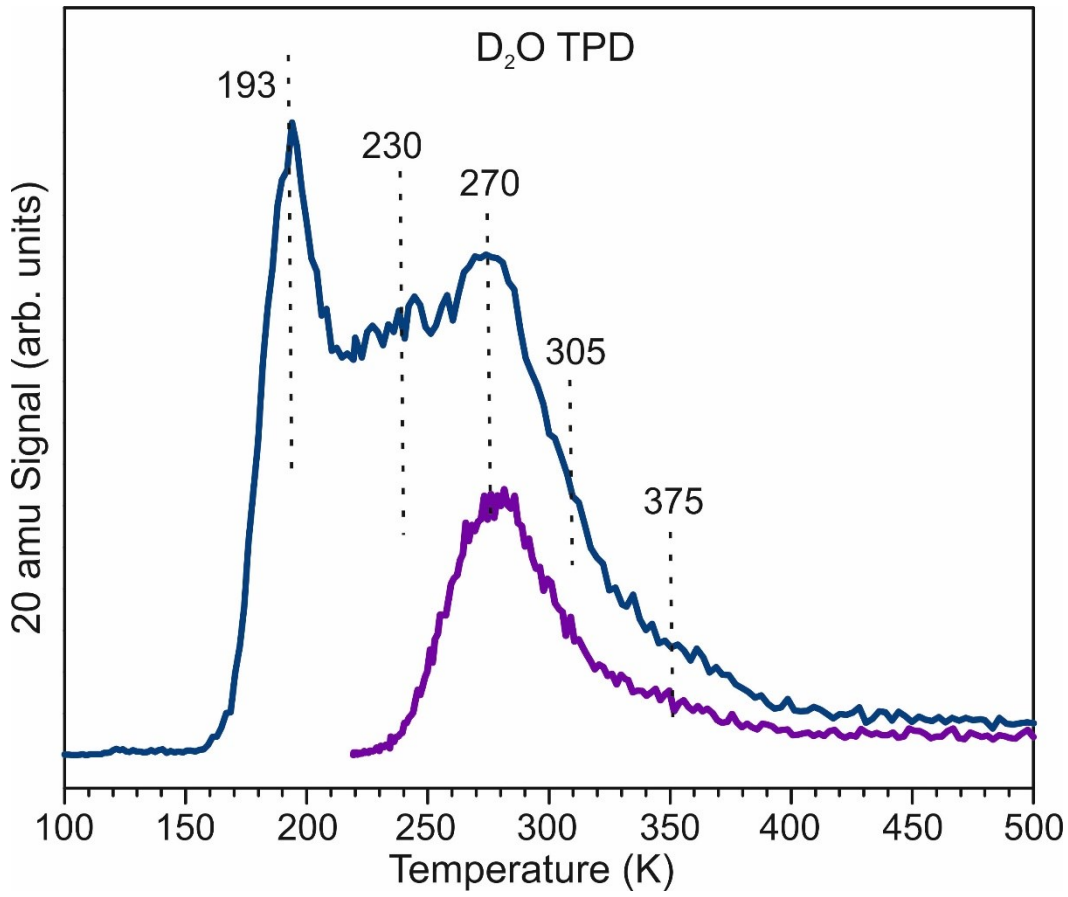


*Fig. 5.7. TPD spectra measured after IRAS experiments performed at 140 K (blue line) and 250 K (purple line). The heating rate is 3 K/s.*

These spectra differ considerably with the ones reported by Joseph et al.[67], who showed a TPD profile characterized by featureless desorption traces in the 200–300 K region. This behavior can be interpreted as a consequence of the surface heterogeneity and/or reorganization of ad-species during the TPD run, leading to broadening and smearing desorption features. However, this cannot be applied to the surface prepared in this work (see recipe described in the Section 4.2, Chapter 4), which exposes a single $Fe_{tet1}$-termination[140]. On the contrary, the presence of resolved peaks in the spectra showed in Fig. 5.7, suggests that water molecules/aggregates with discrete binding energies desorb individually.

Moreover, the presented TPD spectra show quite similar desorption profiles to those measured in a different UHV setup and presented in Ref[158]. The deviations in the temperature reading in the two different TPD experiments are certainly related to the different sample holders and thermocouples used in the two setups, whereas the lack of resolution observed in the spectra in Fig. 5.7 is due to the absence of differential

pumping stages in the mass-spectrometer. Nevertheless, the two experiments can be considered as equivalent and this allows to link the TPD and IRAS results performed in the two different setups.
As this work is mainly focused on the spectroscopic aspect of the water adsorption process on magnetite, the details of the temperature programmed desorption data will be deepened elsewhere[159].

Moreover, LEED experiments of water adsorbed on the same magnetite surface as function of coverage reported in Ref.[158], reveal additional spots arranged in a (2x2) pattern in the range of temperatures between 190 and 280 K. In the same temperature range, the IRA spectra - reported in Fig. 5.5 - showed increasing molecular water contribution, whereas the TPD profiles display resolved desorption features (Fig. 5.7).

The experimental evidences obtained combining the three techniques suggest a rearrangement of the water ad-layer in a (2x2) ordered structure. There are only a few examples in the literature of water ordered ad-layer at the interface with the metal oxide[152,160,161]. In the case of water adsorbed on MgO(100), likely the most intensively studied system[151], LEED experiments showed *c*(4×2) and *p*(3×2) patterns, which were then rationalized by DFT calculation in terms ordered structures, stable at low and higher temperatures, and containing ten and six water molecules per unit cell, respectively. However, it is still not entirely understood which driving force leads the water to aggregate in such a way on the oxide surface.

It seems clear that, to shed light on the atomic structure of the water ad-layer on $Fe_3O_4$(111), and so provide a unified picture to the experimental observations, the input from the theoretical point of view is required. DFT calculations have been, then, performed by Xiaoke Li and Joachim Paier in the Humboldt University in Berlin, to analyze the formation of the water ordered structure in a $Fe_3O_4$(111)-(2x2) unit cell. The outcome from the theory will drive us to the conclusions of this section.

## 5.4 Density Functional Theory Results

DFT calculations show that, when water is dosed on $Fe_3O_4(111)$ surfaces, a dissociative adsorption is the thermodynamically most stable process, with a calculated adsorption energy of -123 kJ/mol. The calculated structure for the dissociated water molecule ("monomeric species") is shown in Fig. 5.8 and includes a terminal $O_wD$ on top of a Fe cation and an $O_sD$ which forms involving a surface oxygen. The same figure also shows the calculated frequencies for the latter species, 2736 $cm^{-1}$ and 2699 $cm^{-1}$, respectively. These are in very well agreement with the ones observed experimentally (2720 $cm^{-1}$ and 2688 $cm^{-1}$), under the assumption the very first peak appearing at 2681 $cm^{-1}$ (Fig. 5.1) is related to the adsorption of water on defects sites.

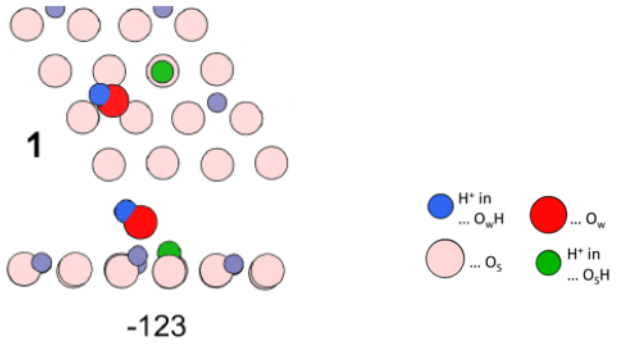


| | $O_wD$-$Fe_{tet1}$ | $O_sD$ | $\Delta_v$ ($cm^{-1}$) |
|---|---|---|---|
| $\nu_{calc.}$ | 2736 | 2699 | 37 |
| $\nu_{obs.}$ | 2720 | 2688 | 32 |

*Fig.5.8. The upper part of the Figure shows the top and side views of a single water molecule dissociated on $Fe_3O_4(111)$ surface. Surface $Fe_{tet}$ ions are violet, surface $O_s$ ions are pink, oxygen n water ($O_w$) is red, proton atop $O_s$ is green, hydrogen in water is blue. The bottom part of the Figure shows a table which compares the calculated and observed vibrational frequencies for $O_wD$-$Fe_{tet1}$ and $O_sD$.*

When a second water molecule arrives on the surface, it may either dissociate as the first one, or form dimer anchoring the already adsorbed "monomer" on the surface. At coverages up to 1ML (~ four molecules per unit cell), the energy gain for the monomer formation is substantially higher than for the dimer formation[158]. Hence, for this coverage conditions, DFT calculations predict structures containing monomeric species, although dimers formation becomes highly probable[159,162]. Accordingly, in a unit cell, up to 4 water molecules will dissociate, and this is considered the initial stage for water adsorption on $Fe_3O_4$(111). Additional molecules do not dissociate and add on the surface in such a way to maximize the H-bonding interaction[24].

The calculated frequencies of $O_wD$ and $O_sD$ for selected structures, containing one to seven water molecules per $Fe_3O_4$(111)-(2x2) unit cell, are summarized in Fig. 5.9. In the figure, in the case of five, six and seven water molecules per unit cell, the structures are indicated with the superscript *cl* and *n*, meaning the difference between "clustered" structures (groups of oligomers on the surface) and hydrogen-bonded dimers and monomers[159].

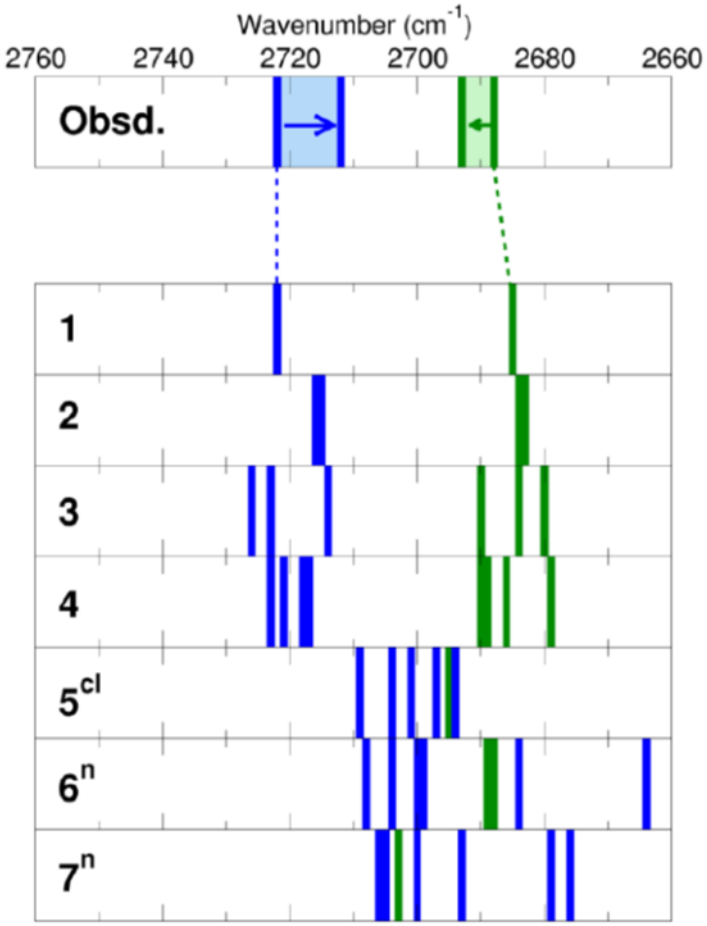


*Fig.5.9. Stick representation of calculated frequencies for $O_wD$ (blue) and $O_sD$ (green) for structures containing 1 to 7 water molecules per unit cell, for comparison with the one observed experimentally and showed in the top panel.*

As the coverage increases, a calculated red-shift of 10 $cm^{-1}$ in the $O_wD$ frequencies (blue sticks), and a blue-shift of 5 $cm^{-1}$ for the $O_sD$ modes (green sticks), is observed. Moreover, the calculated $O_sD$ vibrational frequencies (green sticks) for the structures $5^{cl}$, $6^{n}$, and $7^{n}$ show a red shift of ~16 $cm^{-1}$, when compared to ones for low coverage structures (one to 4 water molecules per unit cell). The latter finding agrees very well with the experimental observations showed earlier in this chapter. In particular, among the potential candidates, the structures labelled as $5^{cl}$ and $6^{n}$ seem to be in best agreement with the IRAS experiment performed at 200 K (see Fig. 5.5a). Reasonably, the formation of these more complex structures develops at expense of the less complex "monomeric" species, giving rise of the isosbestic point already discussed in Fig.5.5b. Furthermore, according to what observed experimentally in Fig. 5.5c, at

increasing coverages all computed OD bands start to overlap with each other, resulting into one feature. The latter band can be related to the experimental one centered at 2712 $cm^{-1}$, which monopolize the scene at 120 K, before the ice multilayer starts growing.

## 5.5 Conclusions

The presented work studied in detail the adsorption of water on the $Fe_3O_4$(111) surface in different coverages regime. Infrared data confirmed the prediction of Leist et al. (known as "classical model"), where water in the initial stage of the adsorption readily dissociates on the $Fe_{tet1}$-terminated surface giving rise of two hydroxyl species, $O_wD$ and $O_sD$, involving oxygen atoms from the water (w) itself and from the oxide surface (s), respectively. At higher coverage, water molecules start forming dimer and more complex oligomers through the pre-existing hydroxyl on the surface, reflected by the presence of the isosbestic point in the IRA spectra. These oligomeric species ultimately assemble in a hydrogen-bonded network architecture, prior formation of the ice multilayer.

The focal point of the obtained results is the important role played by the hydrogen bonds which favor the formation of particular structures in the water ad-layers, driven by a thermodynamic force known as cooperativity[158,163].

# 6. Interaction of $CO_2$ with $Fe_3O_4(111)$

## 6.1 Introduction

The interest on $CO_2$ has raised enormously in the last two decades, being involved in the methanol synthesis[164] and also as one the most important greenhouse gases[78]. Indeed conversion of $CO_2$ into fuels and other value-added chemicals is a currently hot topic addressed by obvious environmental and economic motivations[165]. However, $CO_2$ displays the most oxidized state of carbon which renders it rather inert to chemical transformations, thermodynamically highly unfavorable. Furthermore, the use of water as hydrogen resource (instead of hydrogen itself) for $CO_2$ reduction/hydrogenation would be the most ideal process which remains challenging. Despite certain advances in this field, further fundamental studies need to be addressed to understand the interaction of water and $CO_2$ with catalyst substrates, especially metal-oxide surfaces, for rational design of heterogeneous catalytic processes. In this sense the progresses in the last years in the preparation and characterization of thin oxide films exposing polar surfaces[12] made possible such investigation.

However, as already mentioned in Section 2.5 of Chapter 2, fundamental investigations on transition metal oxides surfaces are scarce. Nevertheless, it can be found in the literature that $CO_2$ interacts stronger with metal oxides, rather than with clean metal surfaces[166], and mainly physisorption (on $TiO_2$[167], ZnO[168], and MgO[169,170]) and different carbonates formation (on CaO[171,172], $Cr_2O_3$[173,174], $Al_2O_3$[81]) have been observed. Besides, it seems that this interaction is favored when it involves surface imperfection (i.e., oxygen vacancies) rather than regular surface sites[175,176].

On the $CO_2$ adsorption on magnetite surfaces, although the versatility of these oxides makes them potentially suitable for such a purpose, the information is even less dense. Very recently, Pavelec et al.[175] investigated the $CO_2$ adsorption on $Fe_3O_4(100)$ single crystals, and proposed a model where $CO_2$ adsorbs initially and most strongly on $Fe^{2+}$-related defects, to then form a physisorbed monolayer with molecules adsorbed on regular surface sites. Density functional theoretical calculations performed on $Fe_3O_4(111)$ surfaces suggest that carbon dioxide chemisorbs binding undercoordinated oxygen sites[177]. However, to the best of our knowledge, there are no experimental studies facing up to the $CO_2$ activation on well-defined $Fe_3O_4(111)$ surfaces.

In this chapter, a "surface science" study of the interaction of $CO_2$ with well-characterized $Fe_3O_4$(111) films grown on Pt(111) single crystal[140], by means of infrared reflection absorption spectroscopy, is presented. Experimental data of $Fe_3O_4$(111) surfaces exposed to $CO_2$ show, at lower temperatures (~120-150 K), mainly contribution from weakly bound species ($CO_2$ phisysorption), although small chemisorbed features can be detected. The formation of the latter species might be interpreted as driven by the presence of surface imperfections[175,177]. At higher temperatures (~200-240 K) stronger chemisorption evidences are observed. However, at this temperature conditions, the sensitivity of the surface towards preparation conditions and residual gas adsorption (in particular of water)[140,158,72,159] has to be taken into account. Indeed, as already observed in Chapter 5, the presence of OH groups on the surface is unavoidable because water readily dissociates on magnetite. It will be shown at the end of this chapter that, in these conditions, the hydroxyl groups present on the surface play a critical role in the early stage of the $CO_2$ activation, promoting the formation of bicarbonate-like species.

## 6.2 $CO_2$ Adsorption on the Clean Surface

Isothermal interaction of $CO_2$ on the surface of a well-defined $Fe_3O_4$(111) film was spectroscopically (IRAS) investigated as a function of surface temperature (within the 120-280 K range) and exposure. Fig. 6.1 shows a series of IRA spectra obtained after $CO_2$ adsorption on the magnetite at different surface temperatures (120 K, 140 K, 200 K, 240 K, 280 K). It is important to mention that the experiments showed below are performed after a relatively high carbon dioxide dosage, i.e. $3.6 \cdot 10^{17}$molec.$\cdot$cm$^{-2}$ and $1.1 \cdot 10^{18}\cdot$molec.$\cdot$cm$^{-2}$ (Fig 6.1a and Fig.6.1b respectively). At lower exposures (not shown) $CO_2$-related signals can hardly be seen. The latter observation might indicate that the regular magnetite surface could be rather inert towards $CO_2$ chemisorption, and that the observed species form binding uncoordinated sites[175,177].

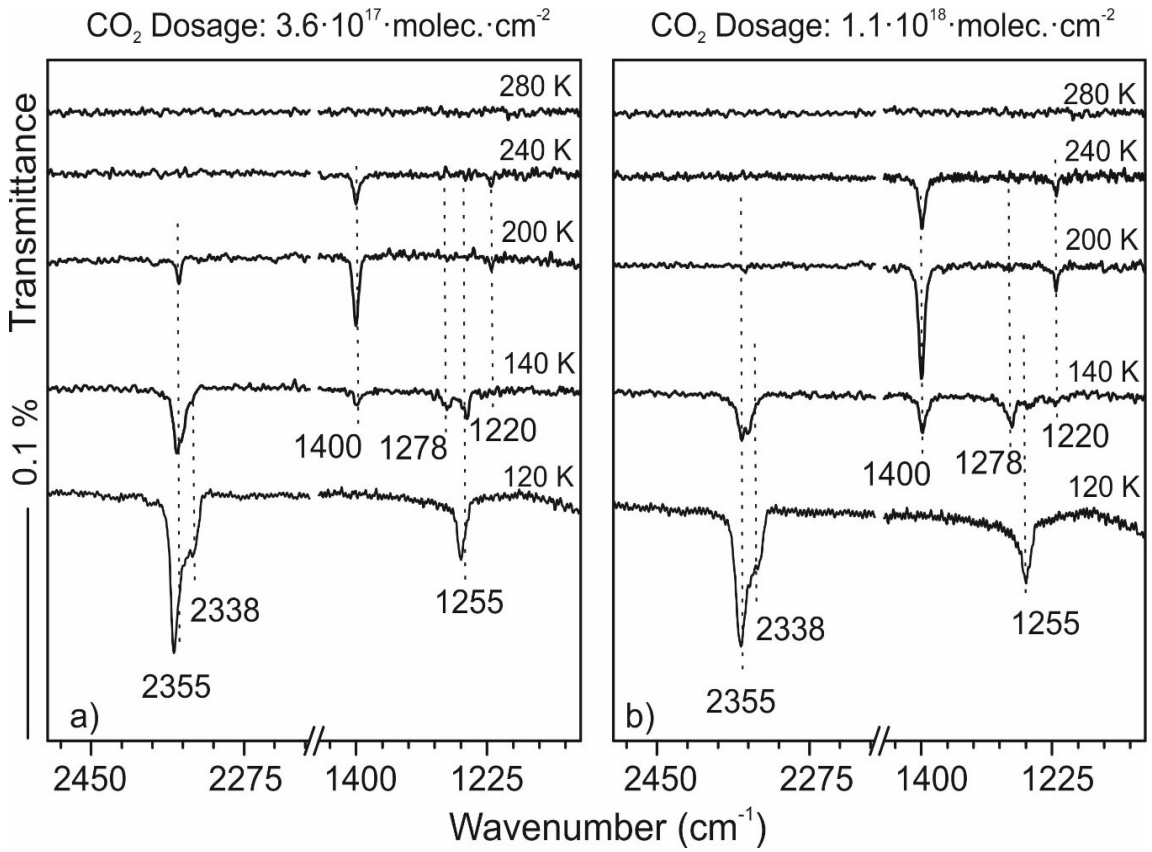


*Fig.6.1. $CO_2$ exposure on $Fe_3O_4$(111) at different surface temperatures (280K, 240K, 200K, 140K, 120K). The same temperatures at different $CO_2$ exposures are compared: (a) shows a dosage of $3.6 \cdot 10^{17}$ molec.·cm$^{-2}$, whereas (b) of $1.1 \cdot 10^{18}$ molec.·cm$^{-2}$.*

Nevertheless, different $CO_2$ behavior at different surface temperatures is observed. In particular, the lower temperatures seem to be the most promising for the $CO_2$ activation. At lower exposure ($3.6 \cdot 10^{17}$ molec.·cm$^{-2}$), the higher wavenumbers region of the spectra is dominated by a sharp peak centered at around 2350 cm$^{-1}$, characteristic of the asymmetric stretching mode of physisorbed $CO_2$ molecule[174]. The latter peak loses its intensity when going from 120 K, where it is accompanied by a shoulder at around 2338 cm$^{-1}$, to 200 K and disappears completely at 240 K. On the other hand, in the region between 1100 and 1500 cm$^{-1}$ a set of bands which are consistent with chemisorption are distinguished by different growth rates with a dependence on the surface temperature. Indeed, while at 120 K only a signal at around 1255 cm$^{-1}$ is detected, at 140 K and lower $CO_2$ exposure three main peaks are observed at 1400 cm$^{-1}$, 1278 cm$^{-1}$ and 1254 cm$^{-1}$. At increasing coverage (Fig. 6.1b), the ratio of intensities of the latter species changes: the 1400 cm$^{-1}$ and the 1278 cm$^{-1}$ features gain intensity,

whereas the 1255 $cm^{-1}$ peak - before higher in intensity than the others - loses it. Also, at this coverage a tiny peak at 1220 $cm^{-1}$ can be observed.
At 200 K, only the two chemisorbed-like species at 1400 $cm^{-1}$ and 1220 $cm^{-1}$ are detected, which gain intensity with increasing dosage. At this temperature, the physisorbed contribution is smaller and no longer visible, even at higher $CO_2$ exposures. At 240 K, physisorption is not observed from the onset, and the same features observed also at 200 K are identified. At this temperature, the chemisorbed species seem to be smaller in intensity, even if their contribution is slightly higher at higher exposures. Finally, at temperatures above 240 K, no $CO_2$ contribution can be found.

As already widely discussed in Chapter 2, Section 2.5, the assignment if the IRA features is difficult and several adsorbate species including $CO_2^-$, $C_2O_4^{2-}$ and various types of $CO_3^{2-}$ must be included in the discussion[174]. The main difficulty in the peak assignment is because such intermediates are characterized by vibrational features which fall all in the same range of frequencies. Plus, several of these chemisorbed-species can be simultaneously present at the surface and therefore overlap. To have a more detailed insights on the behavior of $CO_2$ on the surface at the different temperatures, the full trend of the carbon dioxide adsorption on $Fe_3O_4$(111) as a function of coverage at 120 K (a), 140 K (b) and 200 K (c), is shown in Fig. 6.2.

Before going into the details of the above-mentioned experiments, assigning the IRA features, a few considerations must be made. Since the features related with the carbon dioxide chemisorption are relatively small in intensity, experiments using isotopic substitutes were also performed to confirm if the signals are originating from the molecular beams or from residual gas in the chamber background. The Fig. 6.2 shows, for each temperature, the spectra obtained for the $^{13}CO_2$ (red spectra) and $CO^{18}{}_2$ (blue spectra) adsorption on magnetite at saturation conditions. Clearly, upon isotopes adsorption, the shifts expected for $^{13}C$- and $O^{18}$- labelled molecules are observed for both, physisorbed and chemisorbed features. Therefore, it is possible to conclude that all the adsorption bands observed in the IRA spectra are originated from bonds vibrations of carbon dioxide, dosed with the molecular beams.

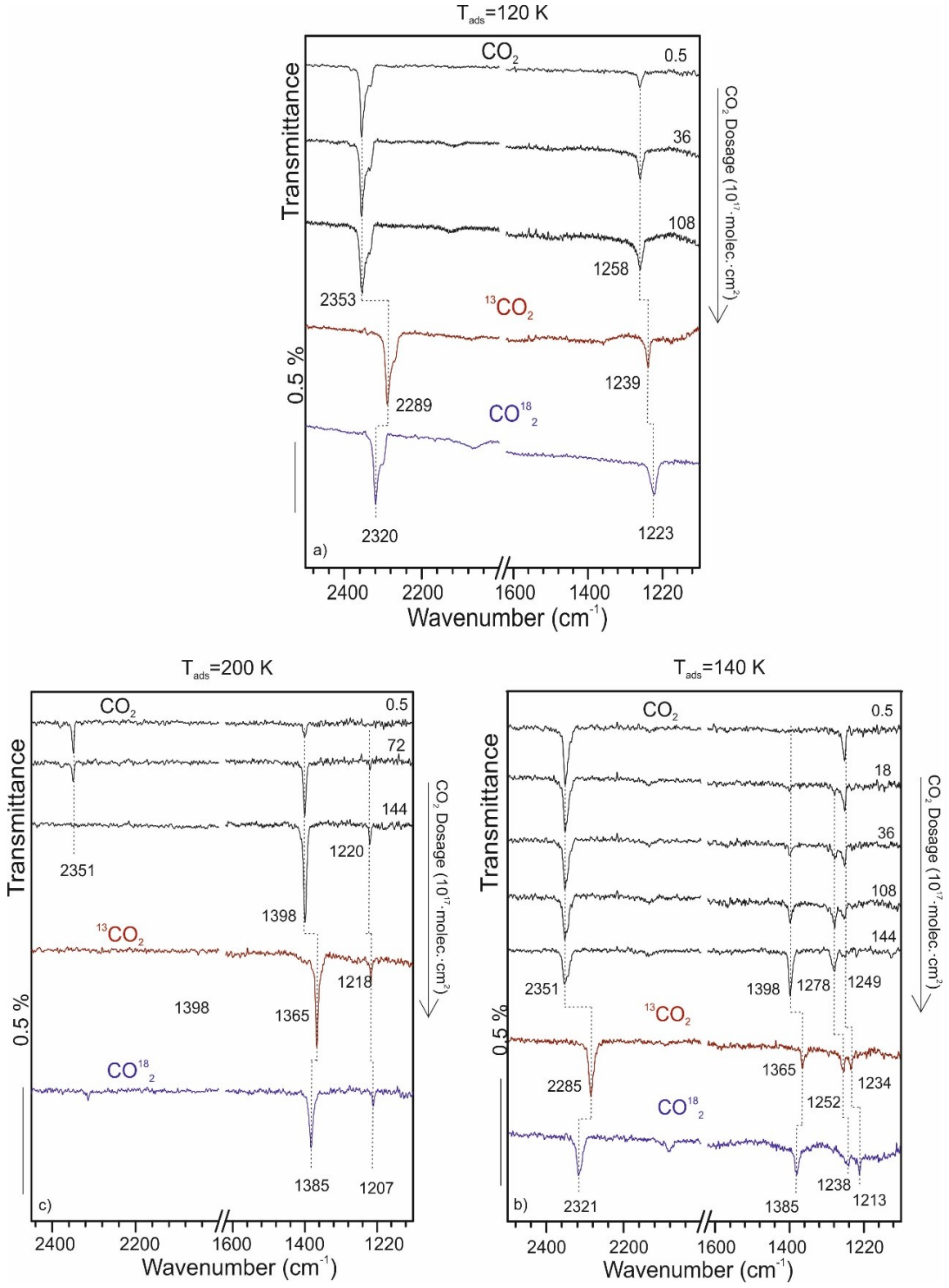


*Fig.6.2. IRA spectra of the $CO_2$ adsorption on $Fe_3O_4(111)$ as a function of coverage at 120K (a), 140 K (b), 200 K (c). Each set of experiment shows also the corresponding adsorption spectrum for isotopically labelled $^{13}CO_2$ (red spectra) or $CO^{18}{}_2$ (blue spectra) at saturation conditions.*

As already mentioned, at 120 K the spectra are dominated by physisorption characterized by a sharp peak centered at about 2353 $cm^{-1}$. On the chemisorption side, a single feature is observed which shows up immediately at 1258 $cm^{-1}$ and growths in intensity with increasing coverage. At higher temperatures (140 and 200 K), the spectra evolution results more complex.

The following analysis of the peaks evolution in the chemisorption region is based on the first approximation that the physisorbed-$CO_2$ acts as a spectator, not affecting the chemisorption process.

Fig. 6.3 provides a zoom of the chemisorption region in the IRA spectra obtained at 140 K and 200 K.

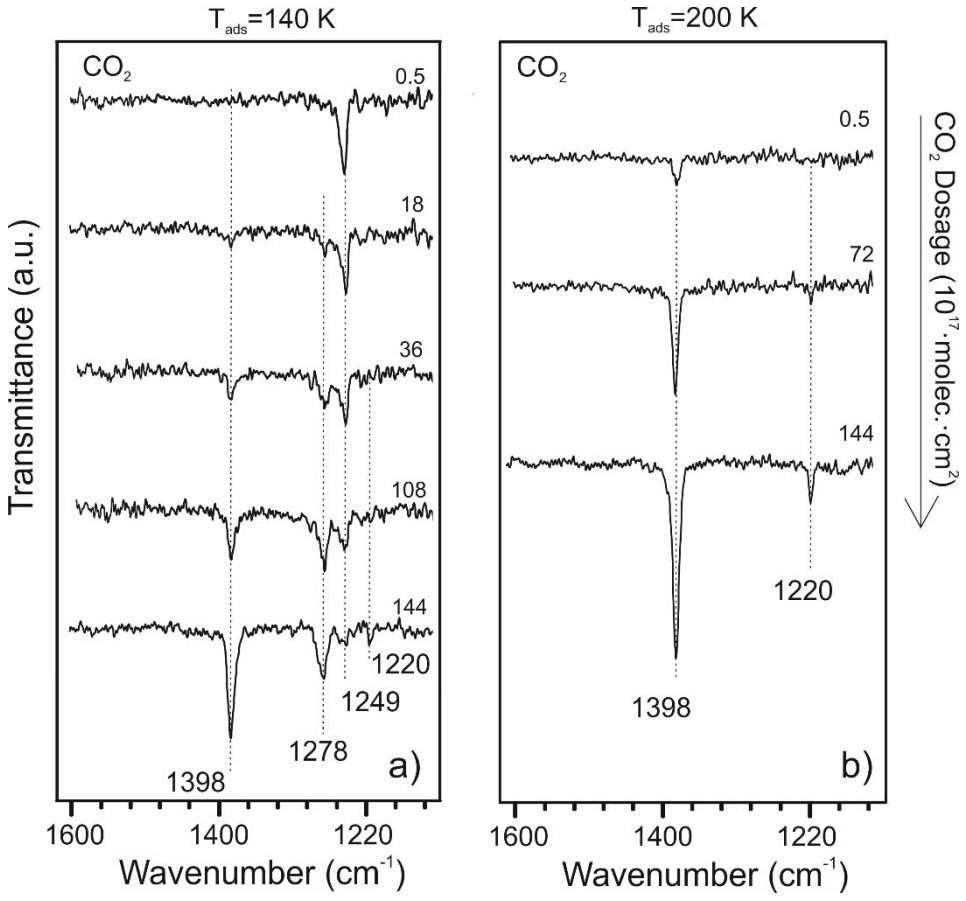


*Fig.6.3. Zoom of the chemisorption region of the IRA spectra for the $CO_2$ adsorption on $Fe_3O_4$(111) as a function of coverage at 140 K (a), and 200 K (b).*

At 140 K the first peak shows up at 1249 $cm^{-1}$ and decreases in intensity as the coverage increases. Finally, it "converts" into the peak centered at 1278 $cm^{-1}$, which growths at higher $CO_2$ exposures on the surface.

Furthermore, another peak starts to grow around 1398 $cm^{-1}$ accompanied, at very high exposures, by a small feature at 1220 $cm^{-1}$. At higher temperature, the latter species, 1398 $cm^{-1}$ and 1220 $cm^{-1}$, are present on the surface from the very beginning and gain intensity as the coverage increase. However, the earlier observed peaks at 1258 $cm^{-1}$ and 1278 $cm^{-1}$, cannot be longer seen at this temperature.

An attempt to assign the observed IRA features follows. The first species that gets formed at 120 K and 140 K, observed at 1255 $cm^{-1}$, is consistent with the symmetric stretching of the O-C-O bond of bent negatively charged $CO_2$, also known as carboxylate ($CO_2^-$)[173,174]. These species seem to be stable only at temperatures < 200 K. Also, carboxylate formation is more favored on metals substrates with a low work function[8], even though the proper adsorption sites existence plays also an important role.

As shown in Table 6.1, carboxylates have three infrared-active modes, the symmetric and antisymmetric O-C-O-stretching and the bending vibration, which are centered at around 1200-1300 $cm^{-1}$, 1600 $cm^{-1}$ and 800 $cm^{-1}$ respectively. The bending vibration is at the border of the frequency range accessible with the IRAS set-up used in this work and, therefore, hard to detect. Also, such species can adsorb on the surface in two different geometries, through the carbon atom, or with both oxygens standing on the surface iron. If the $CO_2^-$ is adsorbed in a $C_{2v}$[178] symmetry, it is not possible to see the antisymmetric stretching because of surface selection rules[179]. Hence, the peak at 1255 cm-1 (Fig. 6.2a-b) is consistent with the symmetric stretching vibration of carboxylates adsorbed in $C_{2v}$ symmetry. Indeed, no features around 1600 $cm^{-1}$ is detected, suggesting that the $CO_2^-$ might be adsorbed with the alignment of the O-O axis parallel to the surface.

| System | 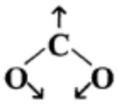 δ | 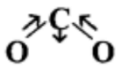 $\nu_s$ | 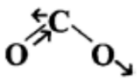 $\nu_{as}$ |
|---|---|---|---|
| $CO_2$/Ni(110) | 700 | 1130/1390 | 1620 |
| $CO_2$/Re(0001) | 650 | 1230 | 1625 |
| $CO_2$/$Fe_3O_4$(111) | 800 | 1064/1160 | 1360/1600 |
| $CO_2$/$Fe_3O_4$(100) | | 1232 | 1634 |

*Table 6.1. Computed vibrational frequencies (in $cm^{-1}$) of carboxylate species ($CO_2^-$). The table is adapted from Ref.*[173] *and references therein.*

Nonetheless, as already specified in Chapter 3, Section 3.5, the $CO_2$ chemisorption on metal oxides is primarily associated with the formation of different types of carbonate-like species[81,173]. Hence, at 140 K, the peak associated with $CO_2^-$, which appears from the very beginning of the exposure, decreases in intensity with increasing exposure and slowly converts into the band at 1278 $cm^{-1}$. On the basis of previous studies the latter feature can be identified as surface-carbonates[81,173,174].

There is a simple model in literature, which describes a charge transfer from the oxygen in the surface lattice to the carbon dioxide molecule approaching and, then, bending giving rise to a $[O\text{-}CO_2]^{2-}$ complex[180]. Table 6.2 summarizes the frequencies for mono-dentate carbonates adsorbed on metal oxides involving oxygen from the surface.

Although the corresponding adsorption sites are considerably different (oxygen vs iron ions), this process is somehow analogous to the formation of the $[M^+\text{-}CO_2^-]$ and this could justify our experimental observations. Further theoretical calculations of the optimized geometries of such molecules on a $Fe_{tet1}$-terminated magnetite will be needed in the future.

| | $\delta(O_sCO)$ | $\delta(OCO_s)$ | $\pi$ | $\nu$ (C-$O_s$) + $\nu$ (C-O) | $\nu$ (C-O) + $\nu$ (C-$O_s$) | $\nu$ (C-O) |
|---|---|---|---|---|---|---|
| System | 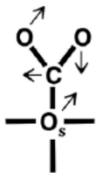 | 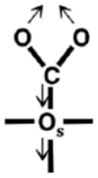 | 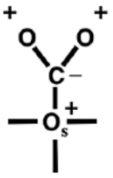 | 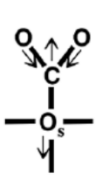 | 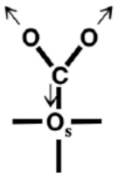 | 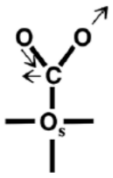 |
| Frequencies | 680-700 | 700-780 | 850-860 | 1050-1070 | 1350-1370 | 1450-1490 |

*Table 6.2. Vibrational frequencies (in $cm^{-1}$) of monodentate carbonates species. The surface oxygen is labelled as $O_s$ .The table is adapted from Ref.*[173] *and references therein.*

As for the carboxylates, also the surface-carbonates decompose at temperatures ≥200 K. At these (higher) temperatures the only visible features in the IRA spectra are the two peaks having frequencies at ~1398 $cm^{-1}$ and 1220 $cm^{-1}$. The nature of these species was for long time under debate and their assignment is one of the aims of this work. Previous studies assigned these peaks to oxalate species[95,170]. Oxalates are dimer-like molecules which could be easily formed through the reaction between a carboxylate sitting on the surface and another $CO_2$ molecule coming from the beam. The bands observed in the IRA spectra in Fig. 6.3b, fall in the range of frequencies typically associated with oxalates. Although, this fits our experimental observations, some considerations must be done. First of all, theoretical calculations suggest for the adsorption of this molecule on the surface a planar configuration as the most stable one[170]. As mentioned earlier in this Chapter as well as in the Section 3.3.2 of Chapter 3, when a molecule is arranged on the surface in a way that makes the perpendicular component of the dipole moment equal to zero, because of surface selection rules, no IR-vibration will be detected[179]. Because of that, even if a molecule is present on the surface, it cannot be detected. This represents one of the limitations of the IRAS technique on a metal-oxide substrate: if some molecules are not observed, it is not necessarily straightforward that they are not present on the surface. Indeed, oxalates are predicted to be quite stable as $CO_2$-intermediate, but it seems to be unlikely to detect them by IRAS.

An interesting experiment performed with isotopically labelled $CO_2$ molecules may be used to discern which type of molecule is being formed, i.e. to distinguish between a dimeric species –such as oxalates– or of a monomeric one. Indeed, when regular $CO_2$ and $^{13}C$-labelled $^{13}CO_2$ are simultaneously sent to the surface, two possible scenarios can happen. If a dimer is formed on the surface, the corresponding IRA features splits into three different peaks, having a ratio of intensity of 1:2:1. These peaks correspond to the dimer-species formed by two $^{12}C$ ($^{12}C$-$^{12}C$), to one obtained from the statistical combination of the two isotopes ($^{13}C$-$^{12}C$; $^{12}C$-$^{13}C$), and to the dimer with two $^{13}C$ ($^{13}C$-$^{13}C$), respectively. If the statistical combinations of the two C-isotopes gives two not identical molecules and if the experimental setup is able to distinguish between them, then a splitting in four peaks with a ratio of intensity of 1:1:1:1 will be observed.

The case of the monomer formation appears quite different from what was described above. Hence, no splitting occurs, and the IRA spectrum is characterized by two well separated peaks, which are the signatures for the monomers formed with $^{12}C$ and $^{13}C$, respectively. The just described experiment is illustrated in Fig. 6.4. The figure depicts the comparison between the co-adsorption of regular $CO_2$ and $^{13}C$ -labelled $^{13}CO_2$, the co-adsorption of regular $CO_2$ and $O^{18}$-labelled $CO^{18}{}_2$, and the adsorption of pure $CO_2$ on $Fe_3O_4$(111) at 200 K.

In this experiment, only the changes in the 1398 $cm^{-1}$ peak will be discussed, because the 1220 $cm^{-1}$ feature is too low in intensity and hard to examine since, as shown already in Fig. 6.2, the shifts concerning it are too small to be appreciated. Clearly, upon co-dosage of $CO_2$ and $^{13}CO_2$ on the magnetite surface, no splitting for the 1398 $cm^{-1}$ is observed. Instead, two separated peaks appear at 1398 $cm^{-1}$ and at 1365 $cm^{-1}$ in correspondence of the molecules formed with regular C and labelled $^{13}C$ (with the shift expected for this molecule, ~35 $cm^{-1}$).

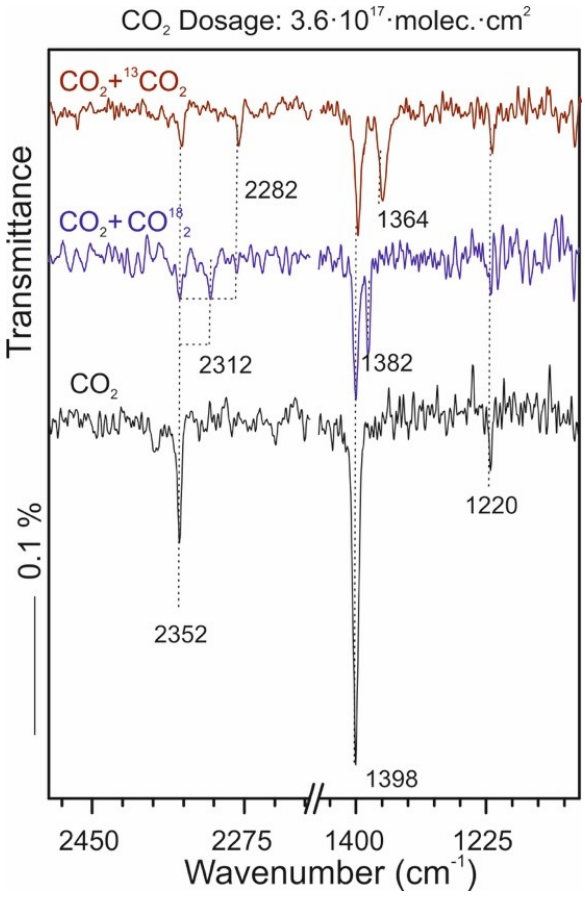


*Fig.6.4. Co-adsorption experiment of pure and isotopically labelled $CO_2$ to distinguish between monomers and dimers on the surface. The comparison between the co-adsorption of $^{13}CO_2$ and $CO_2$ (red), the co-adsorption of $CO^{18}{}_2$ and $CO_2$ (blue), and the pure $CO_2$ adsorption (black) is presented. The experiments are performed at 200 K with a $CO_2$ dosage of $3.6 \cdot 10^{17}$ molec.$\cdot cm^{-2}$.*

The same behavior can be observed when $CO_2$ and $O^{18}$-labelled $CO^{18}{}_2$ are co-adsorbed on the surface. Again, no shift but two separated peaks at 1398 $cm^{-1}$ and 1382 $cm^{-1}$ are observed. These experimental findings confirm that the considered peak is not the fingerprint of a dimer-species as, for example, oxalates. The assignment of these features has to be consistent with a monomeric-like adsorbate that has not been considered before. An answer to this open question was given by Wang X. et al[181] who studied the $CO_2$ activation on $Pd/Al_2O_3$ catalysts. They proposed the formation of bicarbonate-like species which are formed through reaction between $CO_2$ and OH groups present on the surface, stressing the role of the hydroxylation degree of the surface itself. Several considerations follow.

First, the peaks observed in the study presented in this work fall in the same range of frequencies which were assigned by Wang et al. to surface-bicarbonates[181]. Second, it was presented earlier in this chapter that $CO_2$ desorption spectra present at high coverage also considerable amounts of water desorption. Third, the sensitivity of the $Fe_3O_4$(111) towards residual gas adsorption (i.e. water)[140,158,72] has to be taken into account. Therefore, it seems reasonable to further investigate whether and how carbon dioxide and water adsorption on magnetite are linked to each other.

## 6.3 The Role of Water in the $CO_2$ Activation

To shed more light on the nature of the $CO_2$-chemisorbed species on the surface and on their relationship with water, a series of experiments were carried out dosing and co-dosing water as well as $D_2O$, and $CO_2$ on $Fe_3O_4$(111). The first experiment in this sense is illustrated in Fig. 6.5a and investigates the carbon dioxide behavior on a surface modified with OH-groups. Particularly, the magnetite surface was first pre-covered with $H_2O$ (dosage=$5.4 \cdot 10^{14}$ molec.$\cdot cm^{-2}$) at 200 K, and afterwards exposed to different amounts of $CO_2$ in the same temperature conditions. The comparison between the above described experiment and the adsorption of $CO_2$ on "clean" $Fe_3O_4$(111) is also shown in the Fig. 6.5a. It is clear that the presence of hydroxyl groups on the surface has a tremendous effect on the $CO_2$ chemisorption. Indeed, when the surface is covered in OH groups (evidenced by the two peaks at 3690 $cm^{-1}$ and 3640 $cm^{-1}$, widely discussed in Chapter 5), a big enhancement in the intensity of the peaks related to $CO_2$ is observed. Indeed, the peak centered at around 1389 $cm^{-1}$ increases in intensity to almost double, compared to when the same amount of $CO_2$ is adsorbed on the "clean" $Fe_3O_4$(111).

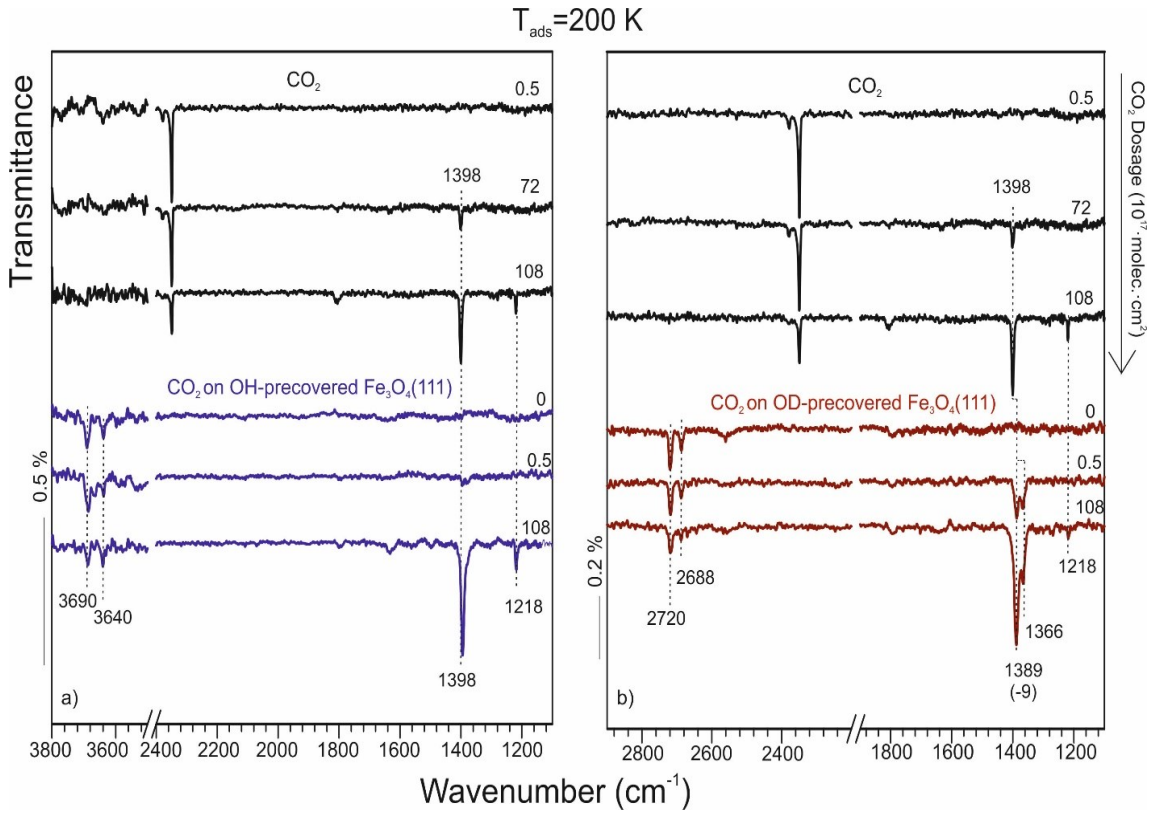


*Fig.6.5. Comparison between the $CO_2$ adsorption on regular (black) and OH-precovered (blue) $Fe_3O_4(111)$ surfaces (a). Comparison between the $CO_2$ adsorption on regular (black) and OD-precovered (red) $Fe_3O_4(111)$ surfaces (b). The $H_2O$ ($D_2O$) dosage on the surface is $5.4 \cdot 10^{14}$ molec.$\cdot cm^{-2}$.*

The above described experiment represents an already convincing evidence for the fact that OH groups act as trigger for the formation of the surface-bicarbonates-like species. The case where it is possible to observe these surface-species also without on-purpose exposition of the surface with water, can be addressed to the reactivity of $Fe_3O_4(111)$ surfaces towards water present in the background of the UHV chamber, which might simply not be detected in the IRA spectra because of the very low concentration and the reasons cited earlier (i.e., selection rules[179]). A conclusive experimental evidence for the bicarbonate-like species formation is given by the experiment depicted in Fig. 6.5b. Here, the adsorption of $CO_2$ on an OD-modified $Fe_3O_4(111)$ surface is studied. The idea behind this experiment is that if the surface species formation is somehow linked to the hydroxyl groups on the surface, upon reaction with OD the related peaks must undergo isotopic shift. Indeed, in an OD-rich surface (evidenced by the well-known IRA features at 2720 $cm^{-1}$ and 2686 $cm^{-1}$), not only a huge enhancement in

intensity of the peaks is observed, but also a shift of 9 $cm^{-1}$ and 6 $cm^{-1}$ for the peaks at 1398 $cm^{-1}$ and 1200 $cm^{-1}$ respectively. Furthermore, a new features at around 1366 $cm^{-1}$ growths up as a shoulder. The latter findings suggest that the water on the surface (as traces from residual gases or adsorbed on purpose) plays a crucial role in the $CO_2$ activation at 200 K, leading to the formation of chemisorbed species consistent with surface-bicarbonates. Now that it is clear that there is a strong relation between water on the surface and carbon dioxide chemisorption, it is of great interest to understand which kind of dependence is established. The first experiment that was performed in this sense is shown in Fig. 6.6. Here, the surface is first modified with a fixed amount of $D_2O$ ($2.6 \cdot 10^{14}$molec.$\cdot cm^{-2}$, light blue spectrum) and afterwards exposed to two different $CO_2$ dosages ($2.7 \cdot 10^{15}$molec.$\cdot cm^{-2}$ and $7.2 \cdot 10^{17}$molec.$\cdot cm^{-2}$, red and yellow spectra respectively). The figure clearly exemplifies the trend of the water related species upon interaction with carbon dioxide. Indeed, the intensity of the OD-species decreases as the intensity of the surface-bircabonates features increases. This observation provides a strong evidence of the relation between the two species on the surface: bicarbonate formation consumes hydroxyl groups.

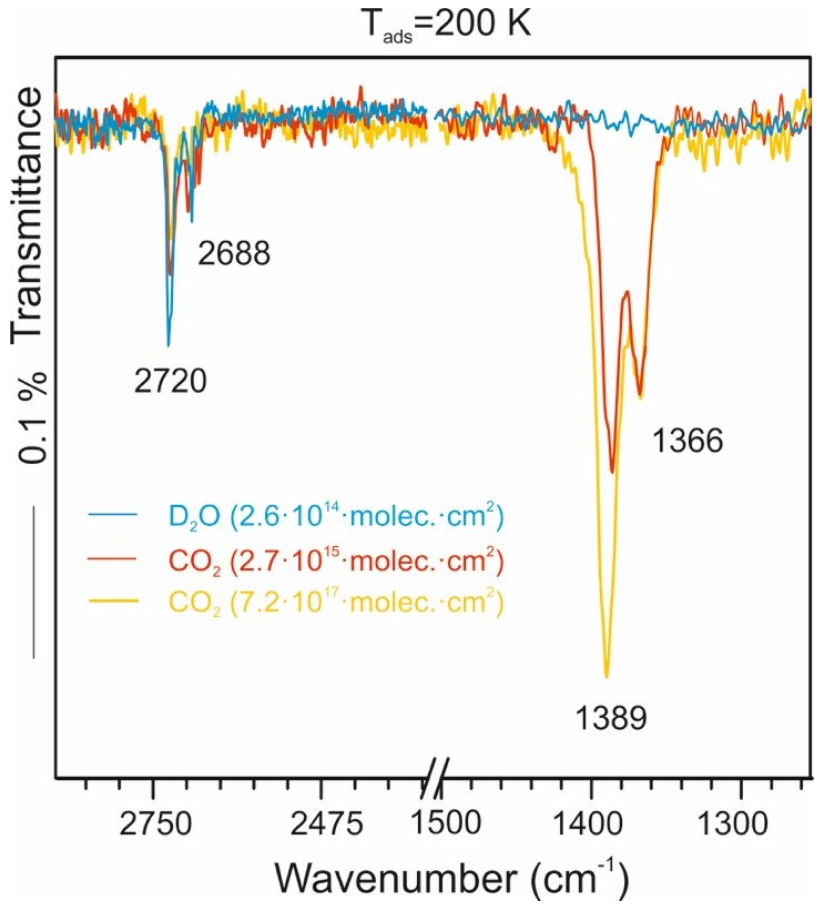


*Fig.6.6. Series of IRA spectra showing the comparison between the pure $D_2O$ adsorption ($2.6 \cdot 10^{14}$molec.·cm$^{-2}$) on $Fe_3O_4$(111) (light blue); how the water-related peaks are affected upon interaction with different amounts of $CO_2$, $2.7 \cdot 10^{15}$molec.·cm$^{-2}$ and $7.2 \cdot 10^{17}$molec.·cm$^{-2}$, illustrated in red and yellow respectively.*

Further insight is given by the study of the behavior of $CO_2$ with respect to different amounts of OD species used for pre-covering the magnetite surface. This experiment, illustrated in Fig. 6.7, shows that presence and concentration of surface-bicarbonates strongly depends on the extent of the hydroxylation degree of the surface. Indeed, when $CO_2$ is adsorbed on magnetite previously modified by a relatively small amount of OD groups a strong surface-bicarbonate related peak at 1389 cm$^{-1}$ is detected. When the OD concentration increases, the second peak around 1366 cm$^{-1}$, which at the beginning develops as a tiny shoulder, gains considerably intensity. However, when the water coverage is high enough allowing it to self-assemble on the surface in the known 2D network (see in the IRA spectrum the development of several sharp features and the broad signature for the molecular water), no peak related to $CO_2$ chemisorption

can be detected. What is shown is a clear evidence that above a critical concentration of $D_2O$, surface-bicarbonates cannot form, meaning that $CO_2$-adsorbates and $D_2O$ are in competition for the same adsorption sites. Accessibility of the "free" OD-Fe on the surface is necessary for the formation of $CO_2$ adsorbates on the $Fe_3O_4$(111), and high ODs concentration passivates the surface. Before the concluding remarks, something else needs to be pointed out. Fig. 6.7 also shows that, upon interaction with $CO_2$, the intensity ratio of the water-related features changes, in comparison with pure $D_2O$ adsorption on $Fe_3O_4$(111). Hence, when the surface-bicarbonates are formed the two water peaks decrease in intensity asymmetrically. It was widely discussed in Chapter 5 that the two mentioned peaks do not belong to the same OD but to a terminal $O_w$D-Fe (on top of a Fe cation) and $O_s$D involving oxygen from the surface lattice. Therefore, it might be possible that different types of bicarbonates are being formed on the surface upon selective interaction with different OD species. This is just a hypothesis, but it can serve as a benchmark for theoretical calculations.

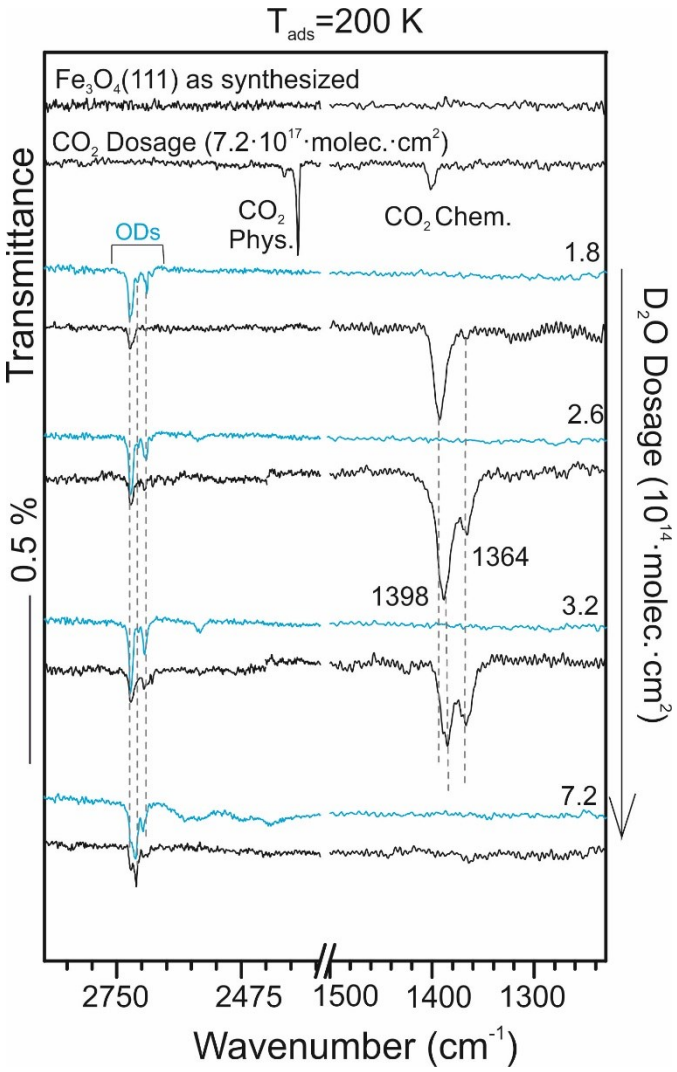


*Fig.6.7. Series of IRA spectra related to the adsorption of $CO_2$ ($7.2 \cdot 10^{17}$ molec.·$cm^{-2}$) on $Fe_3O_4$(111) surfaces pre-covered with different amounts of OD species (black). For comparison, also the adsorption of pure $D_2O$ on the clean magnetite surface is shown (light blue). The experiments are performed at 200 K.*

## 6.4 Conclusions

A detailed study of the carbon dioxide behavior when adsorbed on magnetite (111) surface at different dosages and temperatures conditions was presented in this work. The $CO_2$ adsorption on $Fe_3O_4$(111) was investigated by means of IRAS as function of coverage and the following scenario is proposed. IRA spectra show mainly contribution from $CO_2$-physisorbed in the range of temperatures between 120 K and 140K, although some features associated with chemisorption are also observed. However, the formation of the chemisorbed species requires relatively high $CO_2$

exposures on the surface, meaning that a certain degree of modification of the surface itself has to occur in order to observe chemisorption. This finding suggests that the formation of such chemisorbed species detected in the IRA spectra is driven by the presence of surface imperfections[175,182]. Nevertheless, experiments performed with regular and $^{13}C$- and $O^{18}$-labelled $CO_2$, allowed the assignment of the IRA features observed in the above-mentioned range of temperatures (120-140 K), and consistency with intermediates such as carboxylates and carbonates have been found. At higher temperatures (~200-240 K) considerably stronger adsorbed features develop in the IRA spectra. In these conditions it cannot be excluded that the $Fe_3O_4$(111) surface is not clean, but contains traces of water due to its sensitivity towards residual gas adsorption[140,158,72]. The correlation between $CO_2$ and water was then in more details investigated with infrared experiments, performed using regular as well as labelled water, to pre-cover the surface before $CO_2$ adsorption. It was found that the degree of hydroxylation of the surface plays a crucial role in the $CO_2$ activation on regular $Fe_{tet1}$-magnetite, leading to the formation of bicarbonate-like species.

Certainly, IRAS alone is not sufficient to provide a unified picture and, therefore, further experiments as well as DFT calculations, must be performed.

# 7. Comparison between $Fe_3O_4$(111) and $Fe_3O_4$(100) Surfaces

## 7.1 Introduction

The work presented in the last chapters has shown that surface properties of magnetite are of tremendous interest in both catalysis and material science[183,184,185,15]. Indeed, magnetite being ubiquitous in nature and also reactive towards several chemicals has a potential use as a cheap heterogeneous catalyst[186,187,188,189,19]. Since most of the ambient temperature chemical reactions involving magnetite in natural systems occur in presence of aqueous solutions, the understanding of how the surface and its electronic properties are affected when modified by water is of high relevance. In this sense, iron oxide catalysts are already successfully used in the water-gas shift reaction (WGSR) [19,20], a process of extremely high impact in technology, since it necessarily accompanies outstanding large-scale industries as ammonia and methanol synthesis and is furthermore needed for fuel cells applications[190,191]. In particular, in the literature it is reported that the heterogeneously catalyzed water-gas shift reaction can be regulated by two main reaction mechanisms, the so-called associative and redox mechanism[20,190]. In the first one, water and $CO_2$ interact on the surface forming intermediate-complexes on the basis of the Langmuir–Hinshelwood kinetics (see Chapter 2, Section 2.1). In the second mechanism, the metal oxide surface is alternatively reduced and oxidized by CO and water respectively, following the Mars-van-Krevelen[192] reaction pathway. It is commonly believed that, in both cases, the WGSR is driven by surface hydroxyl groups: this makes the adsorption of water on the magnetite surface one of the most important elementary steps in the reaction[193].

Although most of the literature concerning water and $CO_2$ adsorption studies on magnetite is related to the closed-packed $Fe_3O_4$(111), more work has recently been focused also on the $Fe_3O_4$(100), expecting different reactivity from the two surfaces[21]. With respect to an atomic-level understanding of the structure of the outermost surface layers, recent combined studies using scanning tunneling microscopy (STM), low energy electron diffraction (LEED), and density functional theory (DFT) on the (001) facet gave firm evidence for a resolved surface structure[60]. In this study, Bliem et. al. showed that an ordered array of subsurface cation vacancy (SVC) and interstitials is

responsible for the well-known $(\sqrt{2} \times \sqrt{2})R45^{\circ}$ reconstruction of $Fe_3O_4$(100). On the contrary, the surface structure of the (111) facet has been under debate for almost twenty years. As explained in details in Chapter 4, one of the achievement of this work was indeed to shed light on the $Fe_3O_4$(111) surface structure, eliminating any discrepancy in favor of the single metal $Fe_{tet1}$-termination of the $Fe_3O_4$(111) surface[140].

The reactivity of the two stable facets, (111)- and (100)- $Fe_3O_4$, towards water and $CO_2$ have been studied in the last years by several surface sensitive techniques and a short summary of the state of knowledge up-to-date follows.

*Water adsorption on magnetite.* Experiments performed from Cutting et al. and Kendelewicz et al. on magnetite single crystals by means of photoelectron spectroscopy showed that on both (111) and (100) surfaces, the formation of hydroxyl groups is favored at higher coverages with a sharp pressure dependence[65,66]. With respect to the $Fe_3O_4$(111) surface, the reactivity of the surface towards water has been found to be very sensitive to the surface termination (a wide and detailed discussion can be found in the Chapter 5 of this work). Indeed, water dissociates on regular $Fe_{tet1}$-terminated surface giving rise of terminal $O_wH$ on top of Fe cation and $O_sH$ groups involving oxygen atoms from the surface[67,70,158], whereas on $Fe_{oct2}$-terminated surface it is more likely to form a complex consisting of a half dissociated dimer from the onset[51]. On the (100) facet, water adsorption was studied by means of TPD, XPS, AFM and DFT[163,188]. In particular, the group of G. Parkinson proposed that water splits on the $Fe_3O_4$(100) surface at room temperature, resulting in the hydrogenation of the oxygen lattice; the heating of such surface results in the extraction of lattice oxygen atoms to form water molecules, leading to a reduction of the $Fe_3O_4$(100) under UHV conditions[188]. A very recent study from the same group suggests the formation of partially-dissociated water agglomerates (partially dissociated dimers and trimers) at higher coverage, driven by progressive formation of intermolecular hydrogen bonds, also favored by the presence of neighbor under-coordinated cations[163]. The presence of the subsurface cation vacancies (SCV) reconstruction[60] seems to be responsible for the limited concentration of surface O (one/unit cell) that can accept a proton. The partially dissociated species formed on the surface, act as anchor to build an H-bonded architecture before saturation occurs.

*$CO_2$ adsorption on magnetite.* Concerning the $CO_2$ adsorption on magnetite, the amount of investigations conducted until now is scarce. Earlier in this work, it was presented the first - to the best of our knowledge - adsorption study of carbon dioxide on $Fe_3O_4$(111) as function of coverage and surface temperatures. Experimental evidences show that at lower temperatures (120-150 K) magnetite, in the (111) orientation, is rather inert towards carbon dioxide chemisorption and the formation of species associated with carbonates and carboxylates is likely driven by the presence of surface imperfections. On the other hand, at temperatures in the range 200-240 K, OH groups present on the surfaces lead to the formation of bicarbonate-like species. These observations are in good agreement with the only example found in literature on the adsorption of carbon dioxide on the (100) magnetite surface[175]. The latter, based on TPD, UPS and STM experiments and DFT calculations, suggests that, in its initial stage, $CO_2$ strongly adsorbs on $Fe^{2+}$-surface defects, to form then a monolayer of molecules which are physisorbed on the regular surface ($Fe^{3+}$-sites).

According to what was exposed so far, a parallel study of the adsorption properties of the two surfaces seems essential. In this chapter, preliminary data on the adsorption of water and $CO_2$ on $Fe_3O_4$(100) surfaces is presented. The experiments are performed with the same molecular beam-IRAS experimental setup described in Chapter 3, to allow a direct comparison with the adsorption studies performed on $Fe_3O_4$(111) surfaces, previously discussed in detail in Chapter 5 and 6, respectively. The $Fe_3O_4$(100) surface was prepared following the recipe employed by Davis et al.[21]

## 7.2 Water Adsorption on $Fe_3O_4$(100)

The reactivity of $Fe_3O_4$(100) towards water was investigated performing adsorption experiments of $D_2O$ on the surface at several temperatures and recording the IRA spectra as function of coverage. The adsorption temperatures were chosen on the basis of a very recent TPD experiment of water on $Fe_3O_4$(100), published in the study of Meier et al[163]. In this work, seven desorption peaks have been identified and four of them (at ~155 K, 190 K, 215 K, 230 K) have been considered as related to species adsorbed on the regular surface and constituent of the first water monolayer, and have been in detail characterized[163]. Therefore, it seemed reasonable to start our IRAS investigation with the surface temperatures on the edge of the desorption peaks. Figure 7.1 shows a series of selected IRA spectra of $D_2O$ adsorbed $Fe_3O_4$(100) at 165 K, 200 K and 225 K. The aforementioned temperatures represent the most meaningful ones for this experiment. Indeed, saturation of the surface is already observed at 225 K in the low water coverage regime, and no infrared-signal is detected above this temperature. On the other hand, in the higher coverage regime, ice formation is already observed after high dosage of water at 165 K.

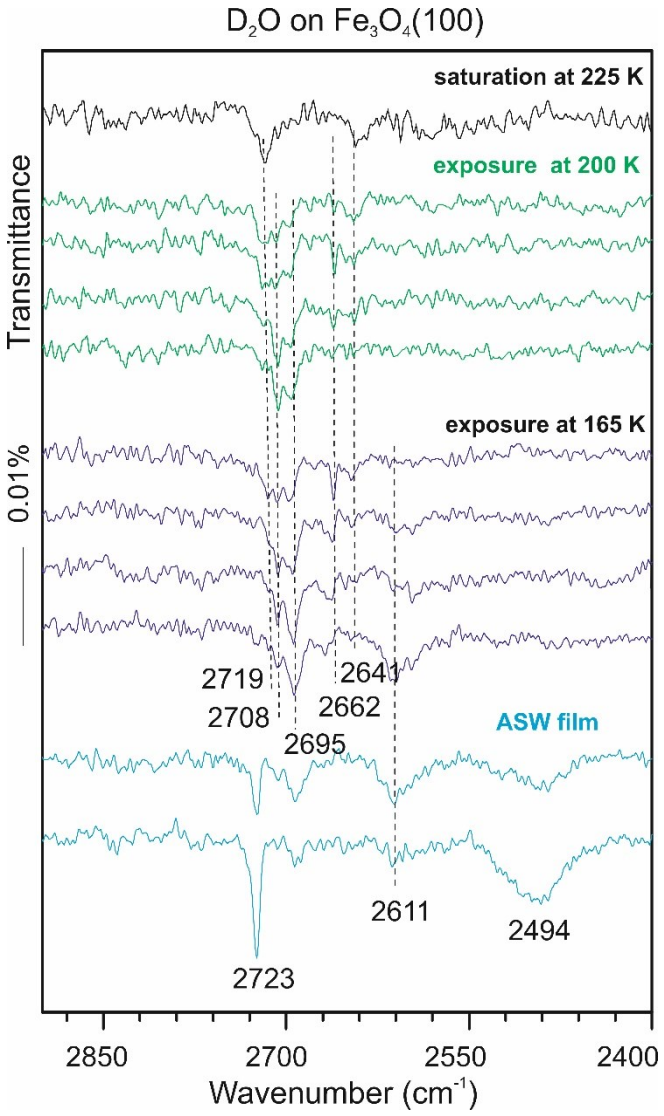


*Fig.7.1. Series of selected spectra showing the IRA-features evolution as a function of coverage when $D_2O$ is adsorbed on $Fe_3O_4$ (100) at 225 K, 200 K, and 165 K respectively. Each water pulse corresponds to a dosage of $6 \cdot 10^{13} \cdot molec. \cdot cm^{-1}$.*

The spectra evolution can be discussed as follows. At 225 K, two broad adsorption features with a center of gravity at around 2719 $cm^{-1}$ and 2642 $cm^{-1}$ can be observed. These two features are already saturated after the first $D_2O$ pulse on the surface. As the coverage increases ($T_{asd}$ = 200 K) new features appear and the overall picture becomes more complex.

The peak at 2719 $cm^{-1}$ decreases in intensity, while a new band at 2708 $cm^{-1}$ starts growing in parallel with another feature centered at 2695 $cm^{-1}$ which appears as a shoulder. In the lower frequencies side of the spectrum, it seems that the band at 2642

$cm^{-1}$, previously observed at higher temperature, survives only for low water dosages and then disappears, whereas a new feature at 2662 $cm^{-1}$ starts grow. At 165 K, the 2719 $cm^{-1}$ peak is no longer visible, and the intensity ratio between the peaks at 2708 $cm^{-1}$ and at 2695 $cm^{-1}$ changes, showing the latter peak with the highest intensity. On the other hand, the lower frequency peak at 2662 $cm^{-1}$ grows and undergoes blue shift. Also, a new broad feature centered at around 2495 $cm^{-1}$ appears. At high water dosage saturation is reached with the formation of ice (ASW), characterized by the sharp peak at 2723 $cm^{-1}$ and the broad one at 2493 $cm^{-1}$, typical for stretching vibrations of dangling OD species at the surface and D-bonded OD in water clusters respectively.

To be able to interpret the spectra evolution and then compare the water behavior on the (100) surface with the one on the (111), the help of isotopic labelling is required. In particular, $D_2O$ was exposed on a magnetite film prepared using $O^{18}$, and the results of this experiment were then compared with the one obtained for water adsorption on regular $Fe_3O_4$(100). Fig. 7.2 shows the above-mentioned experiment when $D_2O$ is adsorbed on $Fe_3O^{18}{}_4$(100) at 225 K.

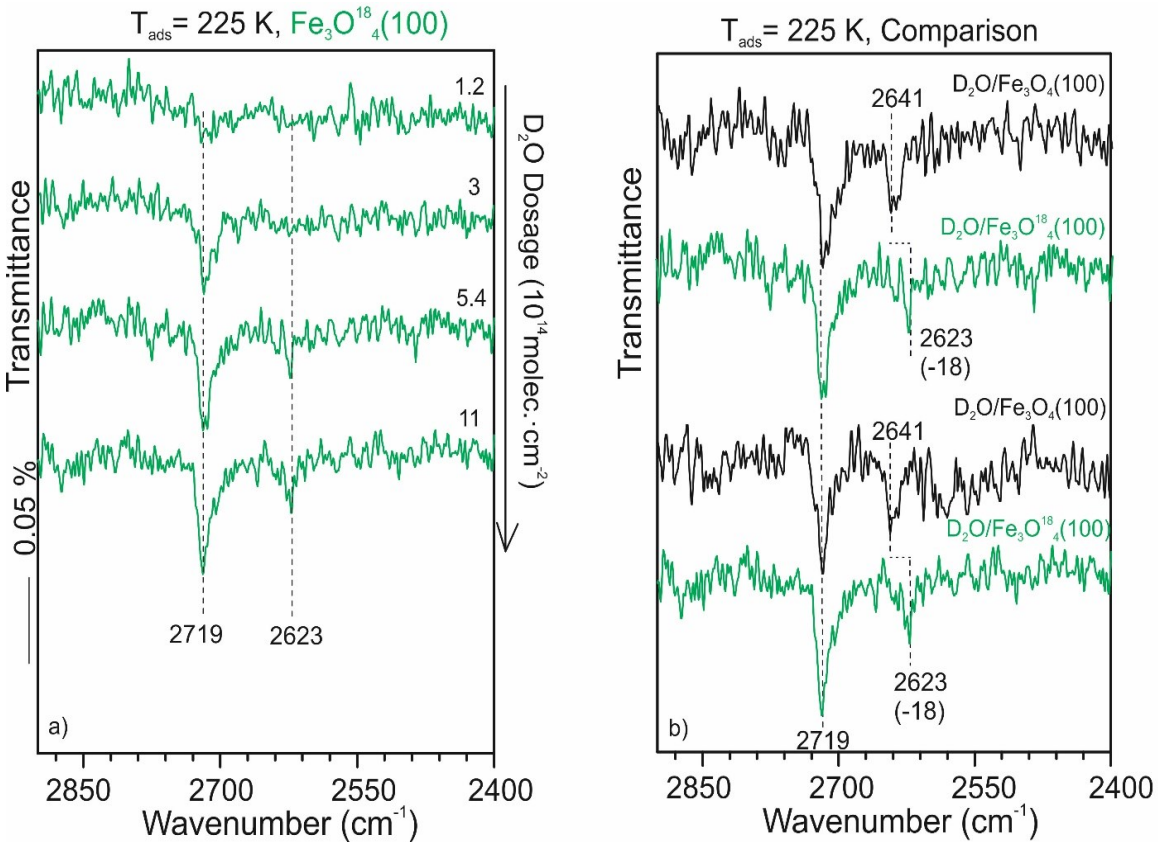


*Fig.7.2. IRA spectra of $D_2O$ adsorbed on $O^{18}$-labelled $Fe_3O^{18}{}_4(100)$ as function of coverage at 225 K (a). Comparison of the IRA features of $D_2O$ adsorbed on regular $Fe_3O_4$ (100) (black spectra) and on $O^{18}$-labelled $Fe_3O^{18}{}_4(100)$ (green spectra) (b) The figure shows the isotopic shifts due to the $O_sD$ involving a surface oxygen.*

The Fig.7.2b clearly shows that, upon $O^{18}$-labelling in the magnetite film, the band centered at 2641 $cm^{-1}$ shifts of about 18 $cm^{-1}$. This represents a strong evidence of the fact that the band at around 2719 $cm^{-1}$ must be associated with terminal Fe-$O_wD$, whereas the one at 2641 $cm^{-1}$ is due to surface hydroxyl groups ($O_sD$). As previously showed in the Fig.5.4 in Chapter 5 in the case of water adsorbed on $Fe_3O_4$(111), also in the case of the $Fe_3O_4$(100) such experiment allows a first conclusion about the water adsorption in the low coverage regime. Hence, the initial stage of the adsorption process involves water dissociation in a terminal Fe-$O_wD$ and an $O_sD$. Interestingly, the isotopic shift observed in this case is very similar to the one observed for the (111) surface (18 $cm^{-1}$ vs 17 $cm^{-1}$). However, the Fig.7.2 also shows that on this surface the OD-related IRA features are significantly small (and also smaller than the same bands observed in the low coverage regime on the (111) surface).

The low coverage conditions as well as the quite low signal-to-noise ratio, suggest that these features might form on defect sites. This hypothesis is supported by the temperature programmed desorption experiments showed in Fig. 7.3. Hence, the desorption profile of water adsorbed at 225 K on the $Fe_3O_4$(100) surface (blue curve), appears to involve only minority species which are, therefore, not considered as adsorption on regular sites. On the contrary, the figure shows desorption profiles obtained after water adsorbed at 200 K (red curve) and at 165 K (black curve), which seem to be consistent with adsorption on the regular surface. This finding is in well agreement with the results reported in Ref.[163]

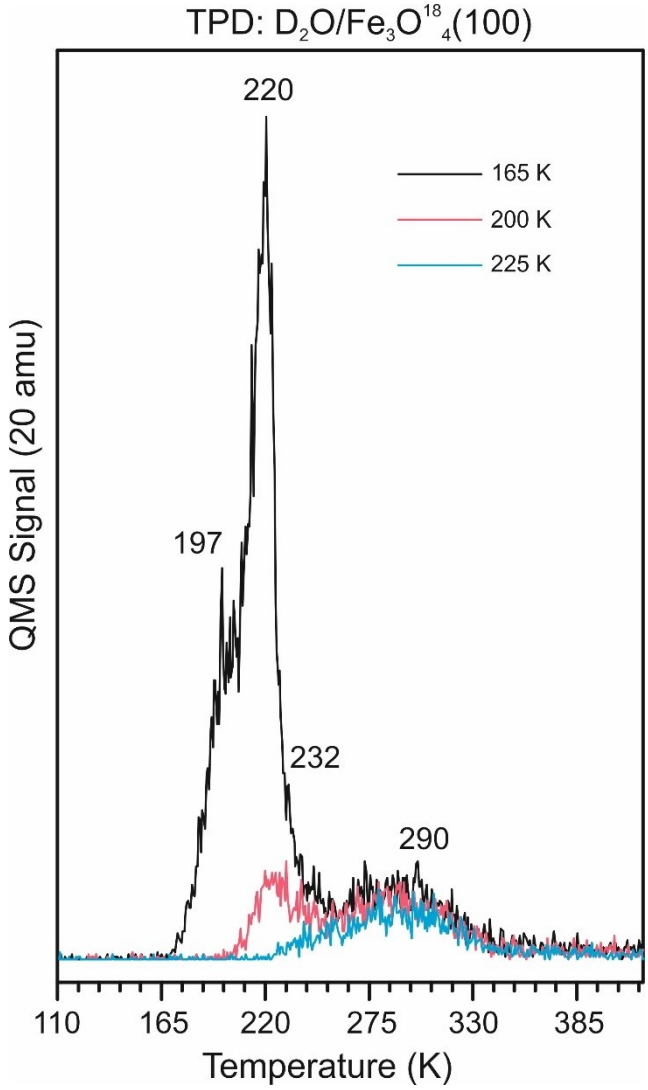


*Fig. 7.3. TPD spectra measured after IRAS experiments performed at 165 K (black line), 200 K (pink line) and 225 K (light blue line). The heating rate is 3 K/s. The observed desorption profiles are in very well agreement with the one presented in the study of Meier et al.*[163] *The lower resolution can be related to the absence of differential pumping stages in the mass spectrometer.*

Figure 7.4 shows the IRA features for $D_2O$ adsorbed on $Fe_3O^{18}{}_4(100)$ at 200 K as function of coverage (a), and also their comparison with the signals observed for the adsorption on a regular magnetite film (b).

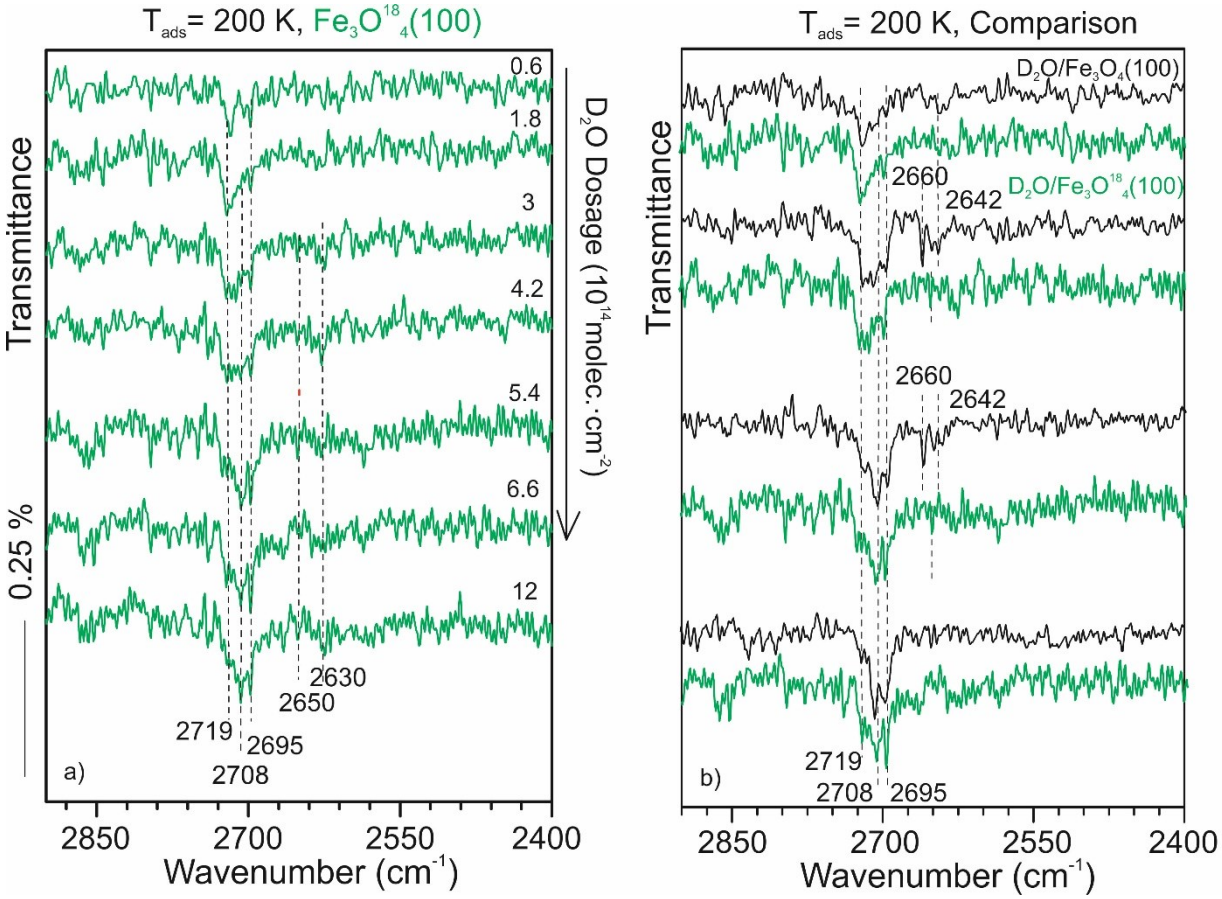


*Fig.7.4. IRA spectra of $D_2O$ adsorbed on $O^{18}$-labelled $Fe_3O^{18}{}_4(100)$ as function of coverage at 200 K (a). Comparison of the IRA features of $D_2O$ adsorbed on regular $Fe_3O_4$ (100) (black spectra) and on $O^{18}$-labelled $Fe_3O^{18}{}_4(100)$ (green spectra) (b).*

This experiment displays a peaks evolution virtually identical to the one detected in the case of water adsorption on a regular on $Fe_3O_4(100)$. The features at 2719 $cm^{-1}$, 2708 $cm^{-1}$ and 2695 $cm^{-1}$ do not shift upon $O^{18}$-labelling of the surface, suggesting that -at this coverage- molecular water adsorption dominates. On the other hand, two new small bands can be identified at around 2650 $cm^{-1}$ and 2630 $cm^{-1}$. Nevertheless, even if these bands are somehow red shifted if compared with the features at 2660 $cm^{-1}$ and 2642 $cm^{-1}$ on the regular $Fe_3O_4(100)$, their size is as small as the noise and they also

disappear after few pulses, indicating that most likely surface diffusion and surface heterogeneity must be taken into account. Hence, in this experiment no significant isotopic shift is observed. It might be, then, concluded that water adsorption on regular surface sites at 200 K occurs molecularly. This is in quite good agreement with what was recently proposed by Meier et al.[163], who calculated that the most stable configuration of water on the $Fe_3O_4$(100) surface involves the formation of a partially dissociated water dimer ($E_{ads}$ = -92 eV/molecule). However, the difference in the adsorption energy for molecular ($E_{ads}$ = -0.64 eV) and dissociative adsorption ($E_{ads}$ = -0.59 eV) of water on the surface is quite small, therefore some mixture might be observed in equilibrium at finite temperatures[163,194]. The partially-dissociated water dimers may then anchor further new water molecules to form bigger oligomers. Accordingly, adsorption of water at high coverage on $O^{18}$-labelled magnetite films was investigated. This experiment is shown in Fig 7.5, where the IRA features for $D_2O$ adsorbed on $Fe_3O^{18}{}_4$(100) at 165 K as function of coverage (a), and also their comparison with what observed for the regular magnetite film (b), are displayed.

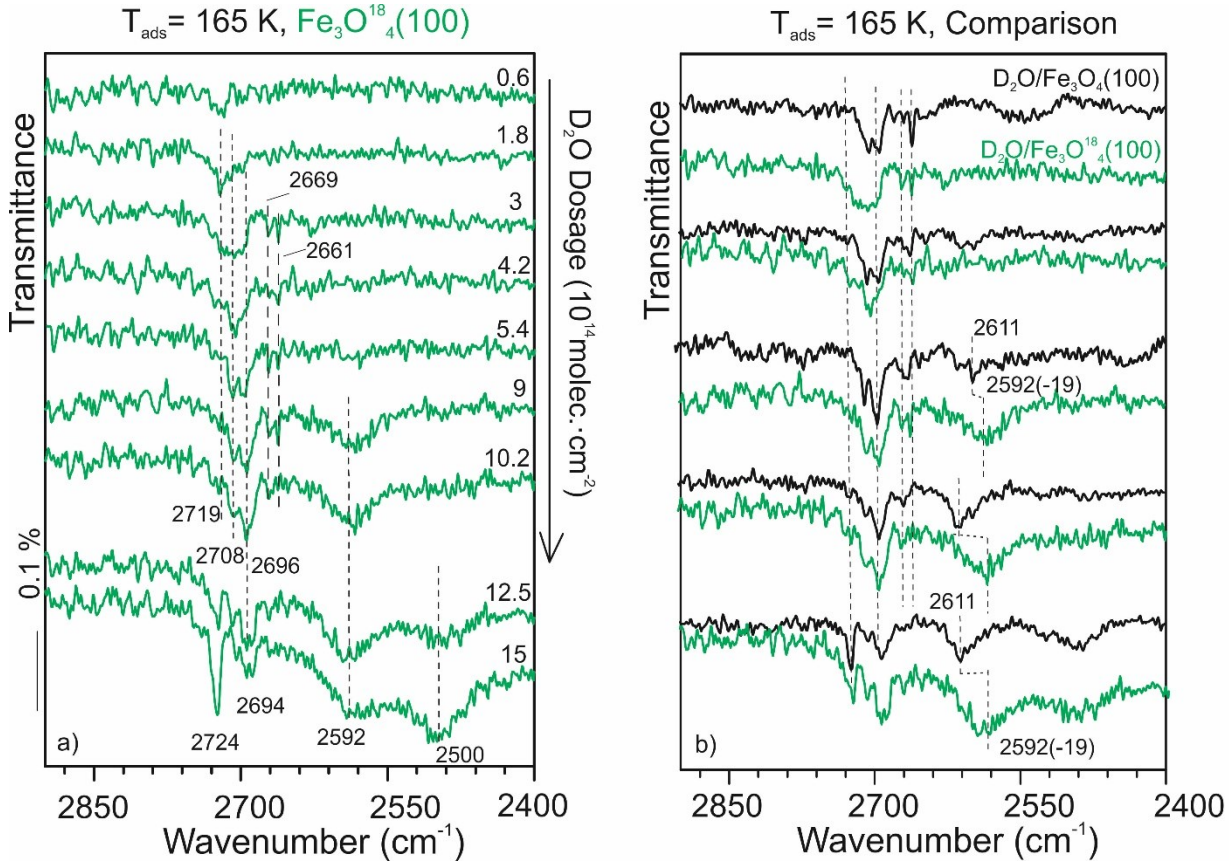


*Fig.7.5. IRA spectra of $D_2O$ adsorbed on $O^{18}$-labelled $Fe_3O^{18}{}_4(100)$ as function of coverage at 165 K (a). Comparison of the IRA features of $D_2O$ adsorbed on regular $Fe_3O_4$ (100) (black spectra) and on $O^{18}$-labelled $Fe_3O^{18}{}_4(100)$ (green spectra) (b).*

In the high coverage regime, the spectra in the 2720-2695 $cm^{-1}$ range follow the same evolution as for the adsorption at 200 K. In the lower frequency region, the picture is less straightforward. Hence, at higher dosage and prior the amorphous solid water formation, a broad band centered in the regular film at ~2611 $cm^{-1}$ starts growing and shifts of about 19 $cm^{-1}$ upon water adsorption on $O^{18}$-labelled $Fe_3O^{18}{}_4(100)$. The isotopic shift clear indicates that this band, despite its width and frequency, is not related to the ASW formation, but it involves indeed surface hydroxyls ($O_sD$). An explanation for this may be found in the already mentioned study from Maier et al. This work proposes that half dissociated water dimers on the surface bind further molecules coming on the surface at increasing coverage, giving rise of partially dissociated water trimers[24]. The geometry of these stable oligomers, calculated with density functional theory and observed experimentally with non-contact AFM measurements, is shown in Fig. 7.6.

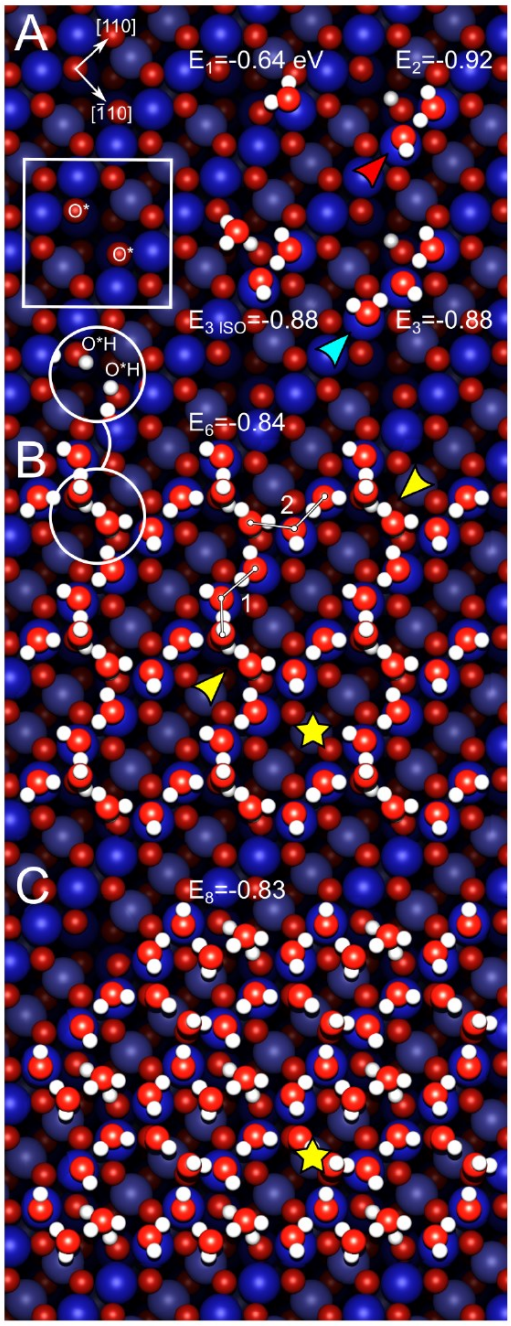


*Fig.7.6. Top view of the minimum-energy structures for water adsorbed on $Fe_3O_4$(100) sufaces calculated by DFT. (A) shows that an isolated water molecule adsorbed intact is less energetically preferred than the formation of dimers and trimers. The two isoenergetic geometries for trimers are also shown. (B) and (C) show a ring-like structure and a more complex one using dangling bonds, typically observed at very high water coverages.*

*This model is proposed by Meier, M., Hulva, J., Jakub, Z., Pavelec, J., Setvin, M., Bliem, R., Schmid, M., Diebold, U., Franchini, C., and Parkinson, G.* [163]

It consists of a linear $D_2O$-OD-$D_2O$ configuration, where the third molecule binds on the surface $Fe_{oct}$ row and donates an H-bond into the OD. According to this picture, it might be possible to detect $O_sD$ involving surface oxygen and that might explain the isotopic shift in the IRA features upon $O^{18}$-labelling of the film.
Increasing the water dosage leads to water molecules chains and ring like structures (as shown in Fig. 7.6 in the calculated structures), and – finally - to the ice layer formation, displayed in the IRA spectra by the characteristic sharp peak at 2724 $cm^{-1}$ and the broad band centered at 2500 $cm^{-1}$.

Based on the experimental observation, it is possible to conclude that the water behavior on the (100) facet of magnetite is similar but non-identical to one on the (111) surface. Indeed, IRA measurements of water adsorption at 165 K, hence suggesting adsorption also on the regular sites, first revealed no surface hydroxyls (beyond those on defects), indicating that molecular adsorption dominates at low coverages. Only at relatively high coverages and up to the point when amorphous solid water starts to form, surface hydroxyls are observed, thus reflecting the formation of half-dissociated dimers and other linear oligomers (most likely half dissociated water trimers), which ultimately form a hydrogen bonding network in which surface hydroxyls "survive" in the structure.

The scenario proposed with the presented infrared data is of course still preliminary and DFT calculations for a more detailed assignment of the IRA features will be performed in the near future.

### 7.3 $CO_2$ Adsorption on $Fe_3O_4(100)$

The adsorption of $CO_2$ was investigated with IRAS on the $Fe_3O_4(100)$ surface as a function of coverage first at 200 K. The reason for choosing this temperature relies on the fact that it allows a more straightforward comparison with the results obtained for the $Fe_3O_4(111)$ surface; spectra at this temperature are easier to interpret than such from lower temperatures, where a more complex peak evolution occurs.

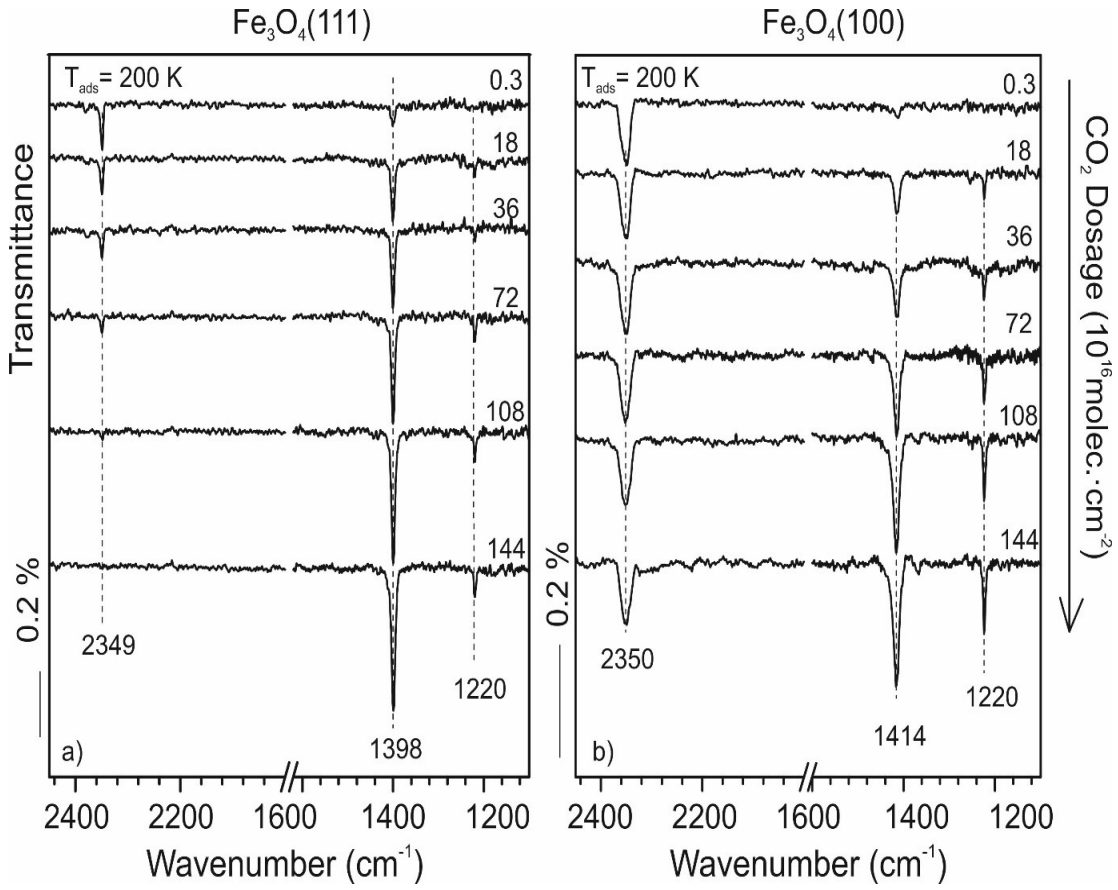


*Fig.7.5. Series of IRA spectra showing the comparison between the $CO_2$ adsorption on $Fe_3O_4(111)$ and $Fe_3O_4(100)$, in (a) and (b) respectively, at 200 K and as a function of $CO_2$ exposure.*

Figure 7.5b shows our first IRA results of the $CO_2$ adsorption on a $Fe_3O_4(100)$, kept at 200 K. In comparison with the adsorption experiment on the (111) surface (Fig. 7.5a), the following considerations can be done. First, as in the case of the (111) orientation, two main chemisorbed species are detected, having frequencies centered at around 1414 $cm^{-1}$ and 1220 $cm^{-1}$, which are very similar to the one observed on the

(111)-oriented surface and, therefore, also in the range of bicarbonate-like species. This surface seems to be less reactive towards $CO_2$, since the intensity of the above-mentioned peaks is rather small compared to what is found in the case of $Fe_3O_4$(111). Second, the peak related to physisorbed $CO_2$, centered at around 2350 $cm^{-1}$, is higher in intensity, – in comparison with the one on $Fe_3O_4$(111), and also does not disappear at increasing exposure. This finding is in good agreement with what was proposed by Pavelec et al.[175], who found that the $CO_2$ adsorbs first on defects-related sites, and afterwards forms a physorbed monolayer on the regular surface. Indeed, LEED and STM studies of the $Fe_3O_4$(100)-$(\sqrt{2}x\sqrt{2})$R45° surface (in both cases of single crystals and thin films) showed a uniform, atomically flat and almost defects-free surface[15,21].

## 7.4 Preliminary Conclusions

The experiments shown in this Chapter are the first step towards a better understanding of the different adsorption properties of the (111)- and (100)- oriented surfaces.

According to the preliminary experimental evidences, the reactivity of the $Fe_3O_4$(100) towards water and $CO_2$ seems to be similar to the one of the (111) facet, but not exactly the same. The very early stage of the water adsorption process has been found to be a splitting of the water molecule, likely involving defects sites on both surfaces. In the case of the (100) facet though, water seems to prefer a partially dissociated dimer configuration on the regular sites even at low coverage, whereas strong experimental evidences have been presented to demonstrate the water dissociation on the (111) surface also in the regular sites prior more complex oligomer formation (Chapter 5). The partially dissociated water dimers act as an anchor for further molecules coming on the (100) surface, leading to the formation of partially dissociated water trimer. On both surfaces dimers and further oligomers assemble into a hydrogen bonding structure before the amorphous solid water is formed.

Carbon dioxide adsorption also involves at first surface imperfection. On both surfaces, evidences for water-induced bicarbonate species have been found, indicating the that water presence (induced or from residual gas adsorption) plays a key role on the $CO_2$ chemisorption on magnetite.

For both molecules, the IRA signals have been found to be smaller in intensity for the (100) surface than for the (111). This might be essentially related to a lower affinity of the $Fe_3O_4$(100) surface towards water and $CO_2$ chemisorption, compared to the $Fe_3O_4$(111). However, as widely explained in the Section 3.3.2 of Chapter 3, several and sometimes unpredictable factors affect the intensity of the IRAS signals, which make a quantitative analysis based only on the peak intensity and area difficult.

# 8. Summary

Understanding the fundamentals which govern adsorption and activation processes of water and $CO_2$ on metal oxide is one of the main achievements in catalytic research. The ubiquity of these two molecules in the ambient environment renders their interaction with solid surfaces of tremendous interest. However, determining their structure upon adsorption on solid surfaces seems to be rather challenging from both experimental and theoretical point of view. In this work, infrared-reflection-adsorption spectroscopy, with the support of temperature programmed desorption and also density functional theoretical calculations, was employed to investigate the catalytic activity of magnetite surfaces towards water and $CO_2$ adsorption. The combination of these powerful techniques with well-defined model substrates allowed the understanding of structure-activity relationships.

The first step in this direction was the preparation of a well-ordered $Fe_3O_4(111)$ film epitaxially grown onto Pt(111) single crystal and its characterization. The characterization of the surface termination of $Fe_3O_4(111)$ is crucial in the elucidation of its adsorption properties. Hence, although this surface has been investigated for more than twenty years, significant controversy remains in literature concerning the thermodynamically most favored surface termination. In the past, LEED experiments combined with LEED I/V and STM studies, suggested a bulk termination at the $Fe_{tet1}$ plane with a 1/4 monolayer of tetrahedrally coordinated $Fe^{3+}$ ions over a close-packed oxygen layer. However, former adsorption studies of CO and water on the magnetite surface invoked the octahedrally terminated surface $Fe_{oct2}$ to rationalize the experimental data. The main origin for this controversy may be found in the fact that multiple terminations can coexist, and they are strongly sensitive to the growth conditions and also to the sample history. In this work, CO was used as probe molecule to shed light on the $Fe_3O_4(111)$ surface termination question because its adsorption properties may be directly correlated to the surface structure of the metal oxide. In particular, a CO adsorption study using IRAS and TPD techniques, corroborated by DFT calculations, ruled out the presence of octahedrally coordinated iron ions ($Fe_{oct2}$) on the regular surface, suggesting the $Fe_{tet1}$-terminated surface as the most stable.

The core of this thesis is the study of the fundamental stages in the adsorption of water and $CO_2$ on a well-defined thetrahedrally terminated $Fe_3O_4(111)$ surface.

The understanding of the initial stage of water adsorption and dissociation is a notoriously challenging task and a certain disagreement can be found in the literature, mainly related to the difficulties of preparing well-defined, uniform and clean surfaces. Indeed, the first established model for the water adsorption on $Fe_3O_4(111)$ was based on the water dissociation on a $Fe_{tet1}$-terminated surface, giving rise to two hydroxo-species, $O_wH$-Fe and $O_sH$-(where $O_w$ and $O_s$ indicate oxygen atoms in water and on the oxide surface, respectively). A more recent study diverges with this picture, suggesting that water spontaneously assembles in a complex formed by dissociated and non-dissociated molecules, known as "half-dissociated dimer", on a $Fe_{oct2}$-terminated surface. Once again, the role of the surface termination seems to be crucial for the interpretation of the experimental data. In this work, based on the fact that - according to the $Fe_3O_4(111)$ surface preparation protocol proposed in Chapter 4- the most stable surface termination is the thetrahedrally one, the following model is proposed. Water readily dissociates on the surface to form two hydroxyl species. The first, $O_wH$, contains an oxygen atom from the water itself and sits on top of a Fe cation; the second, $O_sH$, derives from a H atom from the water and an oxygen from the surface lattice. These species act as anchors for molecular water adsorption ultimately giving rise to a long-range ordered structure. The results were rationalized by DFT calculations in the framework of cooperative formation of the hydrogen bonding network.

Further, the adsorption and activation of carbon dioxide on $Fe_3O_4(111)$ was investigated. Despite $CO_2$ adsorption studies on magnetite surfaces are scarce, proves of chemistry involving mainly different types of carbonates, bicarbonates, carboxylates intermediates, can be found on several metal oxide such as alumina, $TiO_2$, MgO or ZnO. This work provides - to the best of our knowledge - the first study on the $CO_2$ adsorption on $Fe_3O_4(111)$ model-surfaces. IRAS and TPD measurement showed that, between 120 K and 150 K, the $Fe_{tet1}$-regular surface behaves as rather inert towards $CO_2$ chemisorption, and mainly physisorption is observed. In this range of temperatures, the detected IRA-features characteristic for chemisorbed species consistent with carboxylates and carbonates, have to be interpreted as being driven by

the presence of surface imperfections. At temperatures as high as 200 K and slightly above, the presence of OH on the surface (both induced and/or coming with the residual gas adsorption) plays a critical role in the early stage of the $CO_2$ activation, promoting the formation of bicarbonate-like species.

Finally, a well-defined $Fe_3O_4$(100) model film was grown onto Pt(100) single crystal, and preliminary investigations on the adsorption of water and of $CO_2$ on this surface were performed by IRAS. These prior results were compared with the one obtained on $Fe_3O_4$(111), expecting a difference in the reactivity of the two surfaces due to their different structures. The $Fe_3O_4$(100) surface was found to be slightly less reactive towards water and $CO_2$, but the overall picture seems to be in good agreement with the results reported for the $Fe_3O_4$(111) surface. Certainly, more accurate and systematic work must be done in this direction, but these exploratory results on the (100)-oriented magnetite can serve as high quality benchmarks for further experimental investigations as well as theoretical calculations.

# Bibliography


1. G. Ertl, H. Knoezinger, F. Schuth, J. W. Handbook of Heterogeneous Catalysis. *Zeitschrift für Phys. Chemie* **208,** 274–278 (1999).

2. Thomas, J. M. Turning points in Catalysis. *Angew. Chemie - Int. Ed.* **33,** 913–937 (1994).

3. Boudart, M. Catalysis by Supported Metals. *Adv. Catal.* **20,** 153–166 (1969).

4. Ertl, G. Reactions at surfaces: From atoms to complexity (nobel lecture). *Angew. Chemie - Int. Ed.* **47,** 3524–3535 (2008).

5. Henry, C. R. Surface studies of supported model catalysts. *Surf. Sci. Rep.* **31,** 231–325 (1998).

6. Freund, H.-J. Adsorption of gases on solid surfaces. *Ber.Bunsen-Ges.* **99,** 1261–1281 (1995).

7. Freund, H. J. *et al.* Model studies on heterogeneous catalysts at the atomic scale: From supported metal particles to two-dimensional zeolites. *J. Catal.* **308,** 154–167 (2013).

8. Freund, H.-J. Model Studies on Heterogeneous Catalysts at the Atomic Level. *Catal. Today* **100,** 3–9 (2005).

9. Freund, H.-J., Shaikhutdinov, S. & Nilius, N. Model Studies on Heterogeneous Catalysts at the Atomic Scale. *Top. Catal.* **57,** 822–832 (2014).

10. Libuda, J. & Freund, H. J. Molecular beam experiments on model catalysts. *Surf. Sci. Rep.* **57,** 157–298 (2005).

11. Kleyn, A. W. Molecular beams and chemical dynamics at surfaces. *Chem. Soc. Rev.* **32,** 87–95 (2003).

12. Freund, Hans-Joachim, Kuhlenbeck, Helmut, Staemmler, V. Rep. Prog. Phys. **59,** 283–347 (1996).

13. Freund, H. J. Model studies in heterogeneous catalysis. *Chem. - A Eur. J.* **16,** 9384–9397 (2010).

14. Sala, a. *et al.* Defects and inhomogeneities in Fe3O4(111) thin film growth on Pt (111). *Phys. Rev. B* **86,** 155430 (2012).

15. Parkinson, G. S. Iron oxide surfaces. *Surf. Sci. Rep.* **71,** 272–365 (2016).

16. Munoz, M., de Pedro, Z. M., Casas, J. A. & Rodriguez, J. J. Preparation of magnetite-based catalysts and their application in heterogeneous Fenton oxidation - A review. *Appl. Catal. B Environ.* **176–177,** 249–265 (2015).

17. Weiss, W. & Ranke, W. Surface chemistry and catalysis on well-defined

epitaxial iron-oxide layers. *Prog. Surf. Sci.* **70,** 1–151 (2002).

18. Dictor, R. A. & Bell, A. T. Fischer-Tropsch Synthesis over Reduced Iron Oxide Catalysts and Unreduced. *J. Catal.* **97,** 121–136 (1986).

19. Gamba, O. *et al.* Adsorption of Formic Acid on the Fe 3 O 4 (001) Surface. *J. Phys. Chem. C* **119,** 20459–20465 (2015).

20. Lee, D. W. *et al.* The review of Cr-free Fe-based catalysts for high-temperature water-gas shift reactions. *Catal. Today* **210,** 2–9 (2013).

21. Davis, E. M. *et al.* Growth of Fe3O4(001) thin films on Pt(100): Tuning surface termination with an Fe buffer layer. *Surf. Sci.* **636,** 42–46 (2015).

22. Lemire, C., Meyer, R., Henrich, V. E., Shaikhutinov, S. & Freund, H. J. The surface structure of Fe3O4(111) films as studied by CO adsorption. *Surf. Sci.* **572,** 103–114 (2004).

23. Smith, R. S., Li, Z., Dohnálek, Z. & Kay, B. D. Adsorption, desorption, and displacement kinetics of H2O and CO2on Forsterite, Mg2SiO4(011). *J. Phys. Chem. C* **118,** 29091–29100 (2014).

24. Woodruff, D. P. Quantitative structural studies of corundum and rocksalt oxide surfaces. *Chem. Rev.* **113,** 3863–3886 (2013).

25. Pang, C. L., Lindsay, R. & Thornton, G. Structure of clean and adsorbate-covered single-crystal rutile TiO 2 surfaces. *Chem. Rev.* **113,** 3887–3948 (2013).

26. Diebold, U. The surface science of titanium dioxide. *Surf. Sci. Rep.* **48,** 53–229 (2003).

27. Jaeger, M. *et al.* Formation of a well-ordered by oxidation of NiAl(110). *Surf. Sci.* **259,** 235–252 (1991).

28. Kresse, G. *et al.* Structure of the Ultrathin. **308,** 1440–1442 (2005).

29. Benedetti, S., Benia, H. M., Nilius, N., Valeri, S. & Freund, H. J. Morphology and optical properties of MgO thin films on Mo(0 0 1). *Chem. Phys. Lett.* **430,** 330–335 (2006).

30. Liu, B. H., Boscoboinik, J. A., Cui, Y., Shaikhutdinov, S. & Freund, H. J. Stabilization of ultrathin zinc oxide films on metals: Reconstruction versus hydroxylation. *J. Phys. Chem. C* **119,** 7842–7847 (2015).

31. Huggins, C. P. & Nix, R. M. Growth and characterisation of Cr2O3(0 0 0 1) thin films on Cu(1 1 1). *Surf. Sci.* **594,** 163–173 (2005).

32. Mullins, D. R., Radulovic, P. V & Overbury, S. H. Ordered cerium oxide thin films grown on Ru ( 0001 ) and Ni ( 111 ). *Surf. Sci.* **429,** 186–198 (1999).

33. Weiss, W. & Ranke, W. Surface chemistry and catalysis on well-defined epitaxial iron-oxide layers. *Prog. Surf. Sci.* **70,** 1–151 (2002).

34. Kuhlenbeck, H., Shaikhutdinov, S. & Freund, H.-J. Well-Ordered Transition Metal Oxide Layers in Model Catalysis – A Series of Case Studies. *Chem. Rev.* **113,** 3986–4034 (2013).

35. Sickafus, K. E., Wills, J. M. & Grimes, N. W. Structure of Spinel. *J. Am. Ceram. Soc.* **82,** 3279–3292 (2004).

36. Senn, M. S., Wright, J. P. & Attfield, J. P. Charge order and three-site distortions in the Verwey structure of magnetite. *Nature* **481,** 173–176 (2011).

37. Seoighe, C., Naumann, J. & Shvets, I. V. Studies of surface structures on single crystalline magnetite(100). *Surf. Sci.* **440,** 116–124 (1999).

38. Shimizu, T. K., Jung, J., Kato, H. S., Kim, Y. & Kawai, M. Termination and Verwey transition of the (111) surface of magnetite studied by scanning tunneling microscopy and first-principles calculations. *Phys. Rev. B - Condens. Matter Mater. Phys.* **81,** 1–6 (2010).

39. Ketteler, G., Weiss, W., Ranke, W. & Schlögl, R. Bulk and surface phases of iron oxides in an oxygen and water atmosphere at low pressure. *Phys. Chem. Chem. Phys.* **3,** 1114–1122 (2001).

40. Parkinson, G. S. Iron oxide surfaces. *Surf. Sci. Rep.* **71,** 272–365 (2016).

41. Ritter, M. & Weiss, W. Fe O (111) surface structure determined by 3 4 LEED crystallography. **432,** 81–94 (1999).

42. Roddatis, V., Su, D. S., Kuhrs, C., Ranke, W. & Schlögl, R. Transmission electron microscopy investigation of Fe 3 O 4 films grown on (111) Pt substrates. *Thin Solid Films* **396,** 78–83 (2001).

43. Shaikhutdinov, S., Ritter, M., Wang, X., Over, H. & Weiss, W. Defect structures on epitaxial Fe 3 O 4 (111) films. *Phys. Rev. B* **60,** 62–69 (1999).

44. Weiss, W., Barbieri, A., Van Hove, M. A. & Somorjai, G. A. Surface structure determination of an oxide film grown on a foreign substrate: Fe\textsubscript{3}O\textsubscript{4} multilayer on Pt(1 1 1) identified by low energy electron diffraction. *Phys. Rev. Lett.* **71,** 1848–1851 (1993).

45. Sorenson, T. A., Morton, S. A., Waddill, G. D. & Switzer, J. A. Epitaxial electrodeposition of Fe3O4 thin films on the low-index planes of gold. *J. Am. Chem. Soc.* **124,** 7604–7609 (2002).

46. Huang, P. H., Lai, C. H. & Huang, R. T. Room-temperature growth of epitaxial (111) Fe 3O 4 films with conductive Cu underlayer. *J. Appl. Phys.* **97,** 1–4 (2005).

47. Farrow, R. F. C. *et al.* Nanoscale phase separation in Fe 3 O 4 „ 111 … films on sapphire „ 0001 … and phase stability of Fe 3 O 4 „ 001 … films on MgO „ 001 … grown by oxygen-plasma-assisted molecular beam epitaxy. **93,** 5626–5636 (2003).

48. Tasker, P. W. The stability of ionic crystal surfaces. *J. Phys. C Solid State Phys.* **12,** 4977–4984 (1979).

49. Lennie, A., Condon, N. & Leibsle, F. Structures of Fe 3 O 4 (111) surfaces observed by scanning tunneling microscopy. *Phys. Rev. B* **53,** 244–253 (1996).

50. Barbieri, A., Weiss, W., Hove, M. A. Van & Somorjai, G. A. Magnetite Fe\textsubscript{3}O\textsubscript{4} (1 1 1): surface structure by LEED crystallography and energetics. *Surf. Sci.* **302,** 259–279 (1994).

51. Dementyev, P. *et al.* Water Interaction with Iron Oxides. *Angew. Chemie Int. Ed.* n/a-n/a (2015). doi:10.1002/anie.201506439

52. Ceballos, S. F. *et al.* An atomic scale STM study of the Fe3O4(0 0 1) surface. *Surf. Sci.* **548,** 106–116 (2004).

53. Chambers, S. A., Thevuthasan, S. & Joyce, S. A. Surface structure of MBE-grown Fe O ( 001 ) by X-ray photoelectron di ff raction and scanning tunneling microscopy. **450,** 273–279 (2000).

54. Tarrach, G., Bürgler, D., Schaub, T., Wiesendanger, R. & Güntherodt, H.-J. Atomic surface structure of Fe3O4(001) in different preparation studied by scanning tunneling microscopy. *Surf. Sci.* **285,** 1–14 (1993).

55. Stanka, B., Hebenstreit, W., Diebold, U. & Chambers, S. Surface reconstruction of Fe 3 O 4(001). *Surf. Sci.* **448,** 49–63 (2000).

56. Pentcheva, R. *et al.* Jahn-Teller stabilization of a 'Polar' metal oxide surface: Fe3O4(001). *Phys. Rev. Lett.* **94,** 3–6 (2005).

57. Łodziana, Z. Surface verwey transition in magnetite. *Phys. Rev. Lett.* **99,** 1–4 (2007).

58. Yu, X., Huo, C. F., Li, Y. W., Wang, J. & Jiao, H. Fe 3O 4 surface electronic structures and stability from GGA + U. *Surf. Sci.* **606,** 872–879 (2012).

59. Parkinson, G. S., Novotný, Z., Jacobson, P., Schmid, M. & Diebold, U. A metastable Fe(A) termination at the Fe3O4(001) surface. *Surf. Sci.* **605,** 1–4 (2011).

60. Bliem, R. *et al.* Subsurface cation vacancy stabilization of the magnetite (001) surface. *Science (80-. ).* **346,** 1215–1218 (2014).

61. Gao, Y. & Chambers, S. A. Heteroepitaxial growth of a-Fe2O3, g-Fe2O3 and Fe3O4 thin films by oxygen-plasma-assisted molecular beam epitaxy. *J. Cryst. Growth* **174,** 446 (1997).

62. Spiridis, N., Barbasz, J., Łodziana, Z. & Korecki, J. Fe3 O4 (001) films on Fe(001): Termination and reconstruction of iron-rich surfaces. *Phys. Rev. B - Condens. Matter Mater. Phys.* **74,** 1–5 (2006).

63. Henderson, M. The interaction of water with solid surfaces: fundamental aspects revisited. *Surf. Sci. Rep.* **46,** 1–308 (2002).

64. Thiel, P. a, Madey, T. E. & Sloan, A. P. THE INTERACI ' ION OF WATER WITH SOLID SURFACES : FUNDAMENTAL ASPECTS and 0 Elsevier Science Pubhshers B . V . ( North-Holland Physics Publishing Division ). *Surf. Sci. Rep.* **7,** 211–385 (1987).

65. Kendelewicz, T. *et al.* Reaction of water with the (100) and (111) surfaces of Fe3O4. *Surf. Sci.* **453,** 32–46 (2000).

66. Cutting, R. S., Muryn, C. a., Vaughan, D. J. & Thornton, G. Substrate-termination and H2O-coverage dependent dissociation of H2O on Fe3O4(1 1 1). *Surf. Sci.* **602,** 1155–1165 (2008).

67. Joseph, Y., Ranke, W. & Weiss, W. Water on FeO(111) and Fe 3 O 4 (111): Adsorption Behavior on Different Surface Terminations †. *J. Phys. Chem. B* **104,** 3224–3236 (2000).

68. Joseph, Y., Kuhrs, C., Ranke, W., Ritter, M. & Weiss, W. Adsorption of water on FeO(111) and Fe3O4(111): identification of active sites for dissociation. *Chem. Phys. Lett.* **314,** 195–202 (1999).

69. Adib, K. *et al.* Chemistry of CCl4 on Fe3O4(1 1 1)-(2 × 2) surfaces in the presence of adsorbed D2O studied by temperature programmed desorption. *Surf. Sci.* **537,** 191–204 (2003).

70. Leist, U., Ranke, W. & Al-Shamery, K. Water adsorption and growth of ice on epitaxial Fe3O4(111), FeO(111) and Fe2O3(biphase). *Phys. Chem. Chem. Phys.* **5,** 2435–2441 (2003).

71. Rim, K. T. *et al.* Scanning Tunneling Microscopy and Theoretical Study of Water Adsorption on Fe $_3$ O $_4$ : Implications for Catalysis. *J. Am. Chem. Soc.* **134,** 18979–18985 (2012).

72. Shaikhutdinov, S. & Weiss, W. Adsorbate dynamics on iron oxide surfaces studied by scanning tunneling microscopy. *J. Mol. Catal. A Chem.* **158,** 129–133 (2000).

73. Grillo, M. E., Finnis, M. W. & Ranke, W. Surface structure and water adsorption on Fe3O4(111): Spin-density functional theory and on-site Coulomb interactions. *Phys. Rev. B* **77,** 075407 (2008).

74. Li, X. & Paier, J. Adsorption of Water on the Fe 3 O 4 ( 111 ) Surface : Structures , Stabilities , and Vibrational Properties Studied by Density Functional Theory. **4,** (2016).

75. Yang, T. *et al.* Structures and energetics of H2O adsorption on the Fe3O4(111) surface. *Ranliao Huaxue Xuebao* **37,** 506–512 (2009).

76. Zhou, C. *et al.* Density Functional Theory Study of Water Dissociative Chemisorption on the Fe 3 O 4 ( 111 ) Surface. **4,** 21405–21410 (2010).

77. Freund, H.-J. & Roberts, M. W. Surface chemistry of carbon dioxide. *Surf. Sci. Rep.* **25,** 225–273 (1996).

78. Lackner, K. S. A Guide to $CO_2$ Sequestration. *Sci. (New York, N.Y.* **300,** 1677–1678 (2003).

79. D'Alessandro, D. M., Smit, B. & Long, J. R. Carbon dioxide capture: Prospects for new materials. *Angew. Chemie - Int. Ed.* **49,** 6058–6082 (2010).

80. Solymosi, F. The bonding , structure and reactions and promoted metal surfaces of CO2 adsorbed on clean. *J. Mol. Catal.* **65,** 337 (1991).

81. Weilach, C., Spiel, C., Föttinger, K. & Rupprechter, G. Carbonate formation on Al2O3 thin film model catalyst supports. *Surf. Sci.* **605,** 1500–1506 (2011).

82. Haruta, M., Susumu, T., Tetsuhiko K., Hiroyuki, K., Genet, M. J. Low-Temperature Oxidation of CO over Gold Supported on TiO2, a-Fe2O3, and Co3O4. *J. Catal.* **144,** 175–192 (1993).

83. Udovic, T.J., Dumesic, J. A. Adsorptive Properties of Magnetite Surfaces as Studied by Desorption : Studies of 02 , NO , C02 , and CO Adsorption. *J. Catal.* **89,** 314–326 (1984).

84. Borchert, H. *et al.* Pd nanoparticles with highly defined structure on MgO as model catalysts: An FTIR study of the interaction with CO, O2, and H2 under ambient conditions. *J. Catal.* **247,** 145–154 (2007).

85. Monterra, C. and Orio, L. Surface Characterization of Zirconium Oxide II. The interaction with carbon dioxide at ambient temperature. *Mater. Chem. Phys.* **24,** 247–268 (1990).

86. Hadjiivanov, K., Vayssilov, G. N. Characterization of oxide surfaces and zeolites by carbon monoxide as an IR probe molecule. *Adv. Catal.* **47,** 307–511 (2002).

87. Schott, V. *et al.* Corrigendum to: Chemical Activity of Thin Oxide Layers: Strong Interactions with the Support Yield a New Thin-Film Phase of ZnO (Angewandte Chemie International Edition, (2013), 52, 45, (11925-11929), 10.1002/anie.201302315). *Angew. Chemie - Int. Ed.* **56,** 12399 (2017).

88. Wang, Y. *et al.* CO2 activation by ZnO through the formation of an unusual tridentate surface carbonate. *Angew. Chemie - Int. Ed.* **46,** 5624–5627 (2007).

89. Pozdnyakova, O. *et al.* Preferential CO oxidation in hydrogen (PROX) on ceria-supported catalysts, part II: Oxidation states and surface species on Pd/CeO2 under reaction conditions, suggested reaction mechanism. *J. Catal.* **237,** 17–28 (2006).

90. Paul, J., Hoffmann, F. M. & Robbins, J. L. Carbon monoxide and carbon dioxide decomposition on bulk polycrystalline alkali metals. *J. Phys. Chem.* **92,** 6967–6969 (1988).

91. Paul, J., Hoffmann, F. M. CO2 Conversion and Oxalate stability on Alkali-promoted Metal Surfaces: Sodium modified Al(100). *Catal. Letters* **1,** 445–455 (1988).

92. Wohlrab, S., Ehrlich, D., Wambach, J., Kuhlenbeck, H., Freund, H.-J. Promoter Action of Alkali in the Activation of CO2 on Pd(111): a HREELS Case Study. *Surf. Sci.* **220,** 243–252 (1989).

93. Liu, Z. M., Zhou, Y., Solymosi, F. & White, J. M. Vibrational study of carbon dioxide(1-) on potassium-promoted platinum (111). *J. Phys. Chem.* **93,** 4383–4385 (1989).

94. Pritchard, J., Chadwick, D., Zheng, K. Reaction of CO2/H2 on K-Cu(100): RAIRS Studies at Ultrahigh Vacuum and Higher Pressures. 304–307 (1993).

95. Paul, J., Williams, G. P. & Hoffmann, F. M. Carbon dioxide activation and alkali compound formation. I. Vibrational characterization of oxalate intermediates. *Surf. Sci.* **531,** 244–264 (2003).

96. Kolasinski, K. W. Surface Science: Foundations of Catalysis and Nanoscience. *Surf. Sci. Found. Catal. Nanosci. Third Ed.* (2012). doi:10.1002/9781119941798

97. Gundry, P.M., and Tompkins, F. C. Chemisorption of Gases on Metals. *Q. Rev. Chem. Soc.* **1,** 257–291 (1957).

98. Rettner, C. T., Auerbach, D. J., Tully, J. C. & Kleyn, A. W. Chemical Dynamics at the Gas−Surface Interface. *J. Phys. Chem.* **100,** 13021–13033 (1996).

99. Zaremba, E. & Kohn, W. Van der Waals interaction between an atom and a solid surface. *Phys. Rev. B* **13,** 2270–2285 (1976).

100. Christmann, K. *Introduction to surface physical chemistry (Topic in physical chemistry)*. (1991).

101. Cacciatore, M., Rutigliano, M. & Billing, G. D. Eley-Rideal and Langmuir-Hinshelwood Recombination Coefficients for Oxygen on Silica Surfaces. *J. Thermophys. Heat Transf.* **13,** 195–203 (1999).

102. Servos, M. R. Nanotechnology for Water Treatment and Puri cation Foreword by. *Lect. Notes Nanoscale Sci. Technol.* **22,**

103. Zhao, L. *et al.* Morphology-controlled synthesis of magnetites with nanoporous structures and excellent magnetic properties. *Chem. Mater.* **20,** 198–204 (2008).

104. Santos-Carballal, D., Roldan, A., Grau-Crespo, R. & de Leeuw, N. H. A DFT study of the structures, stabilities and redox behaviour of the major surfaces of magnetite Fe 3 O 4. *Phys. Chem. Chem. Phys.* **16,** 21082–21097 (2014).

105. YANG, T. *et al.* Surface structures of Fe3O4 (111), (110), and (001): A density functional theory study. *J. Fuel Chem. Technol.* **38,** 121–128 (2010).

106. D'Evelyn, Mark P., Matrix, R. J. REACTIVE SCATTERING FROM SOLID SURFACES. *Surf. Sci. Rep.* **3,** 413–495 (1984).

107. Barker, J. a. & Auerbach, D. J. Gas-surface dynamics, velocity distributions, trapping and residence times. *Faraday Discuss. Chem. Soc.* **80,** 277 (1985).

108. Libuda, J., Meusel, I., Hartmann, J. & Freund, H.-J. A molecular beam/surface spectroscopy apparatus for the study of reactions on complex model catalysts. *Rev. Sci. Instrum.* **71,** 4395 (2000).

109. King, David A, Wells, M. G. Molecular Beam Investigation od Adsorption Kinetics on Bulk Metal Targets: Nitrogen on Tungsten. *Surf. Sci.* **29,** 454–482 (1972).

110. Comsa, George and David, R. DYNAMICAL PARAMETERS OF DESORBING MOLECULES. *Surf. Sci. Rep.* **5,** 145–198 (1985).

111. Jacobs, D. The role of internal energy and approach geometry in molecule/surface reactive scattering. *J. Phys. Condens. Matter* **7,** 1023–1045 (1995).

112. Scoles, G. Atomic and Molecular Beam Methods. **1,** 721 (1988).

113. Hoffmann, F. M. Infrared Reflection-Absorption Adsorbed Molecules Spectroscopy. *Surf. Sci. Rep.* **3,** 107–192 (1983).

114. Hollins, P. The influence of surface defects on the infrared spectra of adsorbed species. *Surf. Sci. Rep.* **16,** 51–94 (1992).

115. H. Günzler, H. M. H. *IR-Spektroskopie Eine Einführung*.

116. Sakurai, J. Modern Quantum Mechanics. (1994).

117. Atkins, P. & Friedman, R. *Molecular Quantum Mechanics*. (1983).

118. Y.J. Chabal. Surface Infrared Spectroscopy. *Surf. Sci. Rep.* **8,** 211–357 (1988).

119. Mcintyre, J. . D. E. D. E. & Aspnes, D. E. Differential Reflection Spectroscopy of very Thin Surface Films. *Surf. Sci.* **24,** 417–434 (1971).

120. Greenler, R. G. Rahn, R. R., Schwartz, J. P. The Effect of Index of Refraction on the Position, Shape, and Intensity of Infrared Bands in Reflection-Absorption Spectra*. **48,** 42–48 (1971).

121. Greenler, R. G. Reflection Method for Obtaining the Infrared Spectrum of a Thin Layer on a Metal Surface. *J. Chem. Phys.* **50,** 1963–1968 (1969).

122. Tegeder, P. Optically and thermally induced molecular switching processes at metal surfaces. *J. Phys. Condens. Matter* **24,** (2012).

123. Hollins, P. & Pritchard, J. Infrared Studies of Chemisorbed on Single Crystals Layers. *Prog. Surf. Sci.* **19,** 276–350 (1985).

124. Grimley, T. B. The Normal Mode Frequencies of Chemisorbed Atoms and Molecules. *Proc. Phys. Soc.* **79,** 1203–1215 (1962).

125. Blyholder, G. CNDO Model of Carbon Monoxide Chemisorbed on Nickel. **126,** 756–761 (1974).

126. Blyholder, G. Molecular orbital view of chemisorbed carbon monoxide. *J. Phys. Chem. A* **68,** 2772–2777 (1964).

127. Efrima, S; Metiu, H. The Role of the electrostatic interactions in shifting the vibrational frequencies for the two adsorbed molecules. *Surf. Sci.* **109,** 109–126 (1981).

128. Gutiérrez-Vega, J. C., Rodríguez-Dagnino, R. M., Meneses-Nava, M. a. & Chávez-Cerda, S. Mathieu functions, a visual approach. *Am. J. Phys.* **71,** 233 (2003).

129. Langmuir, I. The evaporation, condensation and reflection of molecules and the mechanism of adsorption. *Phys. Rev.* **8,** 149–176 (1916).

130. Redhead, P. a. Thermal desorption of gases. *Vacuum* **12,** 203–211 (1962).

131. Habenschaden, E., Küppers, J. Evaluation of Flash Desorption Spectra. *Surf. Sci.* **138,** L147–L150 (1984).

132. King, D. A. THERMAL DESORPTION FROM METAL SURFACES: A REVIEW. *Surf. Sci.* **47,** 384–402 (1975).

133. Seah, M.P., Dench, W. A. Quantitative Electron Spectroscopy of Surfaces : a standard data base for electron inelastic mean free paths in solids. *Surf. Interface Anal.* **1,** 2–11 (1979).

134. Henzler, M., Göpel, W. *Oberfläschenphysick des Festkörpers*. (Teubner, 1994).

135. Geus, J. W. Preparation and Properties of Iron Oxide and Metallic Iron Catalysts. *Appl. Catal.* **25,** 313–333 (1986).

136. Huang, D.-M., Cao, D.-B., Li, Y.-W. & Jiao, H. Density function theory study of CO adsorption on Fe3O4(111) surface. *J. Phys. Chem. B* **110,** 13920–13925 (2006).

137. Watanabe, M., Kadowaki, T. Dissociation Reactions of CO gas on Fe and Fe3O4 Surfaces Observed by Raman-Ellipsometry Spectroscopy. *Appl. Surf. Sci.* **28,** 147–166 (1987).

138. Retwisch, D.G., Dumesic, J. A. The effect of metal-oxygen bon strenght on properties of oxides: II. Water-gas shift over bulk oxides. *Appl. Catal.* **21,** 97–109 (1986).

139. Tinkle, M, Dumesic, J. A. Isotopic Exchange Measurements of the Rates of Adsorptiot/Desorption and Interconversion of CO and CO2 over Chromia-Promoted Magnetite: Implications of the Rates for Water-Gas Shift. *J. Catal.* **103,** 65–78 (1987).

140. Li, X. *et al.* Surface Termination of Fe $_3$ O $_4$ (111) Films Studied by CO Adsorption Revisited. *J. Phys. Chem. B* **4,** acs.jpcb.7b04228 (2017).

141. Ertl, G., Neumann, M. & Streit, K. M. Chemisorption of CO on the Pt(111) surface. *Surf. Sci.* **64,** 393–410 (1977).

142. Steininger, H., Lehwald, S. & Ibach, H. On the adsorption of CO on Pt (111). *Surf. Sci.* **123,** 264–282 (1982).

143. Henrich, V. E. & Shaikhutdinov, S. K. Atomic geometry of steps on metal-oxide single crystals. *Surf. Sci.* **574,** 306–316 (2005).

144. Chatt, J., Duncanson, L. A. Olefin Co-ordination Compounds. Part I I I . Infrared Spectra and Structure: Attempted Preparation of Acetylene Complexes. *J. Am. Chem. Soc.* **586,** 2939–2947 (1953).

145. Pacchioni, G., Cogliandro, G. & Bagus, P. S. Characterization of oxide surfaces by infrared spectroscopy of adsorbed carbon monoxide: a theoretical investigation of the frequency shift of CO on MgO and NiO. *Surf. Sci.* **255,** 344–354 (1991).

146. Kimmel, G. A. *et al.* Polarization- and azimuth-resolved infrared spectroscopy of water on TiO 2(110): Anisotropy and the hydrogen-bonding network. *J. Phys. Chem. Lett.* **3,** 778–784 (2012).

147. Diebold, U. The surface science of titanium dioxide. *Surf. Sci. Rep.* **48,** 53–229 (2003).

148. Di Valentin, C. *et al.* Adsorption of water on reconstructed rutile TiO2(011)-(2×1): Ti=O double bonds and surface reactivity. *J. Am. Chem. Soc.* **127,** 9895–9903 (2005).

149. Brookes, I. M., Muryn, C. A. & Thornton, G. Imaging water dissociation on TiO2(110). *Phys. Rev. Lett.* **87,** 266103-1-266103–4 (2001).

150. Diebold, U. Perspective: A controversial benchmark system for water-oxide interfaces: H2O/TiO2(110). *J. Chem. Phys.* **147,** (2017).

151. Wlodarczyk, R. *et al.* Structures of the ordered water monolayer on MgO(001). *J. Phys. Chem. C* **115,** 6764–6774 (2011).

152. Meyer, B. *et al.* Partial dissociation of water leads to stable superstructures on the surface of zinc oxide. *Angew. Chemie - Int. Ed.* **43,** 6642–6645 (2004).

153. Noei, H. *et al.* The identification of hydroxyl groups on ZnO nanoparticles by infrared spectroscopy. *Phys. Chem. Chem. Phys.* **10,** 7092 (2008).

154. Yamamoto, S. *et al.* Water Adsorption on r-Fe 2 O 3 ( 0001 ) at near Ambient Conditions. **3,** 2256–2266 (2010).

155. Mu, R. *et al.* Dimerization induced deprotonation of water on RuO2(110). *J. Phys. Chem. Lett.* **5,** 3445–3450 (2014).

156. Kerisit, S., Parker, S. C. & Harding, J. H. Atomistic Simulation of the Dissociative Adsorption of Water on Calcite Surfaces. *J. Phys. Chem. B* **107,** 7676–7682 (2003).

157. Guhl, H., Miller, W. & Reuter, K. Water adsorption and dissociation on SrTiO3(001) revisited: A density-functional theory study. **3,** 1–8 (2010).

158. Mirabella, F. *et al.* Cooperative Formation of Long-Range Ordering in Water Ad-layers on Fe 3 O 4 (111) Surfaces. *Angew. Chemie Int. Ed.* 1–6 (2018). doi:10.1002/anie.201711890

159. Zaki, E., Mirabella, F., Ivars-Barcelo, F., Seifert, J., Carey, S., Li, X., Paier, J., Sauer, J., Shaikhutdinov, S., Freund, H.-J. Water adsorption on Fe3O4(111): Dissociation and Network Formation. *Phys. Chem. Chem. Phys.* **20**, 15764-15774 (2018).

160. He, Y., Tilocca, A., Dulub, O., Selloni, A. & Diebold, U. Local ordering and electronic signatures of submonolayer water on anatase TiO2(101). *Nat. Mater.* **8,** 585–589 (2009).

161. Kaya, S., Weissenrieder, J., Stacchiola, D., Shaikhutdinov, S. & Freund, H. J. Formation of an ordered ice layer on a thin silica film. *J. Phys. Chem. C* **111,** 759–764 (2007).

162. Bernal, J. D. & Fowler, R. H. A theory of wate and ionic solution, with particular reference to hydrogen and hydroxy ions. *J. Chem. Phys.* **1,** 515–548 (1933).

163. Meier, M., Hulva, J., Jakub, Z., Setvin, M., Bliem, R., Schmid, M., Diebold, U., Franchini, C., P. G. Water Agglomerates on Fe3O4(100). *submitted* (2018). doi:10.1002/elan.200704094

164. Freund, H.-J.; Roberts, M. W. Surface chemistry of carbon dioxide. *Surf. Sci. Rep.* 225–273 (1996).

165. Yu, K. M. K., Curcic, I., Gabriel, J. & Tsang, S. C. E. Recent Advances in CO 2 Capture and Utilization. *ChemSusChem* **1,** 893–899 (2008).

166. Burghaus, U. Surface chemistry of CO2 - Adsorption of carbon dioxide on clean surfaces at ultrahigh vacuum. *Prog. Surf. Sci.* **89,** 161–217 (2014).

167. Lin, X. *et al.* Structure and Dynamics of CO 2 on Rutile TiO 2 (110)-1×1. *J. Phys. Chem. C* **116,** 26322–26334 (2012).

168. Funk, S. *et al.* Adsorption dynamics of CO 2 on Cu(110): A molecular beam study. *J. Chem. Phys.* **600,** 583–590 (2006).

169. Tosoni, S., Spinnato, D. & Pacchioni, G. DFT Study of CO 2 Activation on Doped and Ultrathin MgO Films. *J. Phys. Chem. C* **119,** 27594–27602 (2015).

170. Calaza, F. *et al.* Carbon Dioxide Activation and Reaction Induced by Electron Transfer at an Oxide-Metal Interface. *Angew. Chemie Int. Ed.* n/a-n/a (2015). doi:10.1002/anie.201501420

171. Kadossov, E. & Burghaus, U. Adsorption kinetics and dynamics of CO, NO, and CO2 on reduced CaO(100). *J. Phys. Chem. C* **112,** 7390–7400 (2008).

172. Solis, B. H. *et al.* Initial stages of CO 2 adsorption on CaO: a combined experimental and computational study. *Phys. Chem. Chem. Phys.* **19,** 4231–4242 (2017).

173. Seiferth, O. *et al.* IR investigations of CO2 adsorption on chromia surfaces: Cr2O3 (0001)/Cr(110) versus polycrystalline α-Cr2O3. *Surf. Sci.* **421,** 176–190 (1999).

174. O. Seiferth, K. Wolter, H. Kuhlenbeck, H.-J. F. CO2 adsorption on Na precovered Cr2O3(0001). **505,** 215–224 (2002).

175. Pavelec, J. *et al.* A multi-technique study of CO 2 adsorption on Fe 3 O 4 magnetite. *J. Chem. Phys.* **146,** 014701 (2017).

176. Henderson, M. A. Evidence for bicorbonate formation on vacuum annealed TiO2(110) resulting from a precursor-mediated interaction between CO2 and H2O. *Surf. Sci.* **400,** 203–219 (1998).

177. Su, T. *et al.* Density functional theory study on the interaction of CO2with Fe3O4(111) surface. *Appl. Surf. Sci.* **378,** 270–276 (2016).

178. Bartos, B., Freund, H.-J., Kuhlenbeck, H., Neumann, M., Lindner, H., Müller, K. ADSORPTION AND REACTION OF CO, AND CO,/0 CO-ADSORPTION ON Ni(ll0): ANGLE RESOLVED PHOTOEMISSION (ARUPS) AND ELECTRON ENERGY LOSS (HREELS) STUDIES B. *Surf. Sci.* **179,** 59–89 (1987).

179. Moskovits, M. Surface selection rules. *J. Chem. Phys.* **77,** 4408–4416 (1982).

180. Pacchioni, G. Physisorbed and chemisorbed of the MgO(lO0) surface. *Surf. Sci.* (1993).

181. Wang, X., Shi, H., Kwak, J. H. & Szanyi, J. Mechanism of CO2 Hydrogenation on Pd/Al2O3 Catalysts: Kinetics and Transient DRIFTS-MS Studies. *ACS Catal.* **5,** 6337–6349 (2015).

182. Kuhlenbeck, H. *et al.* Adsorption and reaction on oxide surfaces: CO and CO2 on Cr2O3(111). *Berichte der Bunsengesellschaft für Phys. Chemie* **96,** 15–27 (1992).

183. U. Starke, J.B. Pendry, K. H. Diffuse Low-Energy Electron Diffraction. *Prog. Surf. Sci.* **52,** 53–124 (1996).

184. Gawande, M. B., Branco, P. S. & Varma, R. S. Nano-magnetite (Fe3O4) as a support for recyclable catalysts in the development of sustainable methodologies. *Chem. Soc. Rev.* **42,** 3371 (2013).

185. Moussy, J. B. From epitaxial growth of ferrite thin films to spin-polarized tunnelling. *J. Phys. D. Appl. Phys.* **46,** (2013).

186. Cutting, R. S., Muryn, C. a., Thornton, G. & Vaughan, D. J. Molecular scale investigations of the reactivity of magnetite with formic acid, pyridine, and carbon tetrachloride. *Geochim. Cosmochim. Acta* **70,** 3593–3612 (2006).

187. Adib, K. *et al.* Chemistry of CCl4on Fe3O4(1 1 1)-(2 × 2) surfaces in the presence of adsorbed D2O studied by temperature programmed desorption. *Surf. Sci.* **537,** 191–204 (2003).

188. Parkinson, G. S., Novotný, Z., Jacobson, P., Schmid, M. & Diebold, U. Room Temperature Water Splitting at the Surface of Magnetite. *J. Am. Chem. Soc.* **133,** 12650–12655 (2011).

189. Li, Z. *et al.* Reactions of deuterated methanol (CD3OD) on Fe3O4(111). *J. Phys. Chem. C* **119,** 1113–1120 (2015).

190. Ratnasamy, C. & Wagner, J. P. Water Gas Shift Catalysis. *Catal. Rev.* **51,** 325–440 (2009).

191. Yang, H., Ye, H., Zhai, S. & Wang, G. Leak detection of gas transport pipelines based on wigner distribution. *2011 Int. Symp. Adv. Control Ind. Process.* 258–261 (2011). doi:10.1002/apj

192. Mars, P. & van Krevelen, D. W. Oxidations carried out by means of vanadium oxide catalysts. *Chem. Eng. Sci.* **3,** 41–59 (1954).

193. Rhodes, C., Hutchings, G.J., Ward, A. M. Water-gas shift reaction: finding the mechanistic boundary. *Catal. Today* **23,** 43–58 (1995).

194. Tait, S. L., Dohnálek, Z., Campbell, C. T. & Kay, B. D. N-alkanes on MgO(100). II. Chain length dependence of kinetic desorption parameters for small n -alkanes. *J. Chem. Phys.* **122,** (2005).

# Abbreviations

**CEM** channeltron electron multiplier

**DFT** density functional theory

**EB** effusive beam

**ER** Eley-Rideal

**FT** Fourier Transform

**HREELS** high-resolution electron energy loss

**IR** infrared

**IRAS** infrared reflection-absorption spectroscopy

**LEED** low energy electron diffraction

**LH** Langmuir-Hinshelwood

**MB** molecular beam

**MCA** multi-channel arrays

**ML** monolayer

**MSSR** metal surface selection rule

**QCM** quartz crystal microbalance

**QMS** quadrupole mass spectrometry

**SSB** supersonic beam

**SCV** subsurface cation vacancies

**STM** scanning tunneling microscopy

**TDS** thermal desorption spectroscopy

**TPD** temperature programmed desorption

**TPR** temperature programmed reaction

**TR** time-resolved

**UHV** ultra-high vacuum

**UPS** Ultraviolet-photoelectron spectroscopy

**WGSR** water-gas shift reaction

**XPS** X-ray photoelectron spectroscopy

# List of Publications

1. "*Water adsorption on Fe3O4(100): an infrared study",*
   F. Mirabella, E. Zaki, M. Meier, G.S. Parkinson, X. Li, J. Paier, J. Sauer, S. Shaikhutdinov, H.-J. Freund;
   *(in preparation)*

2. "*$CO_2$ adsorption on magnetite surfaces",*
   F. Mirabella, F. Ivars-Barcelo, E. Zaki, X. Li, J. Paier, J. Sauer, S. Shaikhutdinov, H.-J. Freund;
   *(in preparation)*

3. *"Water adsorption on $Fe_3O_4$(111): Dissociation and the network formation",*
   E. Zaki*, F. Mirabella*, F. Ivars- Barceló, J. Seifert, S. Carey, X. Li*, J. Paier, J. Sauer, S. Shaikhutdinov, H.-J. Freund;
   *Phys. Chem. Chem. Phys., 2018, 02, 15764-15774.*
   .

4. *"Cooperative formation of long-range ordering in water ad-layers on $Fe_3O_4$(111)",*
   F. Mirabella*, E. Zaki*, F. Ivars- Barceló, X. Li*, J. Paier, J. Sauer, S. Shaikhutdinov, H.-J. Freund;
   *Angew. Chem. In. Ed., 2018, 57, 1409-1413.*

5. *"Surface Termination of $Fe_3O_4$(111) films studied by CO adsorption revisited"*
   X. Li, J. Paier*, J. Sauer, F. Mirabella, E. Zaki, F. Ivars, S. Shaikhutdinov*, H.-J. Freund
   *J. Phys. Chem. B*, *2018***,** 122, 527-533.

6. *"Selective Partial Hydrogenation of Acrolein on Pd: a Mechanistic Study",*
   K.-H. Dostert, C. P. O'Brien, F. Mirabella, F. Ivars- Barceló, S. Attia, E. Spadafora, S. Schauermann, H-J. Freund;
   *ACS Catalysis*, *2017, 7, 5523-5533.*

7. *"Adsorption of Acrolein, Propanal, and Allyl Alcohol on Pd(111): A combination of Infrared Reflection-Absorption Spectroscopy and Temperature Programmed Desorption Studies"*,
   K.-H. Dostert, C. P. O'Brien, F. Mirabella, F. Ivars- Barceló, S. Schauermann;
   *Phys.Chem.Chem.Phys., 2016, 18, 13960—13973.*

8. *"Water Interaction with Iron Oxides"*
   P. Dementyev, K.-H. Dostert, F. Ivars-Barcelo, C. O'Brain, F. Mirabella., S. Schauermann, X. Li, J. Paier, J. Sauer, H.-J. Freund.
   *Angew. Chem. In. Ed.,* 2015, 54, 1-6.

9. *"Spontaneous deposition of polylysine on surfaces: Role of the secondary structure to optimize noncovalent coating strategies"*
   A. Di Mauro, F. Mirabella, A. D´Urso, R. Randazzo, R. Purrello, M.E. Fragala.
   *Journal of Colloids and Interface Science, 2015, 437, 270-276.*

*These authors contributed equally to the work.

# Acknowledgments

Here I would like to thank all of the people who, in a way or another, were present during my PhD time and supported me.

I express my deepest gratitude to Prof. Dr. Hans-Joachim Freund for the terrific opportunity to work in his department. I have really appreciated his great competence and help during these years. I also would like to thank Prof. Dr. Schauermann for giving me the chance to join the Molecular Beam group in the very beginning of my work, and later on Dr. Shaikhutdinov for taking over my project.

I thank Prof. Dr. Rademann for being my official second supervisor and receiving my thesis.

I would like to thank the International Max Planck Research School (IMPRS) for the financial support (especially for the opportunity to join several german courses at the Goethe Institute), helpful block courses and lectures, outstanding workshops and countless opportunities to learn.

I would like to thank also all the members of the FHI and IMPRS for the atmosphere and the productive environment. The list would be too long to enunciate here.

A special thank goes to our great Secretary-Team, Manuela and Daniela, for being so professional, nice and helpful with all of us.

I thank Mauricio Prieto, a “part-time” member of our office, for always finding the time for a nice chat and also for proofreading my thesis.

I also would like to thank Uwe Härtel for being a great technical support, and also a nice company during long days spent repairing the machine.

Another particular thank must go to Jens Hartmann, not only for the exceptional technical support, but also being someone to talk to, for helping me looking for an apartment when I just arrived and checking on me when things turned complicated.

I also would like to thank Xuefei Weng, for being not only a very wise colleague, always there for scientific and technical discussions, but also for being the greatest

friend I’ve met at the institute, who supported me from the very beginning to the end and changed my perspective in life, I am truly honored to be your friend.

I thank my friends, the wonderful people I’ve met here in Berlin, who behaved as a family from the beginning. Among all of them, special thanks go to my dear Francesca (bela-bela), Puppo, Cogno Elena&Jorge, Rita&Luca and the little Miguelino, Giambo, and Lisa&Antonio and the little Manuel.

Thank to my “old” friends from Sicily, who I feel close to me as if I never left our beautiful island. Thank Federica and Giorgia, especially for knowing me so well and being always at my side. Thank also to Veronica, Andrea, Ciccino, Salvo, Fabio, Matilde and Agata. You all really made me understand that friendship has no boundaries.

Thank you, Linus, for the support and the patience, and for making our place smelling like coffee (sometimes also like cheese) every morning to pull me out of the bed and filling it with good music.

Last but not least, I would like to thank my family and in particular my Mamma and Papà for being there in their own way every single minute of this incredible experience, despite the distance. Without you, none of this would have happened. Thank also to my brother Angelo, Nonna Rosetta, Nonna Francesca and Nonno Angelo, Zio Nello & Zia Giovanna, Nino&Angela, ecc., for being the greatest Francesca’s Supporting Team ever. I felt your love even from 2000 km away.

This work is dedicated to my dear Nonno Nino, I know you would have enjoyed.

# Declaration of Independent Work

I declare that I have completed the thesis independently using only the aids and tools specified. I have not applied for a doctor's degree in the doctoral subject elsewhere and do not hold a corresponding doctor's degree. I have taken due note of the Faculty of Mathematics and Natural Sciences PhD Regulations, published in the Official Gazette of Humboldt-Universität zu Berlin no. 126/2014 on 18/11/2014.

Berlin, den

Francesca Mirabella